

**Red mud as an Iron-based Catalyst for Catalytic Cracking of
Naphthalene**

by

Shiva Madadkhani

B.A.Sc., The University of British Columbia, 2014

A THESIS SUBMITTED IN PARTIAL FULFILLMENT OF THE
REQUIREMENTS FOR THE DEGREE OF

MASTER OF APPLIED SCIENCE

in

The Faculty of Graduate and Postdoctoral Studies
(Chemical and Biological Engineering)

THE UNIVERSITY OF BRITISH COLUMBIA
(Vancouver)

December 2016

© Shiva Madadkhani, 2016

Abstract

Reducing the tar content in the producer gas of biomass gasification processes remains one of the main challenges in the commercialization of this technology and, hence, the development of clean and economical tar-removing technologies is becoming increasingly important. Catalytic tar removal has the advantage of avoiding expensive gas cleaning systems while maintaining the sensible heat in the producer gas. Commercial catalysts based on noble metals and metal oxides have shown good activity towards tar destruction, but are prone to rapid deactivation. This in addition to the high replacement cost provide the rationale for the development of low-cost alternatives. Red mud, a by-product from bauxite processing, has received considerable attention in this regard due to its high iron content in the form of ferric oxide (Fe_2O_3), high surface area, and its resistance to sintering and poisoning. However, very few studies have been conducted to investigate red mud as a potential catalyst for catalytic tar removal.

The aim of this study was to develop a catalyst from red mud for the removal of naphthalene, as a model compound for gasification tar. Red mud catalyst pellets were produced from raw red mud slurry, and their properties were investigated by measuring the chemical composition, surface area, and pore size distribution. Subsequently, the ability for tar decomposition was studied by passing naphthalene-nitrogen and naphthalene-hydrogen mixtures through a bed of the catalyst at five space velocities in the range of 4500-19,000 h^{-1} , and at reactor temperatures of 500, 600, 700 and 800°C. Catalytic cracking tests confirmed that red mud possesses a very high intrinsic catalytic activity for naphthalene conversion even at temperatures as low as 500°C and space velocities as high as 19,000 h^{-1} . Kinetic analysis was also performed to determine the apparent reaction order, the kinetic rate constants as well as the activation energy of the reaction. Long term tests of the catalyst showed that the activity of the catalyst diminished over time when no hydrogen was present in the system; however, in the presence of H_2 the activity was found to remain > 90% for 14 h.

Preface

The work presented in this dissertation was completed by Shiva Madadkhani under the supervision of Drs. Xiaotao Bi, John R. Grace, and Naoko Ellis at the Department of Chemical and Biological Engineering at the University of British Columbia. The experimental set-up used for the catalytic experiments presented in this thesis was designed and commissioned by Tyler G. P. Lewis and Dr. Luisa Burhenne. This was later modified slightly by Shiva Madadkhani. The initial part of the work, including baseline, benchmark and the preliminary tests with red mud were completed under the supervision of Dr. Luisa Burhenne. Thermal cracking experiments presented in Section 4.3 were completed by Dr. Luisa Burhenne. Parts of the catalyst characterization work presented in Chapter 4 were completed by Rahul Anand Sharma and Marine Lagorse.

Shiva Madadkhani prepared the initial and final drafts of this document, which was edited and approved by Professors Xiaotao Bi, John R. Grace and Naoko Ellis.

Table of Contents

Abstract	ii
Preface	iii
Table of Contents	iv
List of Tables	vii
List of Figures	ix
List of Symbols, Abbreviations and Nomenclature	xv
Acknowledgments	xvii
Dedication	xviii
Chapter 1: Introduction	1
1.1 Background.....	1
1.2 Objectives and Research Questions.....	7
1.3 Methodology.....	8
1.4 CREATE Sustainable Synthesis	10
Chapter 2: Literature Review	11
2.1 Gasification Reactions.....	11
2.2 Syngas Contaminants	12
2.3 Tars	14
2.4 Tar Reforming Reactions.....	17
2.5 Tar Sampling Methods	18
2.6 Tar Reforming Catalysts.....	20
2.6.1 Acid Catalysts	21
2.6.2 Alkaline Earth Catalysts	24
2.6.3 Metal Catalysts.....	25
2.6.3.1 Effect of Catalyst Support on Nickel Catalysts	29
2.6.3.2 Effect of Catalyst Promoters on Nickel Catalysts.....	32

2.6.4 Fe-based Catalysts	34
2.6.4.1 Red Mud.....	37
2.7 Catalyst Deactivation.....	41
Chapter 3: Experimental.....	42
3.1 Catalyst Preparation.....	42
3.2 Experimental Set-up	44
3.3 Acitivity Calculation.....	51
3.4 Characterization Techniques	51
3.4.1 Brunauer-Emmett-Teller (BET).....	51
3.4.2 X-ray Diffraction (XRD)	52
3.4.3 Scanning Electron Microscopy (SEM)	52
3.4.4 Thermogravimetric Analysis (TGA).....	53
3.4.5 X-ray Photoelectron Spectrometry (XPS)	53
3.4.6 CHN Analysis	53
3.4.7 X-ray Fluorescence (XRF).....	54
Chapter 4: Results and Discussion	55
4.1 Baseline Tests	55
4.2 Benchmark Tests	57
4.3 Thermal Cracking	58
4.4 Preliminary Tests with Red mud	60
4.5 Nitrogen Tests.....	66
4.5.1 Catalytic Activity	66
4.5.2 Kinetic Analysis.....	68
4.5.3 Catalytic Characterization.....	77
4.5.3.1 Catalyst Surface Area	77
4.5.3.2 Structural Analysis.....	84
4.5.3.3 Catalyst Chemical Composition	87

4.5.4	Discussion	96
4.6	Tests with H ₂	99
4.6.1	Catalyst Activity and Kinetic Results	99
4.6.2	Catalyst Characterization	104
4.6.2.1	Catalyst Surface Area	107
4.6.2.2	Catalyst Chemical Composition	110
4.6.3	Discussion	111
4.7	Long-term Tests.....	113
4.8	Products	115
Chapter 5: Conclusion		122
5.1	Recommendations	124
References		127
Appendices.....		139
Appendix A: Theoretical Naphthalene Feeding Rate		139
Appendix B: Benchmark Test Operating Parameters		142
Appendix C: Naphthalene Conversion Calculation		144
Appendix D: Kinetic Parameters Calculation.....		147
Appendix E: X-ray Diffraction Patterns		152
Appendix F: XPS Patterns		165
Appendix G: Brunauer-Emmett-Teller Analysis		170
Appendix H: Plug Flow Reactor Design Calculations		172

List of Tables

Table 1.1. Concentration of the major gas components in gasification syngas	2
Table 2.1. Gas quality requirements for syngas utilization	13
Table 2.2. Various chemical components in gasification tar as a function of process temperature	15
Table 2.3. Classes of tar based on GC/MS analysis	16
Table 2.4. Classes of tar based on temperature of formation	16
Table 2.5. Chemical composition of red mud from various regions	38
Table 2.6. Mineralogical phases of red mud found through powder XRD	39
Table 3.1. Typical elementary composition, metal oxides and other physical properties of the Alcan red mud, provided by the manufacturer	43
Table 3.2. Operating conditions for naphthalene conversion tests	50
Table 4.1. Apparent Kinetic Parameters of Inert Tests for Temperatures of 600-800°C. 76	
Table 4.2. Crystalline phases identified by powder XRD in the as received RM sample at 25°C (left) vs. fresh unspent pelletized RM (right)	88
Table 4.3. Crystalline phases identified by powder XRD at 25°C (left) vs. at 350°C (right) after exposing fresh unspent catalyst to different temperatures in a N ₂ environment	90
Table 4.4. Crystalline phases identified with powder XRD at 350°C (left) and 550°C (right) after exposing fresh unspent	91
Table 4.5. Crystalline phases identified by XRD at 550°C (left) and 1000°C (right) after exposing fresh unspent catalyst to temperature in a N ₂ environment	92

Table 4.6. Crystalline phases identified with powder XRD in fresh unspent catalyst pellet heated at 1000°C in N ₂ atmosphere (left) compared with spent catalyst pellets after 1 hour of reaction (middle) and 14 h of reaction (right)	95
Table 4.7. Kinetic rate constant of naphthalene cracking with red mud in presence of 13 vol.% H ₂ at the reaction temperatures tested	106
Table 4.8. Crystalline phases of RM as determined by Powder XRD after reduction with 13 vol.% H ₂	110
Table 4.9. Crystalline phases of RM as determined by Powder XRD after reaction with naphthalene in the presence of 13 vol.% H ₂	110
Table 4.10. Comparison of activation energies reported in the literature for naphthalene cracking with various catalysts	113
Table 4.11. CHN analysis of the fresh and spent catalyst pellet	118
Table 4.12. XPS analysis of fresh and spent RM catalyst surface	118
Table A1: Antoine equation constants of naphthalene	139
Table A2: The theoretical net hourly amount of naphthalene feeding rate	141
Table B1: Main parameters of benchmark tar cracking experiments	142
Table B2: Benchmark catalyst activation parameters	143
Table C1: Sample data from test on red mud catalyst in presence of 13 vol.% H ₂ in balance N ₂ with 3.85g of catalyst at 700°C	146
Table D1: Experimental results found for T = 800°C, GHSV = 5229 h ⁻¹ under pure N ₂	147
Table D2: Derived parameters for the determination of the reaction order with linear regression for T = 800°C, GHSV = 5229 h ⁻¹ under pure N ₂	148
Table G1: Red mud BET surface area and pore volumes reported in the literature	171

List of Figures

Figure 1.1. Thermochemical Biomass Conversion Routes	2
Figure 1.2. UBC Bioenergy Research and Demonstration Facility	3
Figure 1.3. An example of tar condensation on the surface of industrial units	4
Figure 1.4. Multi-stage production process of H ₂ and syngas from biomass gasification .	4
Figure 1.5. Primary and secondary tar removal measures	5
Figure 2.1. Product distribution in the various regimes of the gasification process	11
Figure 2.2. Transition of tar molecules as a function of process temperature	15
Figure 2.3. The European tar protocol for tar measurement	18
Figure 2.4. The Peterson column for tar measurement	19
Figure 2.5. Various elements investigated as different components of tar cracking catalysts.....	20
Figure 2.6. Weight distribution of products formed during tar cracking on LZ-Y82 zeolite catalyst.....	22
Figure 2.7. Structure of alumina-silica.....	25
Figure 2.8. Mechanism of benzene transformation to cyclohexane	25
Figure 2.9. Proposed mechanism for conversion of cyclohexane to methylcyclopentane on acid catalysts	25
Figure 2.10. Overall scheme of benzene cracking on acid zeolites	25
Figure 2.11. Steam reforming of toluene over group 1 transition metals	26
Figure 2.12. Steam reforming pathway of aromatic rings	27
Figure 2.13. TEM micrograms of nanocrystalline Ni/ZrO ₂ (left) and conventional Ni/ZrO ₂ catalysts (right).....	30

Figure 2.14. Increased metal/oxide boundary or perimeter at small particle sizes	30
Figure 2.15. Mayenite structure	31
Figure 2.16. Energy barrier for carbon and oxygen diffusion on the monometallic Ni catalyst and bimetallic Sn/Ni catalyst	33
Figure 2.17. Reaction scheme of benzene cracking	35
Figure 2.18. Reaction scheme of phenol cracking on supported iron catalysts	35
Figure 2.19. Temperature profile reduction of red mud with H ₂	40
Figure 3.1. Process flow diagram of the tar cracking unit	45
Figure 3.2. a) The tar vaporizer including the round-bottom flask and the condenser; b) The gas injection panel	46
Figure 3.3. a) Reactor vessel and the furnace; b) Reactor vessel with thermocouple	48
Figure 4.1. Results from the baseline test with naphthalene	56
Figure 4.2. Results from the benchmark tests performed at UBC, Fraunhofer ISE and Fraunhofer Umsicht on an industrial Ni catalyst at 850°C and SV of 19,000 and 4500 h ⁻¹	58
Figure 4.3. Degree of thermal naphthalene conversion in the reactor at temperatures of 650-1050°C at a space velocity of 19,000 hr ⁻¹	59
Figure 4.4. Bulk composition of red mud catalyst as found by XRF analysis	60
Figure 4.5. Preliminary tests results: performance of (a) Ni catalyst at 850°C and SV = 19,000 h ⁻¹ , (b) Ni catalyst at 850°C and SV = 4500 h ⁻¹ , (c) Ni catalyst at 800°C and SV = 19,000 h ⁻¹ , (d) Red mud catalyst at 850°C and SV = 19,000 h ⁻¹ , (a) Red mud catalyst at 800°C and SV = 19,000 h ⁻¹	61
Figure 4.6. Effect of temperature on the performance of RM catalyst at a space velocity of 19,000 h ⁻¹	62

Figure 4.7. Effect of space velocity on the performance of RM catalyst over a testing period of four hours	64
Figure 4.8. Effect of space velocity and temperature on naphthalene conversion in pure N ₂ -environment at space velocities of 4500-19,000 h ⁻¹ and temperatures of 500-800°C. 67	
Figure 4.9. Kinetic results of N ₂ tests at 500°C; Fitted to a first order model (n = 1, k = 26.44 ± 0.73 with 95% confidence)	72
Figure 4.10. Kinetic results of N ₂ tests at 600°C; (n = 1.42, k = 26724 ± 768)	73
Figure 4.11. Kinetic results of N ₂ tests at 700°C (n = 1.64 ± 0.08, k = 719414 ± 6949) 74	
Figure 4.12. Kinetic results of N ₂ tests at 800°C (n = 1.35 ± 0.05, k = 29175 ± 667).....	75
Figure 4.13. Effect of calcination on the surface area of as-received red mud powder determined by single point BET	78
Figure 4.14. Effect of calcination on surface area of pelletized red mud catalyst with multipoint BET	79
Figure 4.15. Effect of calcination on the pore size distribution of the catalyst	81
Figure 4.16. Surface area of post reaction pellets tested in an inert environment	82
Figure 4.17. BJH pore width distribution of fresh red mud catalyst compared with spent catalyst after reaction at temperatures of 500 to 800°C	84
Figure 4.18. SEM image of the as-received red mud powder.....	85
Figure 4.19. SEM image of the prepared red mud pellet prior to any reaction	86
Figure 4.20. SEM image of the red mud pellet after reaction at 850°C.....	86
Figure 4.21. SEM image of the red mud pellet after reaction at 850°C.....	87
Figure 4.22. Thermogravimetric analysis of unspent red mud pellet with nitrogen	89
Figure 4.23. Thermogravimetric analysis of as received red mud powder prior to any processing with nitrogen	93

Figure 4.24. Thermogravimetric analysis (under N ₂) of spent red mud pellet after exposure to a reactor temperature of 800°C.....	94
Figure 4.25. The complexity of heterogeneous catalysis.....	96
Figure 4.26. Carbonaceous deposits on the surface of the catalyst at (a) 500°C, (b) 600°, (c) 700°C, (d) 800°C	98
Figure 4.27. Results of naphthalene cracking tests performed at temperatures of 500-800°C at space velocities of 4508-18674 h ⁻¹ with 13 vol.% H ₂ in balance N ₂	99
Figure 4.28. Results of naphthalene cracking test with 13 vol.% H ₂ at a space velocity of 18,600 h ⁻¹	100
Figure 4.29. Results of naphthalene cracking test with 13 vol.% H ₂ in balance N ₂ at SV = 9,300 h ⁻¹	101
Figure 4.30. Results of naphthalene cracking test with 13 vol.% H ₂ at SV = 6500 h ⁻¹ ..	101
Figure 4.31. Results of naphthalene cracking test with 13 vol.% H ₂ in balance N ₂ at SV=4,500 h ⁻¹	102
Figure 4.32. Results of the kinetic analysis for test with 13 vol.% H ₂ test at 500°C	103
Figure 4.33. Results of the kinetic analysis for experiment with 13 vol.% H ₂ test at 600°C	104
Figure 4.34. Results of the kinetic analysis for experiment with 13 vol.% H ₂ test at 700°C	105
Figure 4.35. Results of the kinetic analysis for experiment with 13 vol.% H ₂ test at 800°C	106
Figure 4.36. Activation energy for naphthalene cracking on red mud with 13 vol.% H ₂ in balance N ₂	107
Figure 4.37. Multi-point BET surface area of reduced red mud pellet	108

Figure 4.38. Long term activity of the RM catalyst in pure N ₂ and 13 vol.% H ₂ in balance N ₂ at SV = 5229 h ⁻¹	114
Figure 4.39. Deactivation of catalyst surface due to coke formation	117
Figure 4.40. TGA analysis of spent catalyst with air.....	121
Figure D1: Linear regression for the estimation of reaction order. Pure N ₂ environment, T = 600°C.....	149
Figure D2: Linear regression for the estimation of reaction order. Pure N ₂ environment, T = 700°C.....	150
Figure D3: Linear regression for the estimation of reaction order. Pure N ₂ environment, T = 800°C.....	151
Figure E1: Powder XRD profile of the as-received red mud powder	153
Figure E2: Powder XRD profile of fresh pelletized red mud	154
Figure E3: Powder XRD profile of spent red mud pellet under pure N ₂ environment at 800C for 1 hour.....	155
Figure E4: Powder XRD profile of fresh red mud pellet heated to 350C	156
Figure E5: Powder XRD profile of fresh red mud pellet heated to 550C	157
Figure E6: Powder XRD profile of fresh red mud pellet heated to 1000C	158
Figure E7: Powder XRD profile of fresh red mud pellet heated to 1000C	159
Figure E8: Powder XRD profile of fresh red mud pellet reduced at 800C	160
Figure E9: Powder XRD profile of fresh red mud pellet reduced at 500C	161
Figure E10: Powder XRD profile of spent red mud pellet under 13 vol.% H ₂ in N ₂ at 800C for 1 hour.....	162
Figure E11: Powder XRD profile of spent red mud pellet under 13 vol.% H ₂ in N ₂ at 800C for 14 hours	163

Figure E12: Powder XRD profile of spent red mud pellet under pure N ₂ at 800C for 14 hours	164
Figure F1: XPS spectra of fresh as-received red mud powder	166
Figure F2: XPS spectra of fresh prepared red mud pellet	167
Figure F3: XPS spectra of spent red mud pellet	168
Figure F4: XPS spectra of fresh as received red mud powder, heated at 300°C for 24h right before analysis	169
Figure H1: Bischoff experimental findings on dispersion of fluid flowing in packed beds	173

List of Symbols, Abbreviations and Nomenclature

$^{\circ}\text{C}$	Degree Celsius
A	Pre-exponential factor
A_c	Cross-sectional area of the reactor (m^2)
\AA	Angstrom
B	Bischoff constant
BET	Brunauer-Emmett-Teller
C_A	Feed concentration (mol/m^3)
C_i	Concentration of naphthalene detected in each vial
cm	Centimeter
D	Reactor diameter (cm)
D_{AB}	Gas phase diffusivity (m^2/s)
d_{p_cat}	Particle diameter (equivalent diameter of sphere of the same volume), m
E_a	Activation energy
$\varepsilon_{\text{void}}$	Reactor bed voidage
F_A	Feed flow rate (mol/h)
FT	Fischer-Tropsch synthesis
GC	Gas chromatography
GC-MS	Gas chromatography/ Mass spectroscopy
ID	Inside diameter
k	Reaction rate constant
kg	Kilogram
L	Catalyst bed height (mm)
m_{cat}	Mass of catalyst
m_i	Inlet mass of naphthalene to the reactor
Δm_i	Mass of naphthalene detected during each sampling interval (i)
MFC	Mass flow controller
mm	Millimetre
μ_{dynamic}	Dynamic viscosity
μm	Micrometer
n	Reaction order
Naph	Naphthalene
nm	Nanometer
P_i	Partial pressure of each gas component
P_T	Total pressure in the naphthalene flask
Pe_{axial}	Axial Peclet number
ppmV	Parts per million by volume
QR	Quartz reactor
R	Universal gas constant
Re	Reynolds number

Re'	Reynolds number in packed beds
RM	Red mud
ρ	Density
SE	Standard error
SEM	Scanning electron microscopy
SNG	Synthetic natural gas
SV	Space velocity (h^{-1})
T	Temperature
TCU	Tar Cracking Unit
TF	Tubular furnace
TGA	Thermogravimetric Analysis
TPR	Temperature programmed reduction
TV	Tar vaporizer
U_s	Superficial gas velocity (m/s)
V_{cat}	Volume of catalyst in the reactor (m^3)
\dot{V}	Volumetric flow rate (m^3/h)
V_i	Partial volume of each gas component
V_T	Total gas volume in the naphthalene flask
W	Mass of catalyst (g)
X	Naphthalene conversion (%)
XRD	X-ray diffraction
XPS	X-ray photoelectron spectrometry
XRF	X-ray fluorescence
γ	Sphericity

Acknowledgments

First and foremost, I would like to express my sincere gratitude to my kind supervisor, Dr. Xiaotao Bi, and my outstanding co-supervisors Dr. John R. Grace and Dr. Naoko Ellis for their mentorship over the past two years, for sharing their deep pool of knowledge, and their continued support, patience and trust. I am forever grateful to them for all the amazing opportunities they provided me with to grow as an individual and as a researcher.

I would like to thank my committee member, Dr. Kevin Smith for all his help and support, for sharing his knowledge, and for the invaluable guidance throughout the various stages of my work. My most sincere thanks to Dr. Laurel Schafer, who helped me not only with her great suggestions and critics as my committee member, but also as the director of the CREATE Sustainable Synthesis program, for her tremendous effort to help all of us CREATE students succeed. I consider myself very fortunate for the opportunity to have been in this program.

My deep appreciation goes to Dr. Luisa Burhenne for her supervision, guidance and mentorship during my first year as a graduate student, for helping me develop a critical-thinking approach towards problems, and for her continued support throughout the rest of the project. I cannot thank her enough for all her support and kindness, and for all the hugs when things were looking dim.

The financial support of the CREATE Sustainable Synthesis program funded by the National Sciences and Engineering Research Council of Canada (NSERC) is gratefully acknowledged and appreciated.

I would also like to acknowledge and express appreciation for the help of the faculty and staff of the department for their support. Special thanks to our visiting and summer

students, Michael, Owen, Marine and Rahul for all their contributions to the project, and to the members of the gasification group.

I thank Hossein and Adel for all the coffee sessions, the encouraging discussions and all the positive energy they sent my way when I needed them the most. Sadaf, Leili, Ayesha, Joanne, Juana, Kimia, Maggie, Razana, Sara, and Michael, I cannot describe in words how grateful I am for having all of you in my life, even when I am miles away from some of you now. Thank you!

My most special thanks to my parents and to my sister, Dena, for their unconditional love and support, for their confidence in me and in my capabilities, for all the late-night/early-morning Skype and Whatsapp calls from all the way on the other side of the world and for bearing the hardship of having their daughter away from them for 2 years. I owe everything that I am to them.

I would like to dedicate this work to Tyler G. P. Lewis, who set the building blocks of this project. May he rest in peace.

To Tyler G. P. Lewis

Chapter 1

Introduction

1.1 Background

According to the 2014 report by the Intergovernmental Panel on Climate Change (IPCC): “Human influence on the climate system is clear and growing, with impacts observed on all continents. If left unchecked, climate change will increase the likelihood of severe, pervasive and irreversible impacts for people and ecosystems.” [1]. The report concludes that the majority of the world’s energy supplies need to be produced from renewable sources by 2050 to eventually phase out fossil fuels by the end of the century. This is while the majority of the world’s current energy needs are supplied through carbon-based fossil fuels. Development of a reliable and affordable clean energy supply remains a challenge [2].

Biomass is a promising source of renewable energy due its wide availability and diversity in terms of feedstock and end-use products. This is especially true in countries such as Canada with enormous biomass resources that can be transformed into value-added products such as chemicals, liquid transport fuels and novel biomaterials. Moreover, the geopolitical advantages of biomass are substantial. Biomass is a locally grown resource and is relatively free from geopolitical uncertainties.

The two major pathways for biomass conversion include biochemical and thermochemical processes, among which thermochemical processes are more effective for lignocellulosic feedstock conversion since these compounds are more resistant to

natural degradation processes [3]. Figure 1.1 depicts the three major routes of thermochemical biomass conversion.

Figure 1.1 has been removed due to copyright restrictions. It was a diagram of the thermochemical routes of biomass conversion [3].

Some of the disadvantages of biomass combustion are related to the high moisture content of biomass, as well as agglomeration and fouling due to the presence of alkali compounds. Although both are relatively old technologies, gasification and pyrolysis have gained renewed interest due to their potential to produce liquid fuels and chemicals from a wide range of feedstock [4].

Gasification involves the reaction of biomass with sub-stoichiometric amounts of oxygen at temperatures of 900-1200°C to produce what is commonly referred to as syngas or product gas, consisting mainly of H₂ and CO. The composition ranges of the major gas components in syngas can be found in Table 1.1. The composition of the gasification syngas is a strong function of the conditions in the gasifier such as the type of gasifier, the temperature as well as the gasification agent. The final ratio of H₂/CO in the product gas can be adjusted depending on the desired end use of the produced syngas.

Table 1.1: Concentration of the major gas components in gasification syngas [5]

Gasification agent	T (°C)	Gas Product (Vol. %)					
		H ₂	CO	CO ₂	CH ₄	N ₂	H ₂ O
Air	780-830	5-16	10-22	9-19	2-6	42-62	11-34
Steam	750-780	38-56	17-32	13-17	7-12		52-60
Steam + O ₂	785-830	14-32	43-52	14-36	6-8		38-61

Syngas has a wide range of applications. In small, decentralized communities it has the potential to be used in combined heat and power cycles (CHP) to produce heat and

electricity. A great example of this is the University of British Columbia's (UBC) Bioenergy Research and Demonstration Facility designed so that gasification syngas could be used in an IC engine to produce ~2 MW of electricity and 4354 kg/h of steam [6].

Figure 1.2 has been removed due to copyright restrictions. It was a picture of the Bioenergy Research and Demonstration Facility at UBC. Original source: <http://www.mmal.ca> [7].

At larger scales (capacities higher than 50 MW), biomass-fired integrated gasifier combined cycles (IGCC) seem very promising for heat and electricity generation [8]. Alternatively, syngas can be transformed to liquid fuels via the Fischer-Tropsch process. Significant research has been focused on the production of bio-based synthetic natural gas (SNG) from syngas. This is due to the fact that transportation is, and will continue to be, the primary demand for liquid hydrocarbons.

Syngas can also be used to produce hydrogen. This can be achieved in a number of ways including: thermo-catalytic decomposition of methane, adsorption-enhanced reforming, auto-thermal chemical looping reforming, or using a bubbling fluidized bed membrane reactor with either steam methane reforming or auto-thermal reforming catalysts [3]. One use of the produced hydrogen could, for instance, be in fuel cells. One of the major advantages of fuel cells over some of the other technologies is their higher efficiency, since they can directly convert chemical energy to electrical power. Some of the recent research projects on combining biomass gasification technologies with fuel cells are: ProBio, a joint project between the Max Planck Society and the Fraunhofer Research Institute, and CHRISGAS funded by the European Commission (EC) [9, 10].

One of the major challenges hindering the wide implementation of biomass gasification systems is the formation of complex, poly-aromatic compounds, commonly known as *tars*. These are organic compounds with molecular weights equal to or greater than that

of benzene (78 kg/kmol). Tar compounds have dew points of $\sim 300^{\circ}\text{C}$ and can easily foul on and clog many downstream industrial components such as heat exchangers, internal combustion engines, pipelines, etc. making syngas utilization extremely challenging.



Figure 1.3: An example of tar condensation on the surface of industrial units (Reprinted with permission from Energy Research Centre of Netherlands) [11]

Moreover, in applications where the producer gas is cooled below 100°C , in addition to the tar compounds, the water content of the producer gas also condenses leading to the formation of a toxic process condensate. This is due to the hazardous nature of tars formed at temperatures above 800°C . There is especially a great risk of adverse health effects from the soluble organic tars in the process condensate [12]. In most biomass gasification processes, the syngas clean-up stage is the largest cost component because of the stringent requirements of end-use applications [13].

Figure 1.4 has been removed due to copyright restrictions. It was an image of the multi-stage production process of hydrogen and syngas from biomass gasification [2].

Tar mitigation methods can generally be classified as primary and secondary techniques. Primary techniques refer to measures taken to reduce the production of tars and to destroy them as they are formed inside the gasifier itself; while, secondary methods refer to gas cleaning technologies downstream of the gasifier. Although primary measures, such as matching the gasifier type and operating conditions with the product end-use, are a fundamental first step, they cannot achieve complete removal of tar compounds. Hence a combination of primary and secondary measures needs to be adopted (Fig. 1.5) [4].

Figure 1.5 has been removed due to copyright restrictions. It was an image of the primary and secondary tar removal measures [14].

Secondary tar elimination methods can be further classified as thermal, physical or catalytic processes. One of the main disadvantages of physical tar removal methods is the fact that they do not eliminate tars but merely transfer the problem from the gas phase to a condensed state incurring additional economic and environmental costs [8]. Thermal processes involve high temperatures of around 1100°C and hence require large energy inputs and thermally resistant reactor materials. Catalytic cracking methods on the other hand eliminate tars by converting them into useful product gas components, retain the thermal energy in syngas and also avoid the generation of an additional waste stream. Moreover, the tar elimination step, methane reforming (if needed), and CO:H₂ ratio adjustment could all be achieved in a single step.

A number of different reactor configurations can achieve catalytic cracking; however, using the catalyst in a secondary reactor following the gasifier is preferred since it maximizes conversion and decreases catalyst deactivation due to coking and carbon deposition[8]Fluidized beds allow for temperature and composition uniformity and lower pressure drops within the reactor, but suffer from attrition of the catalyst. In contrast, catalysts in fixed bed reactors do not experience attrition but are more prone to coking [14].

Commercial catalysts based on noble metals and metal oxides have shown good activity towards tar destruction. Among group VIII metals, commercial nickel catalysts conventionally designed for hydrocarbon reforming in the petrochemical industry have been the predominant focus of hot gas clean-up research [15]. Despite their high tar removal efficiencies, nickel-based catalysts are prone to rapid deactivation due to coke formation. Moreover, minute amounts of nitrogen, sulfur and chlorine-containing compounds in the feed gas can poison the active sites on the catalyst, significantly reducing its performance. This, in addition to the cost of replacement, provides the rationale for investigating low-cost alternatives.

Iron-containing catalysts on the other hand are significantly cheaper and are widely used in the industrial Fischer-Tropsch synthesis and in the water-gas-shift reaction. Tamhankar et al. [16] were among the first to test iron-based catalysts for tar removal. They examined the conversion of benzene in the presence of an iron oxide/silica catalyst and found almost complete tar conversion. Since then numerous recent studies have found iron-containing catalysts to be effective in reforming gasification and pyrolysis tar [17-23].

Red mud is a waste by-product of bauxite processing in the aluminum industry with a high iron content in the form of iron oxides (Fe_2O_3). It is produced at an annual rate of 77 million tons [24]. Disposal and management of red mud tailings continues to be one of the main challenges in the aluminum industry, with the cost of disposal at ~\$3 per ton of alumina produced [25]. Some of the properties of red mud, such as its high surface area, resistance to poisoning, as well as low cost, make it a great potential alternative to the existing metal oxide catalysts [26]. Hence developing a catalyst from this by-product is not only an effective means of value addition to the waste, but also has the advantage of cost-competitiveness. There have been numerous studies on the activity and performance of red mud in catalyzing various reactions such as hydrogenation reactions of unsaturated organic compounds, coal liquefaction, hydrodechlorination reactions, as well as

degradation of polymeric mixtures and waste plastics into fuels [26]. However, to the best of my knowledge, Dr. Yanik and her collaborators at Ege University are the only group to have investigated red mud for steam reforming of tar. The results of their studies are discussed in more detail in Chapter 2.

1.2 Objectives and Research Questions

The aim of this research project was to investigate the effectiveness of red mud in catalytic tar removal compared with already existing commercial catalysts. This was achieved in a bench-scale packed bed reactor at various operating conditions with naphthalene as the model tar compound (as justified in Section 1.3). Results gained from naphthalene could be used to develop a predictive tool for other compounds in the future. Furthermore, these results could be tested at pilot-scale at UBC/Nexterra's Bioenergy Research and Demonstration Facility as well as the UBC dual fluidized bed gasifier, both located at the UBC campus.

Some of the topics addressed in this project include determining:

- The effectiveness of red mud compared with commercial catalysts in removing naphthalene.
- The effect of operating conditions such as space velocity and temperature on the tar removal performance of the catalyst.
- The physical and chemical characteristics of the catalyst particles and their evolution with calcination, catalyst reduction, and exposure to naphthalene.
- The kinetic parameters of the reaction of naphthalene with red mud as catalyst.
- The performance of the catalyst in a reducing reaction environment compared with a N_2 environment.

1.3 Methodology

The activity of the catalyst for tar decomposition is highly dependent on the nature of the tar compound tested. In general, tar compounds containing aliphatic chains or heteroatoms (such as pyridine), are converted more easily than those containing pure aromatic rings [27]. For the initial stage of the project, naphthalene was chosen as the model tar compound. This is mainly due to the fact that naphthalene is the most difficult to remove among model compounds of biomass tar, as indicated by several studies in the literature [28-30].

Before performing extensive tests on the catalyst, it was necessary to gain a basic understanding of the overall performance of the catalyst. Hence, a few preliminary tests were conducted to determine the degree of thermal cracking, the performance of the red mud catalyst compared with an industrial nickel catalyst, as well as to investigate the effects of temperature and space velocity on the overall reactant conversion.

Once a preliminary knowledge of the catalyst activity was acquired, more extensive testing was performed. The activity of the catalyst was tested at five space velocities and four reactor temperatures in a N₂ environment over a duration of one hour. The same tests were repeated in the presence of 13 vol.% H₂ with balance N₂ to determine whether there are any changes in the catalytic activity in a reducing environment. This information was then used to calculate the apparent reaction order, the kinetic constants, as well as the activation energy of the reaction.

The physical and chemical characteristics of the catalyst were examined before and after exposure to naphthalene. The effects of calcination and catalyst reduction with H₂ were also investigated separately in order to better track changes that occur in the catalyst as a result of exposure to the reaction environment. This was achieved by performing Brunauer-Emmett-Teller (BET) surface area measurements, scanning electron

microscopy (SEM), thermogravimetric analysis (TGA), as well as powder X-ray diffraction (XRD) on the catalyst. Moreover, the bulk and surface composition of the catalyst were determined by X-ray fluorescence spectroscopy (XRF) and X-ray photoelectron spectroscopy (XPS).

The project concluded with long-term tests of the catalyst, where the activity was measured both in the presence and absence of H₂ over 14 hours to determine the catalyst deactivation rate and to investigate whether the presence of H₂ results in any changes in the observed deactivation rate.

1.4 CREATE Sustainable Synthesis

This project was supported by the Collaborative Research and Training Experience Program, CREATE Sustainable Synthesis, funded by the Natural Sciences and Engineering Research Council of Canada (NSERC). This program aims to prepare industry-ready graduates to contribute to Canadian clean technologies by providing advanced interdisciplinary training in catalysis research, and providing industrial experience to trainees to facilitate the transition of new graduates into the Industrial Chemical Synthesis/Clean Technology sector with a focus on improving sustainable manufacturing methods.

Catalysis is a key component in providing the technological foundations necessary for development of sustainable, economic chemical processes with minimal waste/by-product generation. The work presented in this dissertation aims at developing a catalyst from an industrial waste product, red mud, to effectively remove tar compounds from gasification syngas. Every year millions of tons of highly alkaline red mud are produced and disposed of in reservoirs, potentially leading to many environmental hazards due to leakage to the sub-soil or resulting in incidents such as the Adjka reservoir accident in Hungary in 2010 [31]. Development of a catalyst from red mud, will not only contribute to value-addition to this industrial by-product, but will also help bring down some of the operational costs involved in gasification systems. Gas clean-up is one of the major cost-components in gasification systems, and hence development of an economic, yet effective catalyst is critical. If successful, the project will help make green energy production via biomass gasification more economically and environmentally attractive.

Chapter 2

Literature Review

The present chapter includes a summary of the literature related to gasification tar and its reforming reactions. First a brief overview of gasification reactions, the nature of tar compounds, and tar sampling methods is provided. This is followed by a more extensive discussion of the catalysts investigated in the literature for tar reforming.

2.1 Gasification Reactions

Biomass gasification is the reaction of biomass with sub-stoichiometric amounts of oxygen and involves a complex combination of pyrolysis and oxidation reactions [32]. Figure 2.1 provides an overview of the overall process involved in biomass gasification.

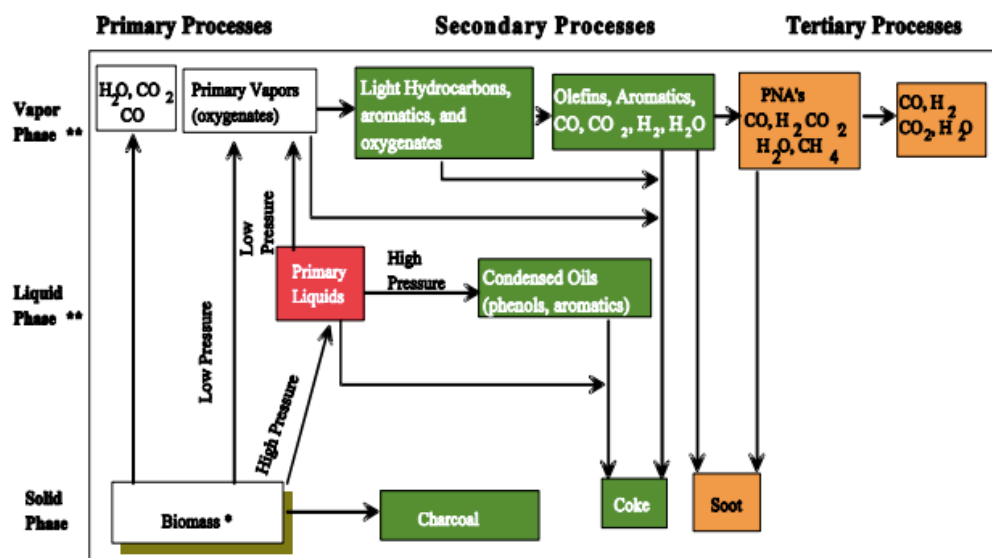
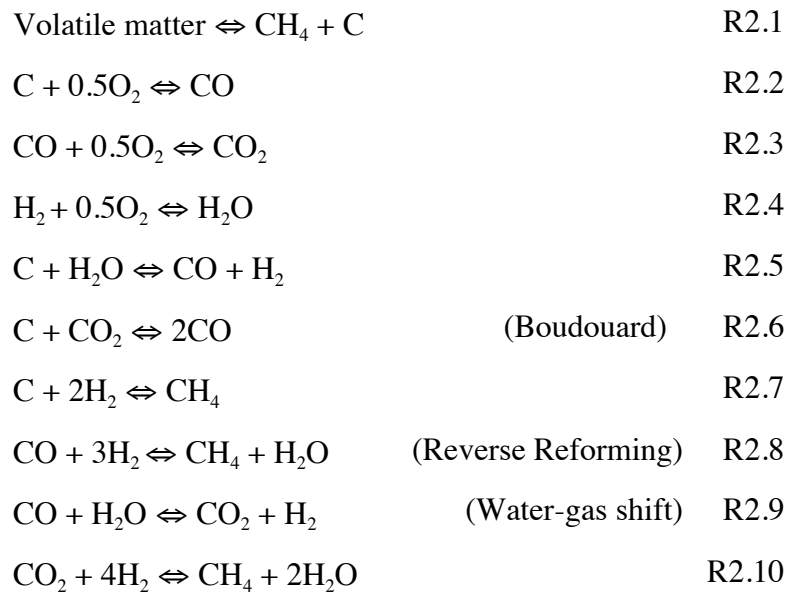


Figure 2.1: Product distribution in the various regimes of the gasification process.

Reprinted with permission from American Chemical Society. Copyright (1987) [33]

The first stage of biomass gasification is pyrolysis occurring at temperatures of 350-550°C, during which biomass is converted to char and volatiles. The produced char is then gasified and partially oxidised in the presence of a gasification agent (O₂, air, steam, CO₂ or a combination) at temperatures of 800-1300°C to form mainly H₂, CO, CO₂, and CH₄ (syngas) [34]. The main chemical reactions involved in biomass gasification are summarized below [15].



2.2 Syngas Contaminants

The resulting syngas from biomass gasification has many impurities. These include [35, 36]:

- ❖ Solid impurities: Dust, ash, char
- ❖ Inorganic impurities: Nitrogen compounds (NH₃, HCN) and sulphur compounds such as H₂S, HCl
- ❖ Organic impurities: Tars
- ❖ Alkali metals: Na and K compounds

In downstream syngas processing units, these contaminants can lead to several problems such as corrosion, erosion, formation of NO_x, SO_x, fouling and plugging. Hence following the gasifier, gas cleaning is an important next-step to reduce these contaminants to levels that comply with regulations and are suitable for the specific end-use application. Some of the gas quality requirements for syngas are listed in Table 2.1 for a few industrial applications.

Table 2.1: Gas quality requirements for syngas utilization [34, 35, 37]

Process	Contaminant	Level	Unit
<i>IC engines</i>	Tars	<10	mg/Nm ³
		<30	mg/Nm ³
	NH ₃	<50	mg/Nm ³
	Chlorides	<10	mg/Nm ³
	Total sulfur	<100	mg/Nm ³
	Particles	<50	mg/Nm ³
	Alkali metals	<1	mg/Nm ³
<i>Gas turbines</i>	Particles	<30	mg/Nm ³
	Alkali metals	0.24	mg/Nm ³
<i>PEM fuel cells</i>	CO	<10	ppm
	H ₂ S	<1	ppm
<i>Methanol synthesis</i>	Tars	<0.1	mg/Nm ³
	CH ₄	<3	%
	NH ₃	10	ppm
	HCN	0.01	ppm
	Total sulfur	0.5	ppm
	Halides	0.001	ppm

The concentrations of the contaminants in the producer gas are strong functions of the biomass feedstock used, the type of the gasifier, the gasification agent, gasifier temperature and pressure among other factors. Depending on the concentration of each contaminant and the end-use application, several gas cleaning techniques could be utilized. These include cyclones, fabric filters, ceramic filters, electrostatic precipitators and wet scrubbers.

Although very useful in removing other contaminants, many of these technologies such as cyclones and fabric filters are not suitable for tar removal. Ceramic filters, such as quartz and glass fibre filters have shown high tar removal efficiencies of 78-97%; however, they have not been studied extensively due to their high cost and complexity [38]. In addition to losing the thermal energy in the produced syngas, a major disadvantage of wet scrubbers is that they merely transfer the tar molecules from the gas phase to a liquid phase, requiring additional economic and environmental costs [8].

Due to their complexity, among all contaminants the removal of tars remains one of the largest barriers in biomass gasification systems. Significant research has been focused on hot gas clean-up technologies to convert these compounds to useful gas components, increasing the energy and material value of the produced syngas.

2.3 Tars

Tars are an assortment of condensable hydrocarbons ranging from single to 5-ring compounds, to complex polynuclear aromatic hydrocarbons (PAH)[39] There are several definitions for tars in the literature; however, in a EU, IEA, and US-DOE meeting in 1998 it was agreed to define tars as all organic contaminants with molecular weights greater than or equal to that of benzene [40]. Elliot et al. studied the transition of tar molecules and their “maturation” as a function of gasification process temperature from

mixed oxygenates to larger aromatic compounds. This general transition scheme is depicted in Fig. 2.2 [41].

Figure 2.2 has been removed due to copyright restrictions. It was an image of the Transition of tar molecules as a function of process temperature [32, 41].

Table 2.2: Various chemical components in gasification tar as a function of process temperature [32, 41]

Conventioanl Flash pyrolysis (450-500°C)	Flash High-temperature pyrolysis (600-650°C)	Conventional Steam Gasification (700-800°C)	High-temperature Steam Gasification (900-1000°C)
Acids	Benzenes,	Naphthalenes	Naphthalene
Aldehydes	Phenols	Acenaphthylenes	Acenaphthylene
Ketones	Catechols	Fluorenes	Phenanthrene
Furans	Naphthalenes	Phenanthrenes	Fluoranthene
Alcohols	Biphenyls	Benzaldehydes	Pyrene
Complex oxygenates	Phenanthrenes	Phenols	Acephenanthrylene
Phenols	Benzofurans	Naphthofurans	Benzanthracenes
Guaiacois	Benzaldehydes	Benzanthracenes	Benzopyrenes
Syringols			226 MW PAHs
Complex phenols			276 MW PAHs

Tars can be classified in a number of different ways. If classified based on GC/MS analysis, they can be divided to five subgroups as depicted in Table 2.3 [42, 43].

Table 2.3: Classes of tar based on GC/MS analysis [39]

Tar class	Class name	Property	Representative Compounds
1	GC-undetectable	Very heavy tars, cannot be detected with GC.	
2	Heterocyclic aromatics	Tars containing hetero atoms; highly water-soluble compounds	Pyridine, phenol, cresols, quinolone, isoquinoline, dibenzophenol
3	Light aromatics (1 ring)	Usually light hydrocarbons with a single ring; do not pose a problem regarding condensability	Toluene, ethylbenzene, xylenes, styrene
4	Light polyaromatic (2-3 rings)	2 and 3 ring compounds; condense at low temperatures	Indene, naphthalene, methylnaphthalene, biphenyl, acenaphthylene
5	Heavy polyaromatic (4-7 rings)	Larger than 3-rings, these compounds condense at high temperatures	Fluoranthene, pyrene, chrysene, perylene, coronene

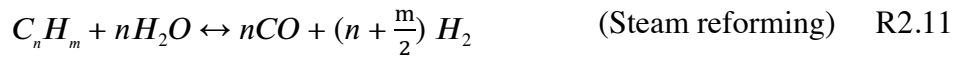
Alternatively, Evans et al. [33] suggested another method of tar classification in 1987. They used molecular beam spectrometry (MBMS) to divide tars into four major groups, as shown in Table 2.4.

Table 2.4: Classes of tar based on temperature of formation [34]

Tar Class	Class name	Property	Representative compounds
1	Primary	Derivates of cellulose, hemicellulose and lignin comprising relatively simple organic compounds	Acetol, phenol, guaiacol, furfural
2	Secondary	Phenolic and olefins	Phenol, xylene
3	Alkyl tertiary	Mainly methyl derivatives of aromatic compounds	Methylacenaphthalene, toluene, methylnaphthalene, indene
4	Condensed tertiary	PAH (2-6 rings)	Naphthalene, pyrene, anthracene, phenantrene

2.4 Tar Reforming Reactions

Tar conversion reactions are similar in concept to the reforming reactions of hydrocarbons in the oil and gas sectors [44]. The major difference between the two, however, is in the nature of the compounds being reformed, since tars from biomass gasification are a mixture of organic molecules with polyaromatic structures and include heteroatoms (such as O, S, or N). The main reactions involved in tar removal are represented in R2.11 through R2.16 [13].



Reforming reactions (dry and steam reforming) involve the decomposition of hydrocarbons to smaller fragments leading eventually to carbon monoxide and hydrogen in the presence of steam or carbon dioxide. These reactions involve two catalytic functions: dissociative adsorption of hydrocarbons on metallic sites, and dissociative adsorption of CO₂ and H₂O on oxide sites [45]. In the absence of a catalyst, the above reactions occur at temperatures of around 900°C – with high activation energy of ~250-350 kJ/mol [13]. Moreover, depending on the type of the end-use application, reaction R2.14 may not be very desirable. If the application of the produced syngas is for energy production, this would be useful as the conversion to CH₄ would increase the heating value of the product gas; however, in applications such as ammonia or methanol production, this would be undesirable [37, 46].

2.5 Tar Sampling Methods

Tar sampling methods can be classified as on- and off-line. Off-line methods are based on trapping the tar molecules by dissolving in organic solvents or condensation on cold surfaces and filters [39]. Among off-line tar measurement methods, the European tar protocol and solids surface adsorption (SPA) are more widely used.

The tar protocol is based on collecting tars and moisture in a series of 6 impinger bottles (Fig. 2.3). The first five bottles are filled with isopropanol, while the last one is kept empty [39]. As an alternative, the Peterson column, consisting of two jacket-cooled impinger bottles filled with isopropanol could also be used [47] (Fig. 2.4).

Figure 2.3 has been removed due to copyright restrictions. It was an image of the suggested apparatus for tar measurement according to the European Tar Protocol [39].

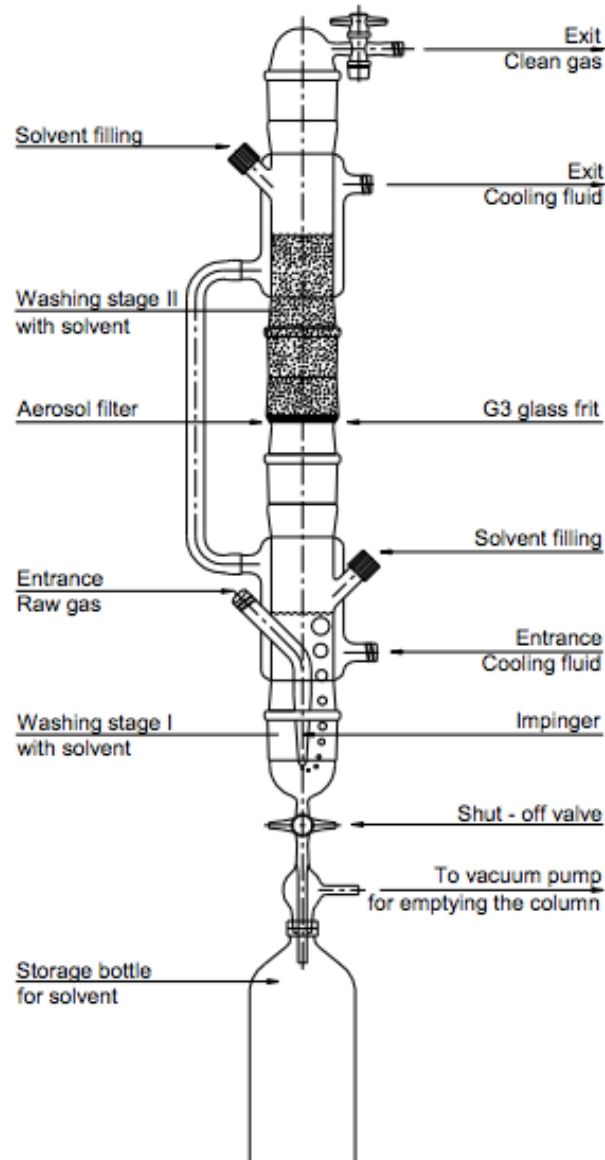


Figure 2.4: The Peterson column for tar measurement (Reprinted with permission from the Energy Research Centre of Netherlands) [47]

Solid phase adsorption involves passing the gas effluent through a solid phase extractor (SPE) to condense the tar out of the gas stream. This is followed by washing the collected tar with dichloromethane for the aromatic content, and a 1:1 solution of dichloromethane

and acetonitrile for the phenolic fraction, which can then be analyzed in a gas chromatograph [34].

Online tar measurement methods include laser-induced fluorescence (LIF), flame ionization detection (FID), and photo-ionization detection (PID). These methods, however, still need to be further developed and improved [34].

2.6 Tar Reforming Catalysts

Figure 2.5 illustrates a number of elements, mostly transition metals, which have been investigated in the literature as base catalysts and promoters for tar cracking reactions.

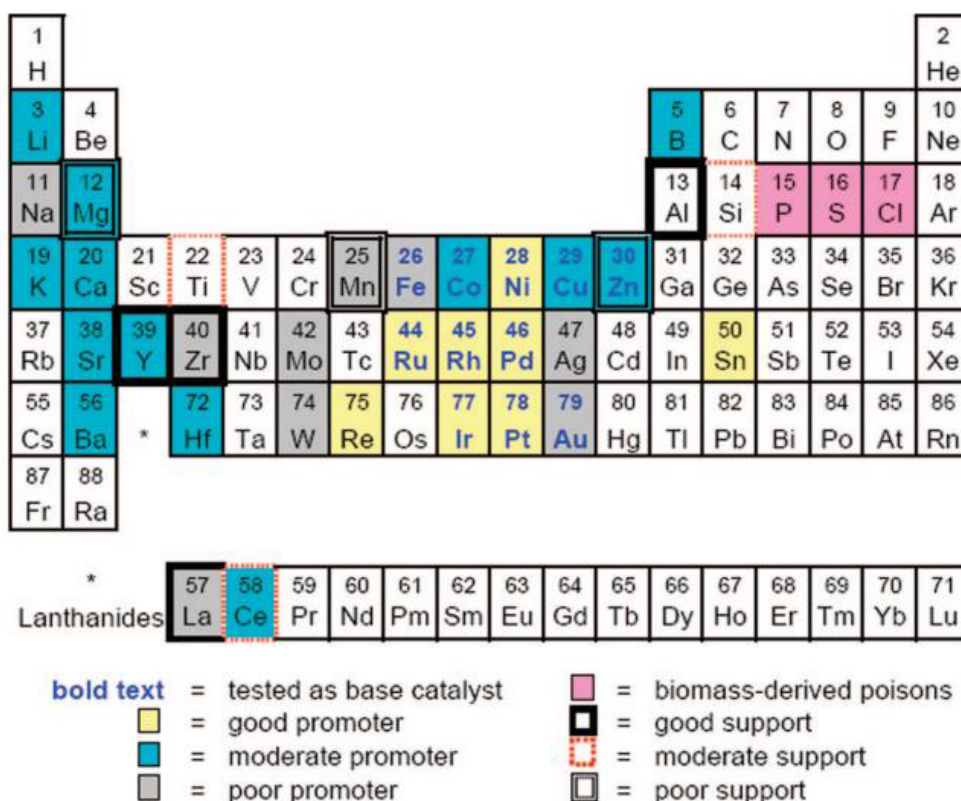


Figure 2.5: Various elements investigated as different components of tar cracking catalysts. Reprinted with permission from American Chemical Society. Copyright (2009)

American Chemical Society [48]

Some of the characteristics of a good tar reforming catalyst include [15]:

- High tar removal efficiency
- Methane reforming capability (if the desired product is syngas)
- Resistance to deactivation as a results of carbon fouling and sintering
- Easy regenerability
- Cost-effectiveness

Tar cracking catalysts have been classified in a number of different ways in the literature. In the following discussion, they are categorized in three big sub-groups, namely, acid catalysts, alkaline earth catalysts, and metal catalysts. Each category is described briefly below.

2.6.1 Acid Catalysts

Examples of acid catalysts used for tar removal include zeolites and silica-alumina. Silica-alumina catalysts ($\text{SiO}_2/\text{Al}_2\text{O}_3$) have an amorphous structure (non-crystalline), with most of their acid sites located in inaccessible parts of the catalyst, leading to low surface acidity. The surface acid density of silica/alumina, measured by temperature programmed desorption (TPD) of ammonia, is around $45 \text{ mm}^2/\text{m}^2$, whereas the surface acidity of zeolites is typically of the order of $100 \text{ mm}^2/\text{m}^2$ [4]. Hence generally $\text{SiO}_2/\text{Al}_2\text{O}_3$ catalysts possess lower catalytic activity compared with zeolites [49-52]. Adjaye et al. [53] for instance, tested the efficiency of silica/alumina in bio-oil upgrading and found its activity to be lower than the zeolite catalysts tested. Moreover, the performance of the catalyst was found to vary with changes in the reaction temperature. In another study Simmel et al. [54] found that most aluminum silicates lose their catalytic activity at temperatures above 850°C and act as inert materials. The authors found the following tar removal activity among the catalysts tested:

Ni on Al_2O_3 > dolomite > silica-alumina > silicon carbide (inert)

Zeolites are crystalline frameworks of $[\text{SiO}_4]^{4-}$ and $[\text{AlO}_4]^{5-}$ linked through oxygen atoms with a coordination polyhedral structure. Some of the advantages of zeolite catalysts include large surface area, well-defined and uniform micropores, and high adsorption capacity. Moreover, the pore volume, active sites as well as the electronic properties of zeolites can be controlled and adjusted, allowing for selective design of the catalyst [55]. For instance, addition of dispersed metals makes these catalysts suitable for ring breaking and hydrogenation reactions involved in tar cracking [4, 37].

Although zeolite catalysts have shown high tar conversions (95-100%), the rapid build-up of carbon deposits on their surface is a major disadvantage. As can be seen in Fig. 2.6, the main product of the tar reforming process with these catalysts is char [56].

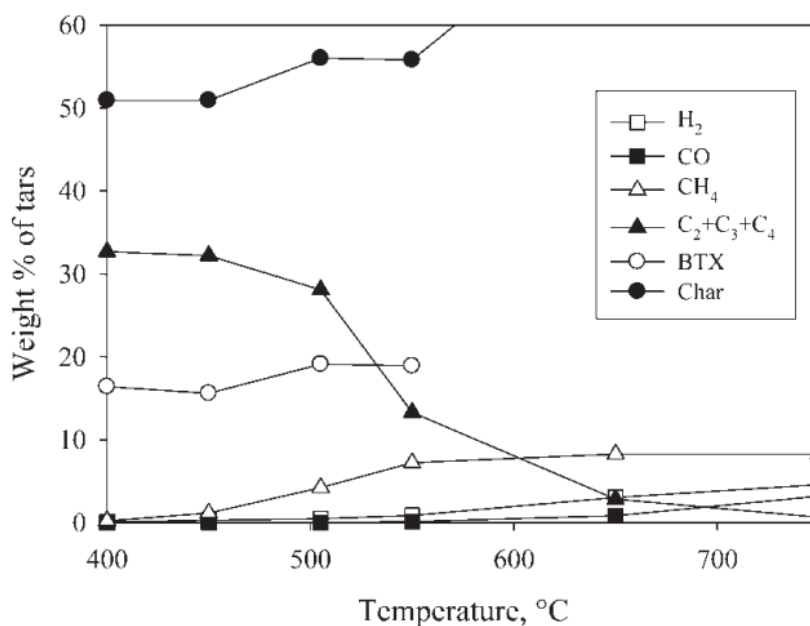


Figure 2.6: Weight distribution of products formed during tar cracking on LZ-Y82 zeolite catalyst. Reprinted with permission from American Chemical Society. Copyright (1984) American Chemical Society [56]

One possible mechanism of hydrogenation of benzene over Bronsted acid sites of zeolites is proposed by Cairon et al. [57] and is presented here. The heat of adsorption of benzene on HY zeolites is relatively high (69 kJ/mol at 500K) and hence the reaction of benzene is assumed to occur in the adsorbed phase. The first step of the reaction is the interaction of the benzene molecule with a zeolite hydroxyl, creating the adsorbed benzenium ion (Fig. 2.8). The benzenium ion then reacts with molecular hydrogen leading to 1,3-cyclohexadiene. The same process is repeated twice more to first form cyclohexene and then cyclohexane. Subsequently, the cyclohexane molecule is transformed to methylcyclopentane by carbocation (Fig. 2.9). The cyclohexane and methylcyclopentane molecules can further be transformed to smaller aliphatic hydrocarbons or desorb in the gas flow (Fig. 2.10) [57].

Figure 2.7 has been removed due to copyright restrictions. It was an image of the structure of alumina-silica [58].

Figure 2.8 has been removed due to copyright restrictions. It was an image of the suggested mechanism of benzene transformation to cyclohexane [57].

Figure 2.9 has been removed due to copyright restrictions. It was an image of the proposed mechanism for conversion of cyclohexane to methylcyclopentane on acid catalysts [59].

Figure 2.10 has been removed due to copyright restrictions. It was an image of the overall scheme of benzene cracking on acid zeolites [57].

2.6.2 Alkaline Earth Catalysts

Alkaline earth catalysts such as Na_2CO_3 , K_2CO_3 , and CsCO_3 are often added to the biomass feed – via dry mixing or wet impregnation as a primary catalyst inside the gasifier. One of the major disadvantages of these catalysts is that they increase the ash content of the char formed during gasification, making disposal more difficult [4]. Moreover, these catalysts are very difficult to recover after the gasification process making them less cost-effective [15]. Mckee and Gong [60, 61] have demonstrated that molten sodium and potassium carbonates as well as oxides and hydroxides of alkali metals, enhance tar decomposition during the gasification process. The order of the activity of the alkaline earth catalysts tested [60, 61] was found to be:



Huang et al. [62] also found the activity of potassium and sodium to be the highest among the five metal catalysts tested in gasification of char. Other operational problems with alkaline earth metals as primary catalysts include sintering and agglomeration of the catalyst particles [4].

As discussed later, alkali metals are most often added as promoters in commercial metal catalysts since they enhance the gasification of carbon atoms that deposit on the metal sites after the C-C bond cleavage, and hence prevent coking [20].

2.6.3 Metal Catalysts

Metal catalysts based on transition metals such as Rh, Ru, Pd, Pt and Ni have been reported to significantly reduce tar compounds from biomass gasification. These catalysts are generally comprised of three components: a metal site which represents the active site of the catalyst, a support material to enhance the mechanical strength of the catalyst and to protect it from attrition, and a promoter, such as alkali or alkaline earth metals to enhance the electronic properties and acid/basic characteristics [35, 48]. Each of these components is discussed in greater detail in the following sections.

Tar reforming catalysts are dual-functional. In hydrocracking catalysts (R2.14), these functions are:

- Cracking of aromatic hydrocarbons and C-C bond cleavage
- Hydrogenation of the unsaturated hydrocarbons formed through cracking [45]

A typical hydrocracking catalyst includes a group VIII metal on an acidic support such as silica/alumina, alumina or acidic zeolite. Hydrocarbon carbocation occurs on the acid sites, while hydrogenation of the unsaturated hydrocarbons from cracking (coke precursors) takes place on metallic sites [45]. The efficiency of the coordination between these two functions requires an optimal level of metal loading. Common hydrogenation metals include Pt, Ni, Pd, Mo and Co [63].

The second tar-reforming pathway is via the metal catalyzed steam reforming reaction (R2.11), where the tar molecules and water are dissociatively adsorbed on the catalyst surface. The hydroxyl groups from water dissociation then react with the hydrocarbon fragments [64].

Transition metal catalysts can be categorized in two groups. The first group, consisting of noble metals such as Pt, Rh, and Pd are more sensitive to the support material effects

[65]. Since the heat of oxygen chemisorption on these metals is relatively low (<400 kJ/mol), they require a support for activating water to hydroxyl groups. In these catalysts, aromatic tar molecules are chemisorbed on the metal sites, while water is activated on the support. The rate-determining step of the tar cracking reaction is then the migration of hydroxyl groups towards metal sites to react with hydrocarbon fragments [65-67]. As can be seen in Fig. 2.11, in the presence of the first group of transition metal catalysts, toluene is dissociated to a phenyl and methyl group on the metallic sites; while, water is dissociated to hydroxyl groups on the acid sites of the support. Transfer of hydrogen from Bronsted acid sites to the phenyl group results in the formation of benzene, which is subsequently desorbed from the catalyst surface, and a carbene molecule, which can react with oxygen in the support or dehydrogenate other hydrocarbons [64, 68].

Figure 2.11 has been removed due to copyright restrictions. It was an image of the steam reforming of toluene over group 1 transition metals [68].

The second group of transition metal catalysts consists of Ni, Ru, and Co, metals that are less sensitive to the support material. Since these elements are more oxidizable, having a high heat of oxygen chemisorption, water molecules and tars are competitively adsorbed on the metal surface. Although the support material assists with hydroxyl formation and water adsorption, its main contribution is through metal dispersion and sintering prevention. Hence, unlike the first group of transition metals, the rate-determining step of the reaction with these catalysts is not controlled by transportation of oxygen through the support [65].

The reaction pathway illustrated in Figure 2.12 demonstrates how aromatic rings are progressively opened by the catalyst in steam reforming reactions, eventually resulting in a tar molecule with one less ring. As can be seen, the main reactions include: hydrocarbon carbocation via attachment of Bronsted acids, cleavage of aromatic carbon-

carbon bonds and hence nucleus degradation, dehydrogenation, and finally dealkylation of the side chains producing H_2 and CO . The size of the alkyl groups on the side chains can affect the rate of the reaction. For instance, toluene is more readily dealkalized compared with alkyl-benzenes [68, 69].

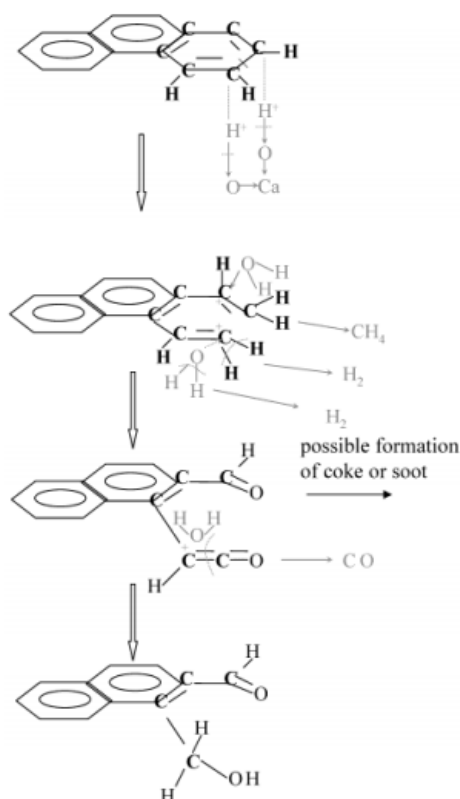


Figure 2.12: Steam reforming pathway of aromatic rings. Reprinted with permission from American Chemical Society. Copyright (2003) American Chemical Society [69]

Among transition metal catalysts, rhodium and nickel exhibit higher catalytic activities for tar destruction. In a 2002 study, Aupretre et al. tested alumina-supported group VIII metals, excluding Os, Co and Ir, for ethanol steam reforming and found rhodium and nickel to have the highest activity among all catalysts [70]. Tomishige et al. investigated steam reforming of biomass tar and found the order of the catalytic tar removal efficiency to be [71]:



Sutton et al. evaluated the dry reforming reactions of methane and propane and found alumina supported nickel to have the highest activity, followed by ruthenium alumina, and platinum on zirconium dioxide [72]. Assadullah et al. tested several commercial catalysts and found the carbon-based tar conversion efficiency of G-91 nickel catalyst and ruthenium to be 89% and 97%, respectively [73]. Simell et al. found alumina supported nickel catalysts to be effective in complete tar removal, surpassing silica-alumina, silicon carbide, activated alumina and dolomite catalysts at 900°C [54].

Although non-nickel metal catalysts such as platinum and rhodium are very effective in removing tar compounds and are more resistant to surface coke formation, they are much more expensive than nickel catalysts. Considering the low economic margins of biomass gasification units, nickel catalysts are a more viable option. Commercial nickel catalysts conventionally designed for hydrocarbon reforming in the petrochemical industry have been the predominant focus of hot gas clean-up research.

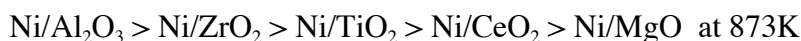
Supported nickel catalysts used in industrial steam-reforming processes were originally designed for paraffinic hydrocarbon reforming and are not suitable for reforming poly-aromatic tar components found in the gasification product gas [68]. Some of the more commonly used support and promoter materials for nickel catalysts are discussed in the following sections.

2.6.3.1 Effect of Catalyst Support on Nickel Catalysts

Catalyst support material can improve the catalytic activity by:

- Enhancing the dispersion of the active metal phase;
- Modifying the electronic properties of the metal phase through the electron donor/acceptor groups in the support; or
- Affecting the acidity/basicity characteristics of the catalyst, which in some cases will enable the support to intervene in the reaction process and possess a function necessary in the reaction pathway [48].

Alumina is the most commonly used support for nickel metal catalysts in the industry. This is mainly due to its unique crystal structure, which translates into high surface area, great mechanical strength and high metal dispersion capacity, in addition to its cost-effectiveness [2]. Sutton et al. tested the tar removal activity of a number of different nickel catalysts supported on Al_2O_3 , ZrO_2 , TiO_2 and SiO_2 and found Ni/ TiO_2 to have the highest efficiency, removing 98.1% of the tar compounds. This was followed by Ni/ ZrO_2 with efficiency of 92%. The tar removal efficiencies of the same support materials in the absence of nickel particles were found to be 79.5% and 78.4% for TiO_2 and ZrO_2 , respectively [15, 72]. Miyazawa et al. tested the same nickel-supported catalysts in steam reforming of tar from wood pyrolysis and found the order of the activity to be [74]:



In order to improve the activity of alumina supported catalysts, Roh et al. [75] evaluated the addition of 30% MgO to the support. They found a 25% improvement in the activity of Ni/MgO- Al_2O_3 compared with the un-promoted nickel-alumina. These findings were attributed to enhanced metal-support interactions, which were found from temperature-programmed reduction analysis [75]. Matsumura et al. found that at 500°C nickel was

gradually oxidized and deactivated on the Ni/Al₂O₃ and Ni/SiO₂ catalysts; however, Ni/ZrO₂ deactivated at a higher temperature due to stronger metal-support interaction [76].

Ni catalysts supported on zirconium oxide nanocrystalline exhibited superior activity levels and coke resistance properties compared with Ni/Al₂O₃ and conventional Ni/ZrO₂ catalysts [77]. One possible explanation for this could be the fact that the metal/oxide boundary is increased once the particle size is reduced (Figs. 2.13 and 2.14). Since CO₂ (for dry reforming) and H₂O molecules (for steam reforming) are activated at these boundaries, reducing the particle size enhances the transfer of oxygen atoms to carbonaceous deposits and hydrocarbon fragments on the nickel metal sites [78].

Figure 2.13 has been removed due to copyright restrictions. It was an image of TEM micrograms of nanocrystalline Ni/ZrO₂ and conventional Ni/ZrO₂ catalysts [77].

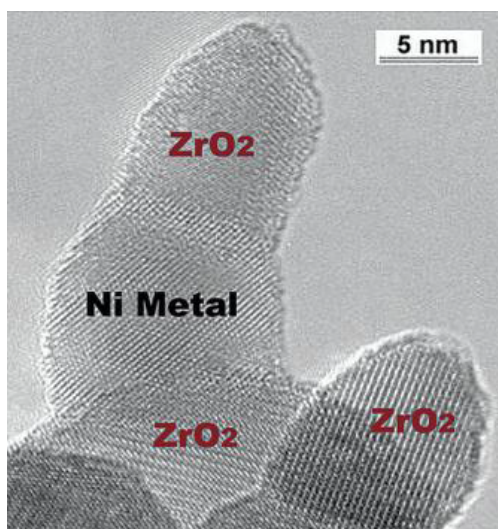


Figure 2.14: Increased metal/oxide boundary or perimeter at small particle sizes. Reprinted with permission from American Chemical Society. Copyright (2003) American Chemical Society [78]

Impregnation of nickel particles on a zeolite support is another possibility that has been explored by a number of researchers. Buchireddy et al. [79] found that the tar reforming activity of nickel was increased when added to zeolites. It was shown that nickel-supported ZY-30 and ZY-80 achieved naphthalene conversions of 99%. Moreover, the catalysts exhibited very little loss in activity during a 97-hour test. Inaba et al. tested a zeolite supported nickel catalyst, promoted with cerium oxide, as a primary catalyst and found the output tar levels to be significantly lowered. However, since the catalyst was added directly to the gasifier, a large amount of coke was deposited on the surface of the catalyst. Moreover, the nickel particles were heavily agglomerated [80].

Li and Hirabayashi [81] prepared a nickel/mayenite ($\text{Ca}_{12}\text{Al}_{14}\text{O}_{33}$) catalyst and evaluated its catalytic activity in steam reforming of toluene. Mayenite consists of a calcium-aluminate framework. The aluminate ions are linked together by sharing corner oxygen atoms. The remaining 'Free' oxygen is located in micro-pores (cages) of mayenite in the form of hydroxide, peroxide and superoxide radicals (Fig. 2.15). These superoxide radicals have the ability to transfer to metallic nickel sites and gasify the deposited carbon. Moreover, the free oxygen can be substituted by sulphur and hence hinder catalyst deactivation in the presence of sulphur-containing compounds.

As expected, the toluene conversion efficiency of nickel-mayenite was found to be above 90% at 600°C, with great activity against coke deposition and hydrogen sulphide poisoning [81].

Figure 2.15 has been removed due to copyright restrictions. It was an image of the structure of Mayenite [81].

Ni/lanthanum oxide was also found to show high catalytic activity in dry reforming of methane. The activity of the catalyst was found to be higher than alumina and CaO

supported nickel catalysts. Moreover, despite significant coking during the Ni/Al₂O₃ reaction, not much carbon deposition occurred with Ni/La₂O₃. XPS analysis indicated that carbon dioxide compounds were selectively adsorbed on the surface of the support, forming La₂O₂CO₃ which prevented coke formation [48].

2.6.3.2 Effect of Catalyst Promoters on Nickel Catalysts

The significant enhancement in the catalytic activity of nickel catalysts by addition of alumina demonstrated the importance of surface acidity in tar reforming/cracking reactions. This led a number of researchers to investigate the effect of addition of alkali and alkaline earth metals as promoters to metal catalysts, and more specifically to determine their effect on metal dispersion, surface acidity and metal-support interactions. Alkali and alkaline earth cations are electron donors (Lewis bases) and can reduce the acidity of the catalyst surface. Moreover, in their oxide form they can form bonds with the acidic sites of the support material and can modify the interactions between the metal and the support [82].

Juan et al. [83] studied the effect of potassium content on the activity of alumina-supported nickel catalysts for dry reforming of methane. They determined that potassium enhanced the reducibility of nickel metal sites, leading to very low coke deposition and high catalytic activity throughout the reaction. TPR analysis of the catalyst surface suggested that this was through modification of catalyst-support interactions.

Bangala et al. [44] investigated the effect of Cr₂O₃ addition as a promoter to nickel/alumina catalysts in naphthalene conversion. They found that to attain the optimal tar conversion levels while minimizing the degree of coke formation on the catalyst surface, the Cr loading needs to be around 5 wt.%. XRD analysis of the Cr-doped nickel catalysts prior to and after use for naphthalene steam reforming led the authors to believe that Cr alloying geometrically rearranges the nickel crystal planes and consequently the

electronic properties of the catalyst such that catalyst deactivation due to coke deposition is minimized.

Group VIII metals are common dopants (promoters). Jeong et al. investigated Ru-doped nickel catalysts in steam reforming reaction of methane [84]. They found the addition of Ru to decrease the amount of coke formation on the catalyst surface by suppressing the carbon chain growth through the reduction of nickel-oxides, and stabilization of the reforming activity. Nikolla et al. tried to find a Sn/Ni bimetallic catalyst that was resistant to coke formation. Since the energy barrier of carbon diffusion through monometallic nickel catalyst is very low (0.5 eV), C-C bonds can be readily formed on the carbon nucleation centers on the catalyst. DFT calculations predicted that the addition of tin to nickel catalysts would increase the energy barrier of carbon diffusion through the catalyst, while leaving the oxygen diffusion barrier unchanged. Hence formation of CO through oxygen diffusion would be more energetically favourable than C-C bond formation, making the catalyst more resistant to coke formation (Fig. 2.16). This was later verified experimentally [85].

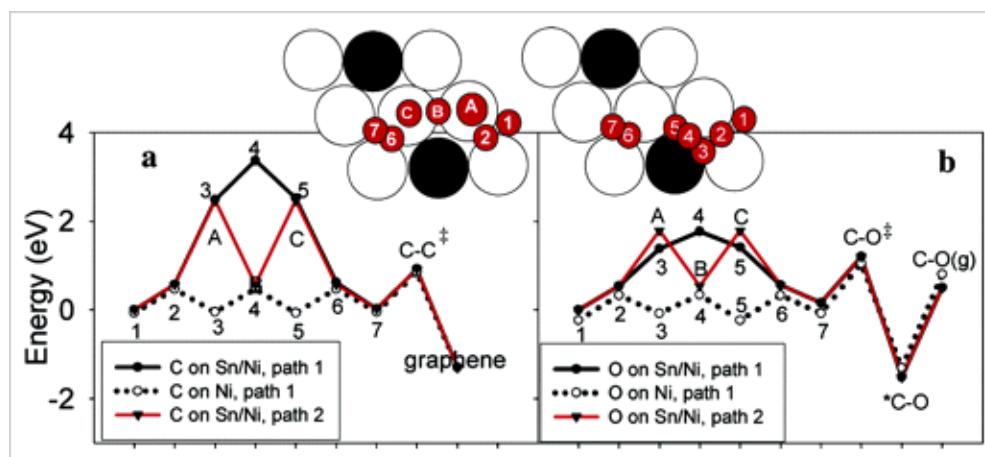


Figure 2.16: Energy barrier for carbon and oxygen diffusion on the monometallic Ni catalyst and bimetallic Sn/Ni catalyst. Reprinted with permission from American Chemical Society. Copyright (2006) American Chemical Society [85]

2.6.4 Fe-based Catalysts

Iron is one of the most abundant elements on the earth and is well known for catalyzing many industrial reactions such as the Fischer-Tropsch synthesis, the water-gas-shift reaction, as well as the ammonia synthesis among other applications [86]. Numerous recent studies have found iron-containing catalysts to be effective in reforming gasification tar. Some of these are summarized below.

Tamhankar et al. [16] were among the first to test these catalysts for tar removal. They examined the conversion of benzene using an iron-oxide/silica catalyst in the presence and absence of hydrogen gas. At a reaction temperature of 650°C, the authors found the conversion of benzene to be ~40% in a N₂ environment. Complete conversion was achieved when 9.3 vol.% H₂ with balance N₂ was added to the system. The authors found that in the absence of hydrogen, hematite (iron (III) oxide) was only reduced to magnetite, while in the presence of H₂ the magnetite phase was further reduced to metallic iron. Hence the authors concluded that the latter is the main active phase of the catalyst in reforming benzene. To further test this effect, they conducted a few more experiments on pre-reduced iron oxide catalyst particles— again with and without hydrogen gas in their reaction system. In the original iron-oxide catalyst, the initial benzene conversion started at 80% and improved to 100% conversion after 2 hours when hydrogen was used in the system. With the pre-reduced catalyst, however, the authors found the initial conversion of benzene to be 100% from the beginning regardless of the presence or absence of hydrogen [16].

There were significant differences in the deactivation rate of the catalyst between the two reaction environments tested. In the nitrogen environment, the catalyst started to deactivate within 2 h of experimentation; however, when hydrogen was present in the system the conversion level stayed high during 9 h of testing. According to the authors, this was a strong indication that hydrogen was not directly involved in the cracking

reactions of benzene on the catalyst, but rather in reactions with the intermediate coke precursors to produce methane. This would hinder catalyst deactivation by keeping the surface of the catalyst clean from coke. Moreover, methane was the only compound that could be identified in the product stream. The authors believed that the reaction proceeds according to the following reaction scheme with the ring destabilization of benzene being the rate-determining step [16]:

Figure 2.17 has been removed due to copyright restrictions. It was an image of the reaction scheme of benzene cracking [87].

Polychronopoulou et al. [64] studied the steam reforming reaction of phenols over supported Fe catalysts. The authors found the phenol conversion to be in the range of 33.8-63.3% for a reaction temperature of 700°C and over a duration of 30 minutes. The study showed that the catalyst support material contributed significantly to the steam reforming reaction through water chemisorption, thereby enhancing the gasification of carbonaceous deposits to CO, CO₂ and H₂. This was found to be enhanced by increasing the degree of support basicity. In terms of reaction products, no methane or higher hydrocarbons other than benzene could be detected. The authors suggested a dual site mechanism for the reaction where the OH back-spillover from the support to iron oxide keeps the metal active phase free from coking [64]. A full schematic of the proposed reaction mechanism is depicted in Figure 2.18.

Figure 2.18 has been removed due to copyright restrictions. It was an image of the reaction scheme of phenol cracking on supported iron catalysts [87].

Based on these findings, Nordgreen et al. investigated the effectiveness of metallic iron for catalytic tar reforming in a 2006 study [17, 19]. Their thermodynamic calculations resulted in a set of operating conditions for optimized performance of iron catalysts in terms of carbon contamination and oxidation [17]. In another study, the authors tested

1.7-1.9 mm iron oxide particles in steam reforming of tar from an atmospheric gasifier. Experiments with FeO, Fe₂O₄ and Fe₃O₄ showed that iron oxides did not possess any catalytic activity in tar cracking. However, when the catalyst was pre-reduced with 40% hydrogen to metallic iron, very good carbon breaking activity was observed and neither carbon deposits nor any decline in activity was recorded over the duration of the experiment (2.5 h) [17].

Azhar Uddin et al. [21] investigated the performance of an iron oxide (Fe₂O₃) catalyst with a tar-containing stream from a micro-gasifier. The authors found that the surface area of the developed iron catalysts played an important role in tar destruction. Moreover, the addition of Al₂O₃ was found to improve the activity of the catalyst.

Noichi et al. studied the properties of mixed metal oxide catalysts such as iron-alumina, and iron-zirconia at 850°C and found the tar conversion level to be between 45 and 75%. However, the performance of the catalyst was found to decline significantly over time due to deactivation [88].

In a 2011 study, Nemanova et al. [20] investigated the performance of five iron-based catalysts with different oxygen contents. Although the authors expected the pure metallic iron catalyst to exhibit the best performance, the results indicated that the higher oxygen containing catalysts were in fact more effective at intermediate reaction temperatures (~800°C). The investigators attributed this finding to a shift from one rate-determining reaction to another with changes in temperature.

Khelfa et al. studied the gasification and pyrolysis of Miscanthus x Giganteusa biomass in the presence of hematite as a catalyst. The authors observed a significant increase in the level of their H₂ production with the use of hematite. Moreover, the catalyst was also active in the breakdown of tar molecules formed during the process, especially light organic acids and furan derivatives [22].

Min et al. [89] studied the steam reforming reaction of biomass tar with ilmenite (a naturally occurring iron ore). Synchronous fluorescence spectroscopy revealed a good activity of the catalyst, with the tar peak area decreasing by 45 and 76% at temperatures of 600 and 850°C, respectively. The authors found the catalyst to be more effective in reforming smaller-ring aromatics compared with larger-ring molecules. Moreover, the tars mainly transformed to coke at the lower temperatures tested, while at the higher temperatures they were converted to gaseous products in the presence of sufficient steam.

Koike et al. tested the steam reforming of benzene, toluene and phenol over Ni and Ni-Fe alloy catalysts. The addition of iron to the nickel catalyst was found to increase the tar reforming activity, and reduce the carbon deposition levels on the surface. The level of carbonaceous species formed during the reaction was significantly higher for phenol conversion compared with toluene and benzene [90].

2.6.4.1 Red Mud

As introduced in Chapter 1, red mud is a by-product of alumina processing via the Bayer process. The major components of red mud include Fe_2O_3 , Al_2O_3 , SiO_2 , and TiO_2 among other oxides. The exact chemical composition varies depending on the source of the iron ore, the chemical process used, etc. Table 2.5 summarizes some of the chemical compositions reported in the literature for red mud from different regions [25, 91-95].

Table 2.5: Chemical composition of red mud from various regions

Component	Region						
	Wt. %	Aughinish	India	Jamaica	Turkey	Germany	Canada
Fe ₂ O ₃	30.4	33.1	42.3	39.84	36.5	31	47.85
Al ₂ O ₃	23.6	18.2	16.4	20.24	23.8	14	20.2
SiO ₂	9.65	8.8	8	15.24	8.5	6	7.50
TiO ₂	17.85	19.6	6	4.15	13.5	23	9.91
Na ₂ O	5.3	5.8	4.6	9.43	1.8	-	8.4
CaO	6.4	2.7	9	1.8	5.3		6.22
Other	6.8	11.8	13.7	0.48	10.6	15	0
Reference	[91]	[92]	[25]	[93]	[94]	[95]	[95]

Red mud has a fine particle size distribution with 90 vol.% below the size of 75 μm with a BET surface area of 20–30 m^2/g [26]. Red mud has been studied for various catalytic applications, including:

- Hydrogenation of biomass, coal, and oil shale [96-99]
- Hydrodechlorination of tetrachloroethylene and C₂-chlorohydrocarbons [100-102]
- Catalytic combustion of methane [103]
- Recovery of sulphur from sulphurous waste gases [104]
- Reduction of nitric oxide [105]
- Conversion of waste oil to fuel [106]
- Hydrotreating of heavy crude oil [107]

Several research groups [108-114] have reported the main mineralogical phases of red mud found through powder XRD. These are summarized in Table 2.6.

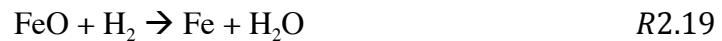
Table 2.6: Mineralogical phases of red mud found through powder XRD

Mineral phase	Chemical Formula	Mineral phase	Chemical Formula
Goethite	FeOOH	Antase	TiO ₂
Hematite	Fe ₂ O ₃	Bayerite	Al(OH) ₃
Iron hydroxide	Fe(OH) ₃	Boehmite	AlO(OH)
Magnetite	Fe ₃ O ₄	Pervoskite	CaTiO ₃
Rutile	TiO ₂	Gibbsite	Al(OH) ₃
Quartz	SiO ₂	Calcite	CaCO ₃

The temperature programmed reduction profile of red mud is depicted in Figure 2.19. The first peak occurs at lower temperatures (<200°C) and corresponds to the loss of water. The second peak occurring at 270-400°C corresponds to the reduction of Fe₂O₃ to Fe₃O₄ according to:



The third broader peak observed in the TPR profile, at temperatures of 400-850°C consists of four unresolved peaks, corresponding to the reduction of Fe₃O₄ to Fe as well as to FeO, and the reduction of FeO to metallic Fe [26, 101, 109, 115].



Teplov et al. [109] suggest that the fourth and last major peak observed, occurring at temperatures above 800°C and corresponding to 2.5% of the total weight loss could correspond to the transformation of Na₂O to gaseous Na.

Figure 2.19 has been removed due to copyright restrictions. It was an image of the temperature reduction profile of red mud with H₂ [109].

Ordenez et al. [101] compared the TPR profile of red mud to that of pure hematite and found that although the shapes of the observed peaks were different, the transition temperatures and the number of peaks for both materials were the same. The differences in the peak shapes were attributed to diffusional differences between red mud and pure hematite, and it was concluded that the reduction properties of red mud are only affected by the hematite content.

To the best of my knowledge, Dr. Jale Yanik and her collaborators at Ege University in Turkey are the only group who have tested red mud in catalyzing tar-reforming reactions. In a 2014 paper, that group tested red mud and 50% Fe₂O₃/50% CeO₂ catalysts in reforming tars from gasification of walnut and almond shells. When no catalyst was used in the system, the thermal tar cracking conversion was found to be 58.6% and ~90% at temperatures of 600 and 700°C, respectively. While the use of Fe-Ce catalyst improved the tar conversion level to 94.8% and 100% at these temperatures, the use of the red mud catalyst was only effective in slightly improving the conversion from 58.6% to 68.3% at 600°C, and did not result in any changes at 700°C compared with thermal cracking [116]. In a second study, the same group tested the activities of red mud and 10% Fe₂O₃-90% CeO₂ in steam gasification of three types of algal biomass. The authors found Fe-Ce to be more catalytically effective than red mud in converting tars. For two of the three algae tested, the authors found the tar conversion level to increase from 70% (for thermal tar conversion) to ~80% with the red mud catalyst, and to 100% with Fe-Ce. For the third biomass type, the conversion increased from ~44% to 50% and 70% with red mud and Fe-Ce, respectively.

2.7 Catalyst Deactivation

Development of catalysts that are resistant to coking and sulphur poisoning (mainly H₂S) is often performed simultaneously. Some of these methods were touched upon in the previous sections. Once present in the reaction environment, sulphur atoms can reversibly or irreversibly bind to metal sites and form metal sulphides. The three main modes of deactivation in most tar reforming catalysts include:

- Chemical deactivation due to
 - (i) Carbon deposition on the surface of the catalyst (coking)
 - (ii) Surface poisoning due to sulphur or other inorganic contaminants such as Cl and P, all of which can decrease the stability of the catalyst
 - (iii) Loss of active metal by diffusion in the support matrix [4, 44, 48]
- Mechanical deactivation due to plugging and fouling inside the pores.
- Thermal deactivation as a results of:
 - (i) Sintering
 - (ii) Phase changes in the catalyst, leading to loss of surface area and activity [68]

Chapter 3

Experimental

This chapter includes a description of the tar cracking experimental set-up and the catalyst preparation method, as well as an overview of the reaction process, the experimental procedure and the sample analysis method. The analytical techniques used for catalyst characterization are also described in more detail.

3.1 Catalyst Preparation

Red mud was obtained from Rio Tinto Alcan's Arvida R&D Centre in Jonquiere, Canada, as a by-product of the extraction of alumina from bauxite. The typical composition of red mud, its identified surface metal oxide phases, and other physical properties were provided by the supplier and are presented in Table 3.1. Note, that this composition varies with the red mud source and the composition of the bauxite itself, but it is always mainly composed of Fe_2O_3 and Al_2O_3 together with other alkali metal oxides. When the red mud was received, it was approximately 50% (w/w) red clay comprised of very fine particles (mean $5 \mu\text{m}$, with 48 % below $1 \mu\text{m}$, and 70% below $10 \mu\text{m}$). The malleable nature of the as-received red mud made forming small catalyst particles somewhat difficult.

After attempting various pre-conditioning methods to achieve uniform catalyst particles on the sub millimeter scale, the following method was selected. The red mud was dried in an oven at 110°C for 24 h. When dehydrated, the brittle red mud was ground in a mortar and pestle to generate a powder. 30 g of red mud powder was then mixed with 1 g of Sesbania powder as a binder. Sesbania gum originates from India and is extracted from

natural Sesbania plant seeds. 10 mL of distilled water was added together with 2 mL of 1 molar HCl acid, while continuously stirring the powder until a gum-like viscosity was achieved.

The red mud gum was inserted into a pelletizing machine to produce red mud pellets with a diameter of 2 mm and a length of 7.5 mm. The final particles were then dried at 120°C for 4 h to remove the free water and nitric acid. After that, the samples were first dried at 200°C for 2 h to remove chemically absorptive water, then heated to 300°C for 3 h to remove most of the binder, and finally to 350°C for 1 h to burn the residual binder.

Table 3.1: Typical elementary composition, metal oxides and other physical properties of the Alcan red mud, provided by the manufacturer

Red mud	wt.%
Al_2O_3	12-25
Fe_2O_3	30-40
SiO_2	10-20
TiO_2	3-8
CaO	1-6
Na_2O	5-10
H_2O (Chemical)	10
<i>Particle size</i>	10-250 μm
Density (dried)	3.0-3.5 g/cc
Specific surface area	10-40 m^2/g
Alkalinity	pH 14

3.2 Experimental Set-up

Bench-scale screening of the red mud catalyst was conducted in the tar cracking unit (TCU) that had been previously designed and fabricated in the Clean Energy Research Centre (CERC) high head lab at UBC. Naphthalene was used as the model tar compound since it is one of the major components in biomass gasification tar at temperatures above 900°C. Due to its low reactivity towards cracking and reforming reactions, naphthalene is viewed as one of the most difficult tars to destroy.

The tar cracking unit, depicted in Figure 3.1, consisted of a 30 mm ID by 600 mm long quartz tube reactor (QR) housed in a tubular electrical furnace (TF) that could be heated to temperatures above 1000°C. The unit inlet port consisted of 3 mass flow controllers to provide N₂ gas for the tar vaporizer (TV) unit, H₂ gas, and an additional inflow of N₂ to adjust the desired tar concentration. The temperature was utilized to control the naphthalene generation rates.

All gas lines following the tar introduction were heated with electrical heating tapes (312 W) to prevent condensation prior to reaching the reactor. The unreacted tar, products of the reforming reaction, as well as the permanent gases, left the reactor at the bottom. The reactor exit line was heated to 300°C to prevent tar condensation in the exit line

To simplify the discussion, the setup is divided to four sections. A description of each section is presented below.

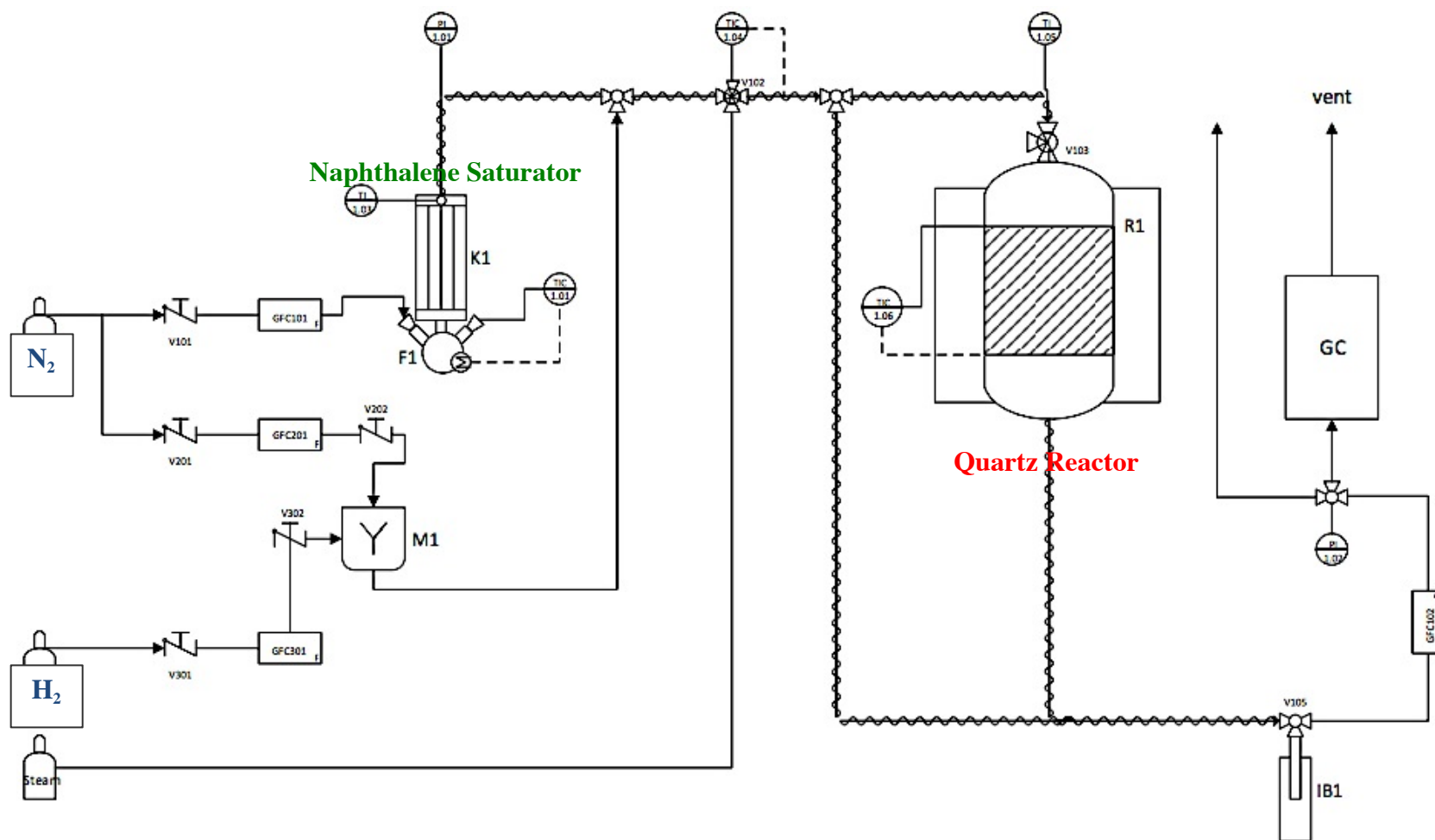


Figure 3.1: Process flow diagram of the tar cracking unit

1 Although a steam line was added to the experimental set-up, it was not used for any of the experiments described in this dissertation.

I. Tar vaporizer (TV) unit

The tar vaporizer consisted of a round-bottom flask connected to a condenser. The flask was half-filled with the model tar compound (naphthalene) and was placed in a hot bath of glycerol to maintain the temperature at 53°C. The temperature of the flask was measured with a k-type thermocouple, and the collected temperature data were logged in the system at intervals of 15 seconds. The vaporized naphthalene was carried from the flask to the following units with a controlled flow of nitrogen gas entering through the flask at a rate of 35 mL/min. The amount of tar fed to the reactor needed to be precisely controlled. Since the feeding system relied on the evaporation rate of naphthalene, the temperatures of the flask and the condenser attached to it needed to be maintained carefully in order to avoid any disruption of the system equilibrium. The condenser temperature was maintained at 90°C by passing hot water from a heating bath through the outer tube. An additional 350 mL/min of carrier gas was added to the gas stream leaving the condenser outlet. This carrier gas consisted of pure N₂ (purity 4.8) in the inert catalytic tests, and of 13 vol.% H₂ with balance N₂ in tests where the effect of catalyst reduction was investigated.

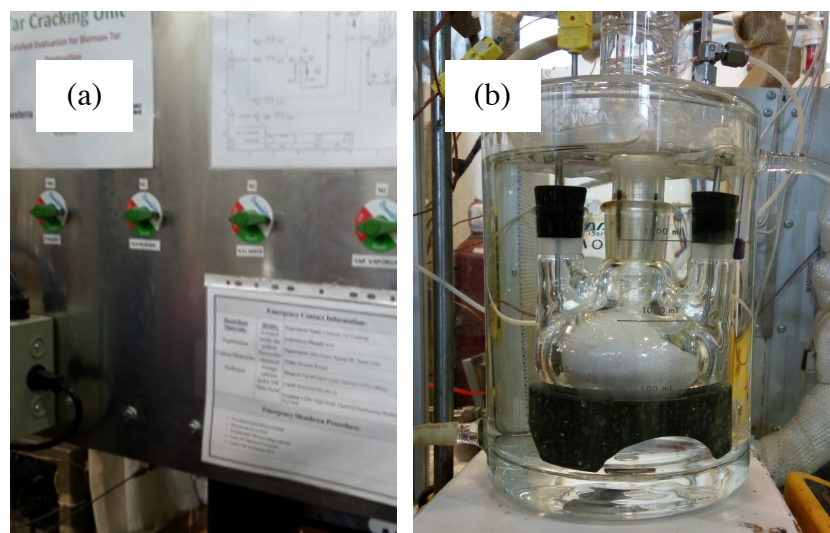


Figure 3.2: a) The tar vaporizer including the round-bottom flask and the condenser; b) The gas injection panel

II. Feed concentration evaluation

After the initial phase of the project, the experimental setup was modified slightly to allow for direct measurement of the amount of tar evaporated from the TV unit. For the benchmark tests, the preliminary red mud tests, as well as the thermal cracking tests, the older version of the setup was used where the theoretical amount of naphthalene feed was calculated from the equilibrium vapour pressure curve of naphthalene (Appendix A), and this value was used to calculate the degree of naphthalene conversion.

Before carrying out any of the many catalytic tests, a bypass line was added to the system, and the experimental procedure was modified slightly: during the first hour of experimentation, the naphthalene-containing gas stream from the TV unit was passed through the bypass line without going through the catalyst-containing reactor. This allowed for direct measurement of the feed concentration prior to every test. To ensure that the amount of feed remained constant throughout the experiment, the gas stream was once again passed through the bypass line during the last hour of the experiment. The temperature of the bypass line was maintained at 300°C to avoid any tar condensation or reaction.

Due to instabilities in the system, naphthalene concentration during the first and last hour through the bypass line did not match in some experiments, indicating that the rate of naphthalene feed had not been constant throughout those tests. Hence, the results of such experiments had to be disregarded in the final analysis.

III. Reactor and furnace

The reactor consisted of a 30 mm ID by 600 mm long quartz tube. This tube was placed inside a Lindberg M series tubular furnace. The amount of catalyst added to the reactor was adjusted based on the desired gas space velocity (Table 3.2). For enhanced heat transfer, inert mesh 12 SiC particles were placed equally below and above the catalyst to make a total bed height of 90 mm (including the catalyst height).

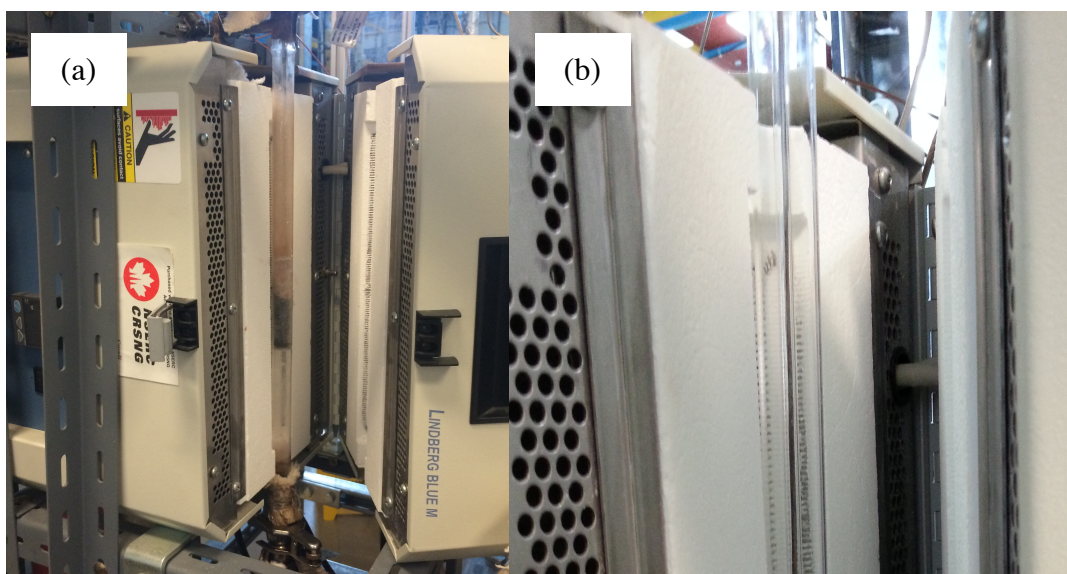


Figure 3.3: a) Reactor vessel and the furnace; b) Reactor vessel with thermocouple

IV. Tar collection and analysis

The outlet gas from the reactor entered an impinger bottle filled with 200 mL of acetone. This bottle was placed in dry ice and was cooled to -60°C to condense unreacted naphthalene as well as other reaction products as the gas bubbled through the acetone. Every hour, three samples were collected from the impinger bottle. The samples were then analyzed using gas chromatography coupled with a mass spectrometry detector (GC-MS) to determine the concentration of the components condensed in acetone. The GCMS

used was a Shimadzu model QP-2010S, equipped with a RXI-5MS column and AOC-20i auto-sampler. The remaining non-condensables, together with the permanent gases exiting from the bottle, first passed through a mass flow meter to measure the exit gas flow rate, and were subsequently sent to a Mandel 8610C GC for further analysis. All connection lines in the system including the reactor exit line were heated to 300°C to avoid condensation.

The operating conditions used in the tar cracking tests are summarized in Table 3.2.

Table 3.2: Operating conditions for naphthalene conversion tests

Parameter	Unit	Value					Value				
Carrier gas		N ₂					13 vol.% H ₂ in N ₂				
Flow MFC1	L/min	0.035					0.035				
Flow MFC2	L/min	0.350					0.300				
Flow MFC3	L/min	0					0.050				
Reactor ID	cm	15					15				
Catalyst mass	g	1.91	2.13	2.69	3.85	5	1.91	2.69	3.85	5	
Bed height	mm	7	14	20	25	29	7	20	25	29	
Space velocity	h ⁻¹	18674	9337	6536	5229	4500	4500	6536	5229	4500	
Temperatures	°C	500-800					500-800				
Feed concentration	g/h	0.014 ± 0.002					0.014 ± 0.002				
Experimental time	h	1					1				

3.3 Activity Calculation

The weight of the acetone added to the impinger bottle, as well as all samples taken during the experiments were recorded. From the measured concentration of naphthalene in the samples with the GC-MS, the net mass of naphthalene collected in the bottle during each sampling interval was calculated. This was subsequently used to calculate the reactant conversion:

$$X (\%) = \left(1 - \frac{(m_1 - \Delta m_i)}{m_1} \right) * 100$$

where m_1 is the mass of naphthalene fed to the system measured through the bypass line during the 1st hour of the experiment, and Δm_i is the net mass of naphthalene condensed in the impinger bottle during each sampling interval. More details on the naphthalene conversion calculations can be found in Appendix C.

3.4 Characterization Techniques

When testing with heterogeneous materials such as red mud, characterizing the surface area, structure and composition of the catalyst is critical in investigating the source of catalytic effects. The red mud catalyst was thoroughly characterized before and after preconditioning the raw material, as well as before and after exposure to naphthalene at temperatures of 500-800°C using the following analytical techniques.

3.4.1 Brunauer–Emmett–Teller (BET)

The surface area and pore size distribution of the catalyst were measured for the as-received red mud, the prepared red mud pellets, as well as the spent catalyst by means of nitrogen adsorption-desorption isotherms at 77 K in a Micromeritics AutoChem II 2920 equipment. Prior to measurements, the samples were degassed for 12 h at 250°C. The amount of nitrogen adsorbed at a relative pressure of $p/p_0 = 0.01$ to $p/p_0 = 0.98$ was used

to evaluate the total surface area and pore volume, respectively. The surface area was determined using the Brunauer-Emmett-Teller (BET) theory. The effects of calcination temperature, as well as catalyst reduction by H₂ were also investigated.

3.4.2 Powder X-ray Diffraction (XRD)

This technique was used to provide information about the nature of the constituent crystalline phases, and to investigate the changes occurring in the red mud after exposure to naphthalene at the reaction temperatures tested. For this analysis, a Bruker D8 Advance X-ray diffractometer (in Bragg-Brentano configuration) with LynxEye silicon strip detector and a Ni filter was used. Copper radiation (Cu K α_1 and K α_2) was generated using a 2.5° soller slit at 40 kV and 40 mA, and the patterns were collected over the angular range of 5° to 89.9° with a step size of 0.039°. To reduce the detection of fluorescence, the discrimination lower level was set to 0.19 and the window width was set to 0.06 for the LynxEye detector.

Before analysis, all samples were dried, ground with a mortar and pestle, and packed in a shallow well sample holder; crystalline phases were identified with a search-match procedure using the ICDD PDF-2 database. All XRD measurements were carried out by the Chemistry Department at the University of British Columbia.

3.4.3 Scanning Electron Microscopy (SEM)

The microscopic structure and the qualitative physical changes of the red mud due to calcination, acid pre-treatment and catalytic tar cracking were analyzed using a Hitachi S3000N scanning electron microscope (SEM). The red mud samples were coated in gold (Edwards S150A sputter coater) for one minute in order to increase the electric conductivity. The samples were analyzed in a high vacuum environment.

3.4.4 Thermogravimetric Analysis (TGA)

Thermogravimetric analysis (TGA) was performed using a TA instruments Q600-SDT thermal analyzer in the Bioenergy and Fuel Research laboratory in the Department of Chemical and Biological Engineering at UBC. Measurements were carried out in Shimadzu alumina crucibles. During each run ~15.9 mg of sample was heated from room temperature to the final target temperature at a rate of 10°C/min under a nitrogen flow of 100 mL/min.

3.4.5 X-ray Photoelectron Spectrometry (XPS)

XPS analysis was performed to determine the composition of the catalyst at the near-surface region, as well as to determine the oxidation states of the iron oxide present. The analysis was performed using a Leybold MAX200 instrument. The X-ray source was Al K-alpha. The area of the analyzed area was 4x7 mm², and the pass energies used for the survey scan and narrow scan measurements were 192 and 48 eV respectively. All measurements were carried out by the Interfacial Analysis and Reactivity Laboratory at the Department of Chemistry at UBC.

3.4.6 CHN Analysis

CHN analysis involves the combustion of a pre-determined amount of sample material in oxygen. The resulting N₂, CO₂ and water species generated in the process are analyzed by thermal conductivity detection (TCD), and are compared with known standards (acetanilide and nitroaniline). The instrument used for the analysis was a Carlo Erba Elemental Analyzer Model 1106 with a Mettler Toledo UMX2 Analyzer.

The technique adopted is based on a modification of the classical Pregl and Dumas method. “The samples are held in a lightweight tin container and dropped at preset

intervals of time into a vertical quartz tube, maintained at 1030°C, through which a constant flow of helium is run. When the samples are introduced, the helium stream is temporarily enriched with pure oxygen. Flash combustion takes place, primed by the oxidation of the container. Quantitative combustion is then achieved by passing the mixture of gasses over Cr_2O_3 . The mixture of combustion gases is then passed over copper at 650°C to remove the excess of oxygen and reduce oxides of nitrogen to nitrogen. It then passes through a chromatographic column of Porapak QS heated to approximately 100°C. The individual components are then separated and eluted as N_2 - CO_2 - H_2O . They are measured by a thermal conductivity detector, whose signal feeds a potentiometric recorder and in parallel an integrator with digital printout. The instrument is calibrated by combustion of standard compounds.”[117]All measurements were performed by Canadian Microanalytical Service Ltd located in Delta, British Columbia.

3.4.7 X-ray Fluorescence Spectrometry (XRF)

XRF was used to determine the bulk composition of the major oxides in the catalyst. The analysis was performed using a PanAnalytical Axiosfast WDXRF spectrometer. A predetermined amount of sample was heated to determine the loss on ignition (LOI). The sample was then fused in a platinum-gold crucible with a commercial lithium tetraborate flux. The molten material was cast in a platinum mold and fused discs were analyzed by XRF. All measurements were carried out by the analytical testing, inspection and certification company, Bureau Veritas Canada located in Vancouver, BC.

Chapter 4

Results and Discussion

This chapter presents the experimental results obtained from naphthalene cracking tests and catalyst characterization. The chapter is divided into two sections: first a summary of the preliminary test results, including the baseline test, the benchmark test, as well as preliminary test results with red mud is provided; this is followed by the results from the extensive tests performed on red mud both under inert conditions and in the presence of H_2 .

Preliminary Test Results

4.1 Baseline Tests

In order to verify that the amount of naphthalene fed to the reaction system remained constant throughout the testing period, multiple baseline tests were performed prior to conducting any experiments with the red mud catalyst. Baseline tests were repeated at various points in the project to ensure the stability of the naphthalene feeding system. The results from these tests are presented in Fig. 4.1. The net hourly amount of naphthalene fed remained relatively stable over the testing period in each test; however, due to slight differences in the system temperature there were small but noticeable differences among the different tests conducted. From theoretical calculations (Appendix A), a temperature difference of 0.5°C , for instance, results in $\sim 4.2\%$ difference in the amount of naphthalene evaporated. These differences between the various baseline tests are reflected in Fig. 4.1. As mentioned in Section 3.2, to double check that the naphthalene

feeding rate remained constant throughout each experiment, a bypass line was added to the experimental set-up and the first and last hour amounts of naphthalene feed rate were compared at the end of each experiment as a second check to ensure stability.

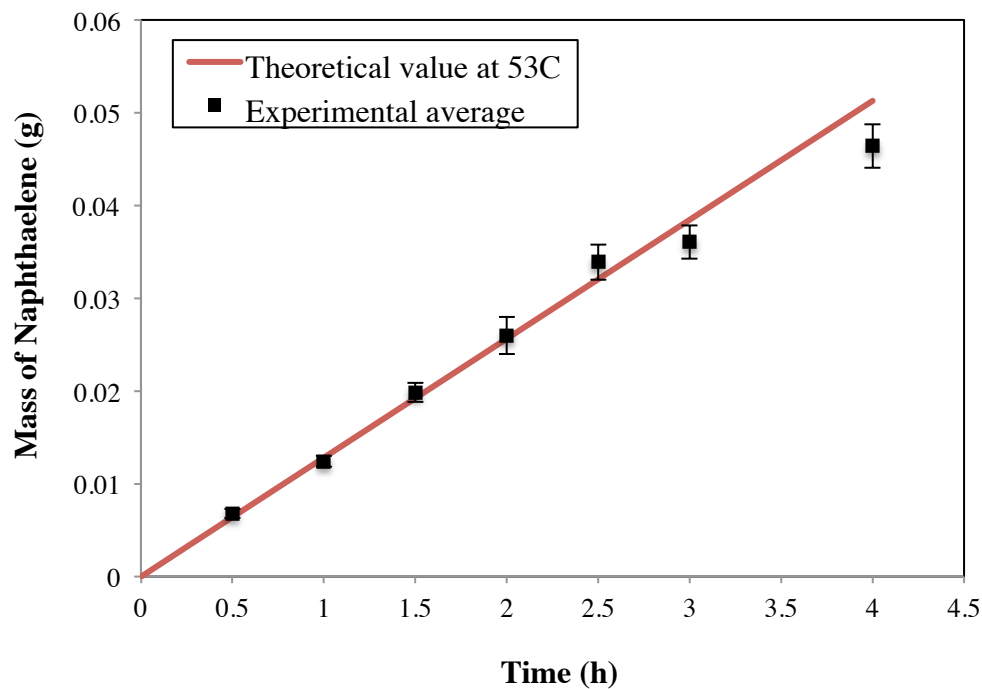


Figure 4.1: Results from the baseline test with naphthalene

The theoretical amount of naphthalene present in the gas phase carried to the reaction system is calculated from the vapour pressure curve of naphthalene (Appendix A). This theoretical value is compared with the actual amount of naphthalene measured during the baseline test in Fig. 4.1.

4.2 Benchmark Tests

As mentioned in Chapter 1, this project is a collaboration between the Fraunhofer Institute and UBC with the aim of developing an effective economic catalyst for tar removal from gasification syngas.

Prior to testing the catalyst, it was crucial to ensure that the experimental setups at UBC and the partner institutes at Fraunhofer (ISE and UMSICHT) have very similar performance in order to be able to compare experimental results. Thus, benchmark tests were performed at all three institutions with an industrial Ni-based catalyst from Johnson-Matthey to ensure that similar results could be obtained from all three experimental units. The tests were performed for a duration of four hours at a temperature of 850°C and a space velocity (SV) of 19,000 h⁻¹ for the naphthalene conversion tests, and a space velocity of 4500 h⁻¹ for the benzene cracking experiments. A summary of the agreed upon benchmark test parameters can be found in Appendix B. Note, that space velocity (SV) is defined as the feed volumetric flow rate divided by the volume of the catalyst in the packed bed reactor:

$$SV = \frac{\dot{V}}{V_{cat}} \quad E4.1$$

Fraunhofer ISE performed benchmark tests using both naphthalene and benzene as their model tar compound; while, Fraunhofer UMSICHT only tested benzene, and UBC only naphthalene. The results of the benchmark tests from all three institutions are presented in Figure 4.2.

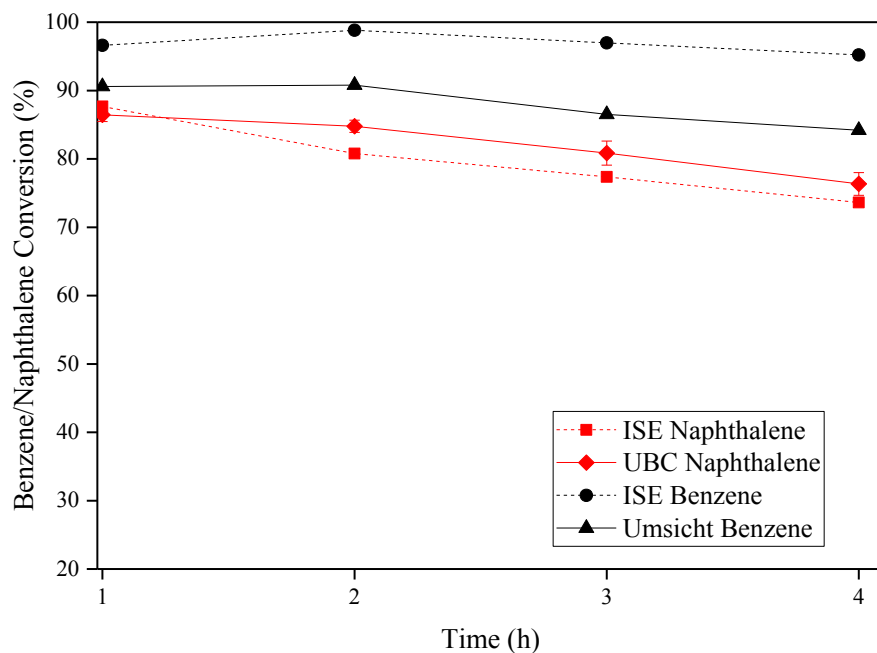


Figure 4.2: Results from the benchmark tests performed at UBC, Fraunhofer ISE and Fraunhofer Umsicht on an industrial Ni catalyst at 850°C and SV of 19,000 and 4500 h⁻¹

As can be seen, the experimental results obtained by Fraunhofer ISE and UBC for naphthalene conversion were in good agreement with less than 3% difference in conversion. On the other hand, the ones from Fraunhofer UMSICHT and ISE for benzene differed by up to 10% in conversion.

4.3 Thermal Cracking

In order to differentiate between thermal and catalytic cracking, the degree of thermal naphthalene conversion was determined by feeding the reactant through the empty reactor column. An inert bed of mesh 12 SiC particles was placed inside the reactor to assure the same space velocity as for the catalytic cracking tests (SV = 19,000 hr⁻¹). The

tar concentration (~ 100 ppmV) and the volumetric flow rate were kept the same as for the catalytic cracking tests. The temperature in the quartz glass reactor was increased from 650°C to 1050°C in steps of 100°C . Naphthalene conversion was then measured at each temperature (Fig. 4.3). The results showed almost no thermal naphthalene conversion up to a temperature of 850°C . This value increased to 15% at 950°C and eventually to 58% naphthalene conversion at 1050°C . These findings are comparable to the findings of Jess [118] who found no thermal conversion at temperatures below 900°C and 58% conversion of naphthalene at 1200°C . The difference in findings was most probably due to a 40% shorter residence time of the feed gas in the heating zone of the set up used by Jess. Shorter residence times in the cracking zone are known to demand higher temperatures to decompose tar molecules successfully.

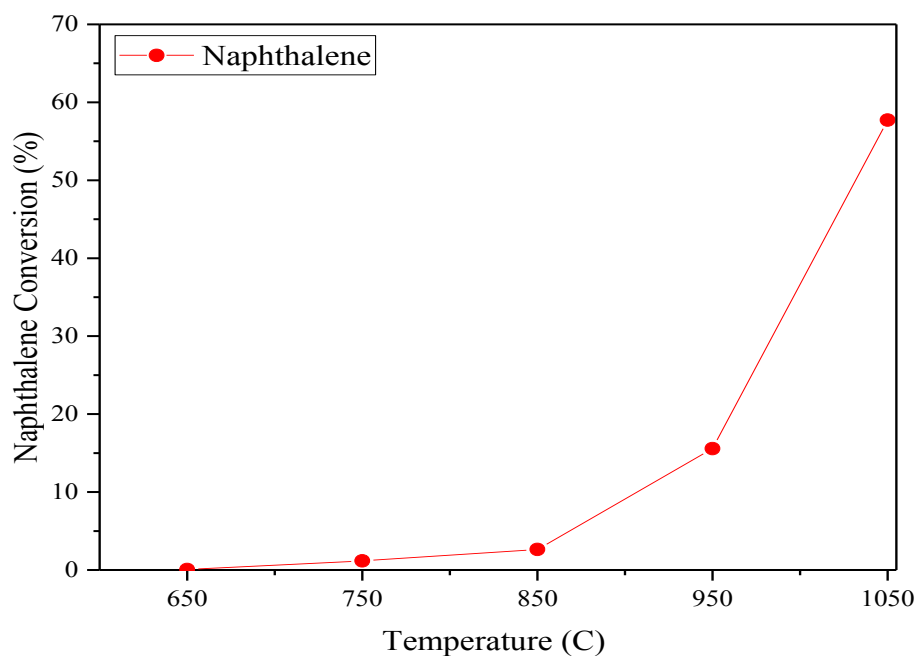


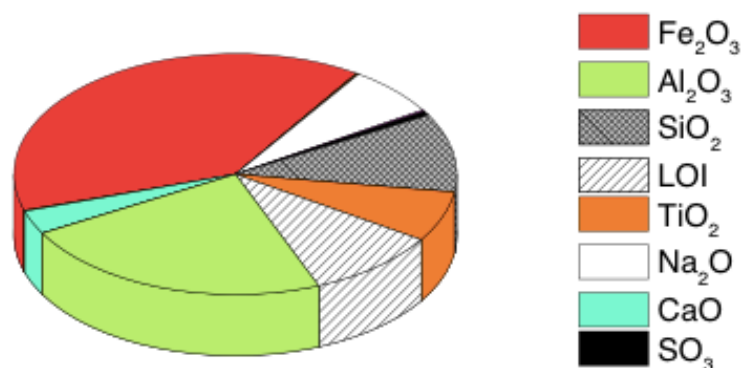
Figure 4.3: Degree of thermal naphthalene conversion in the reactor at temperatures of 650 - 1050°C at a space velocity of $19,000\text{ hr}^{-1}$

The results from the thermal cracking tests further prove that thermal tar removal processes require high temperatures of above 900°C and indicate the need for a catalyst to decompose tars at temperatures < 900°C.

All the subsequent catalytic cracking tests were performed in a temperature range of 500–850°C, for which the degree of thermal cracking is < 5% (Fig. 4.3).

4.4 Preliminary Tests with Red Mud

Once the benchmark and thermal tar cracking results had been completed, the second phase of the project –red mud catalyst testing was initiated. In order to determine the bulk chemical composition of the red mud catalyst, X-ray fluorescence analysis (XRF) was performed on an as-received red mud sample. All measurements were carried out by Bureau Veritas S.A., and the results are summarized in Fig. 4.4.



Fe ₂ O ₃	Al ₂ O ₃	SiO ₂	LOI	TiO ₂	Na ₂ O (%)	CaO	SO ₃	P ₂ O ₅	Cr ₂ O ₃	MgO
38.60	22.70	10.40	9.58	6.70	6.61	3.12	0.59	0.19	0.14	0.12

Figure 4.4: Bulk composition of red mud catalyst as found by XRF analysis

As can be seen the major component of the catalyst was iron oxide (38.6%), followed by aluminum oxide (22.7%) and silicon oxide (10.4%). Moreover, the measured concentrations of the oxides present in the catalyst are in line with the concentration values reported by the supplier and fall within the range reported in the literature (see Section 2.6.4.1). To gain a broad preliminary understanding of the performance of the catalyst, red mud (RM) pellets were exposed to N_2 - environment for a duration of 4 hours and their tar removal activity was compared with that of the industrial benchmark Ni catalyst which had been tested previously. The tests were carried out at a space velocity of $19,000\text{ h}^{-1}$ and temperatures of 850°C and 800°C . From the measured naphthalene concentration in the gas at the reactor inlet and outlet, the conversion was calculated for all experimental conditions. This calculated conversion includes both catalytic as well as the thermal conversion reactions studied previously.

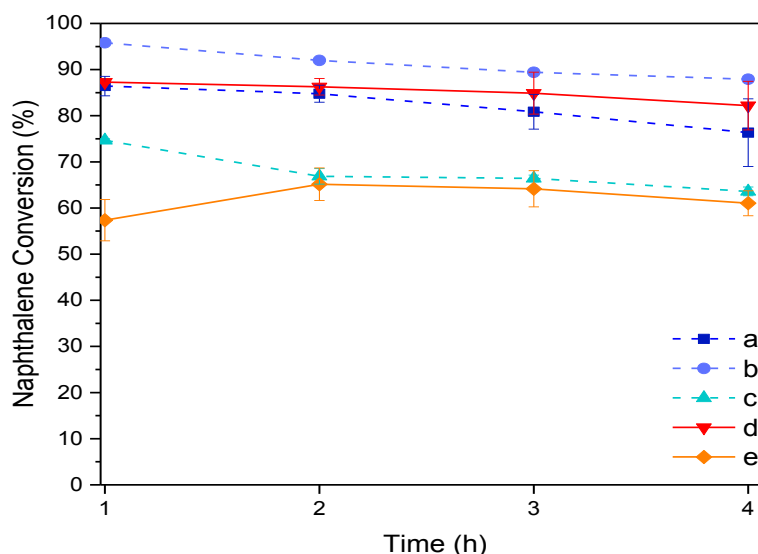


Figure 4.5: Preliminary tests results: performance of (a) Ni catalyst at 850°C and $\text{SV} = 19,000\text{ h}^{-1}$, (b) Ni catalyst at 850°C and $\text{SV} = 4500\text{ h}^{-1}$, (c) Ni catalyst at 800°C and $\text{SV} = 19,000\text{ h}^{-1}$, (d) Red mud catalyst at 850°C and $\text{SV} = 19,000\text{ h}^{-1}$, (e) Red mud catalyst at 800°C and $\text{SV} = 19,000\text{ h}^{-1}$

As can be seen in Fig. 4.5, the performance of the red mud catalyst was very similar to the Ni catalyst at both temperatures tested except for the first-hour performance of red mud at 800°C which was significantly lower than that of the Ni catalyst. The degree of naphthalene conversion was comparably better at the higher temperature tested for both catalysts, with the catalytic activity decreasing over time due to deactivation.

The effect of reactor temperature on the catalyst performance was also investigated at a space velocity of 19,000 h⁻¹ (Fig. 4.6). As expected there was a strong correlation between temperature and naphthalene conversion at the reaction conditions tested with an increase of approximately ~10% in tar conversion for every 100°C increase in reactor temperature.

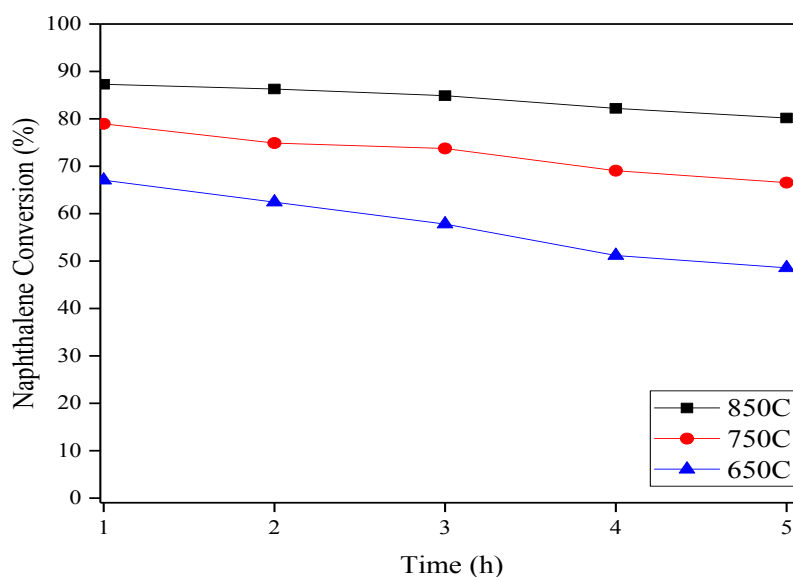


Figure 4.6: Effect of temperature on the performance of RM catalyst at a space velocity of 19,000 h⁻¹

Although the performance of the catalyst significantly increased with increasing temperature, the rate of catalyst deactivation did not seem to be significantly affected by temperature for the range of conditions studied over the testing period (5 hours).

Once the effect of temperature had been investigated, the next step was to evaluate the effect of space velocity on the reactant conversion (Fig. 4.7). This was achieved by testing the catalyst at two distinct space velocities of 4,500 and 19,000 h⁻¹ for a testing duration of 4 h at four different reactor temperatures. Lowering the space velocity by increasing the amount of catalyst in the reactor tube significantly increased the naphthalene conversion at all temperatures tested. This could be due to the fact that the retention time of the naphthalene feed was higher as the space velocity decreased. This could have resulted in increased contact time between the reactant and the catalyst, and hence the tar removal efficiency. A more extensive examination of the long-term activity of the catalyst is required to determine the effect of space velocity on the catalyst performance. Catalyst deactivation and regeneration pathway studies were not in the scope of the current project and would need to be investigated in detail in future experiments.

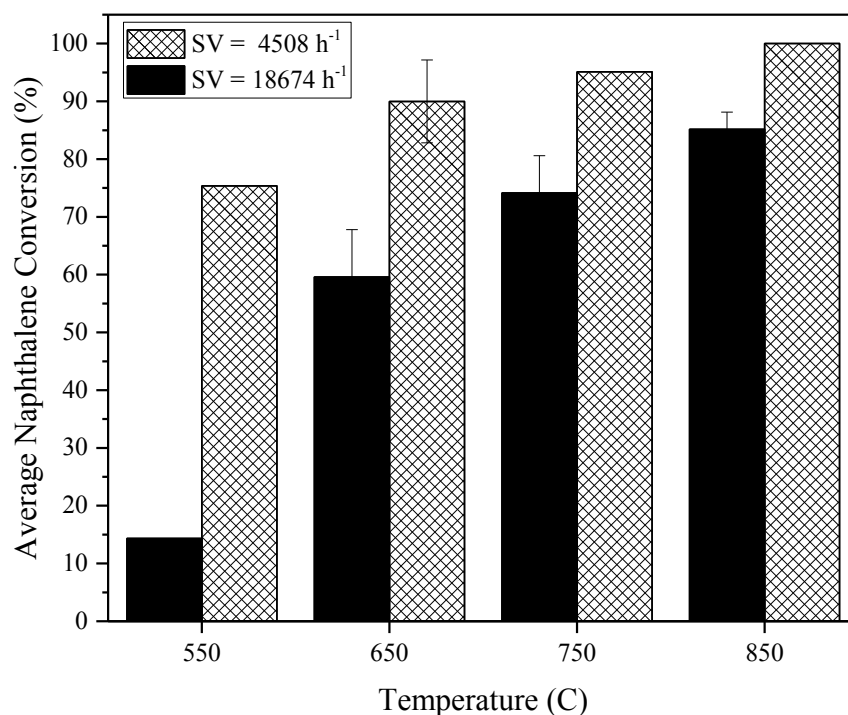


Figure 4.7: Effect of space velocity on the performance of RM catalyst over a testing period of four hours.

In Fig. 4.7, strong temperature effects can again be observed at both space velocities. While at a space velocity of 19,000 h⁻¹ and temperature of 550°C, naphthalene conversion reached an average of 14.4% (in 4 h), this value increased to 59.6% and 74.2% at 650°C and 750°C, respectively, and reached a maximum of 85.2% at 850°C. These results are in line with the findings of Wang et al. [119], who investigated tar conversion over Fe_2O_3 powders mixed with natural dolomite. At a space velocity of 12,000 h⁻¹ they reported a tar conversion of 44% and 97% for temperatures of 650°C and 850°C, respectively. These authors attributed the high tar conversion levels to the high amounts of Fe_2O_3 in their catalyst. The difference between their and our results could be explained by the different space velocities used as well as the nature of the catalysts tested.

Overall, the red mud catalyst showed a very high intrinsic catalytic activity for naphthalene conversion even at temperatures as low as 550°C and space velocities as high as 19,000 h⁻¹.

Extensive Tests

Promising preliminary results with the red mud catalyst in the initial testing stage encouraged us to pursue further investigation of the catalyst to determine its long term activity and performance in reducing reaction environments such as those encountered with gasification syngas. The presence of reducing agents such as hydrogen could potentially have several effects on the performance of the catalyst. This could be due to the interaction of hydrogen with the catalyst surface, altering the physical and chemical characteristics by reducing the iron phase of the catalyst and affecting the surface area for instance. These surface effects are discussed in further detail in the following sections. Additionally, hydrogen could react with the intermediate reaction products and potentially change the long-term activity of the catalyst [16]. It could also change the reaction pathway and affect the kinetics of the reaction. In order to delineate these effects, all tests were initially performed in an inert nitrogen-environment before being repeated again with hydrogen. Moreover, extensive surface characterization tests were performed to better track the physical and chemical changes in the catalyst at various stages of the experiments. In order to investigate these effects the following tests were conducted:

- **Tests with N₂:** To determine the kinetics of the tar conversion reactions, the red mud catalyst was tested at four distinct temperatures and five space velocities for a duration of one hour in an inert nitrogen- environment.

- **Tests with H_2 :** The same tests were repeated in a reducing environment (13 vol.% H_2 with balance N_2) at four of the same gas space velocities as before, and the results were compared.
- **Long-term tests:** To determine the long term activity of the catalyst, red mud pellets were tested for a duration of 14 h in the absence and in the presence of hydrogen.

Detailed discussion of the findings from these tests is presented in the following sections.

4.5 Tests with N_2

4.5.1 Catalytic Activity

In order to determine the reaction kinetics of naphthalene removal, the red mud catalyst was tested at five space velocities, achieved by increasing the amount of catalyst in the reactor, at reactor temperatures of 500-800°C for a duration of 1 h. At the end of each hour, the conversion of the naphthalene was determined and the results were plotted for all reaction conditions tested in Fig. 4.8.

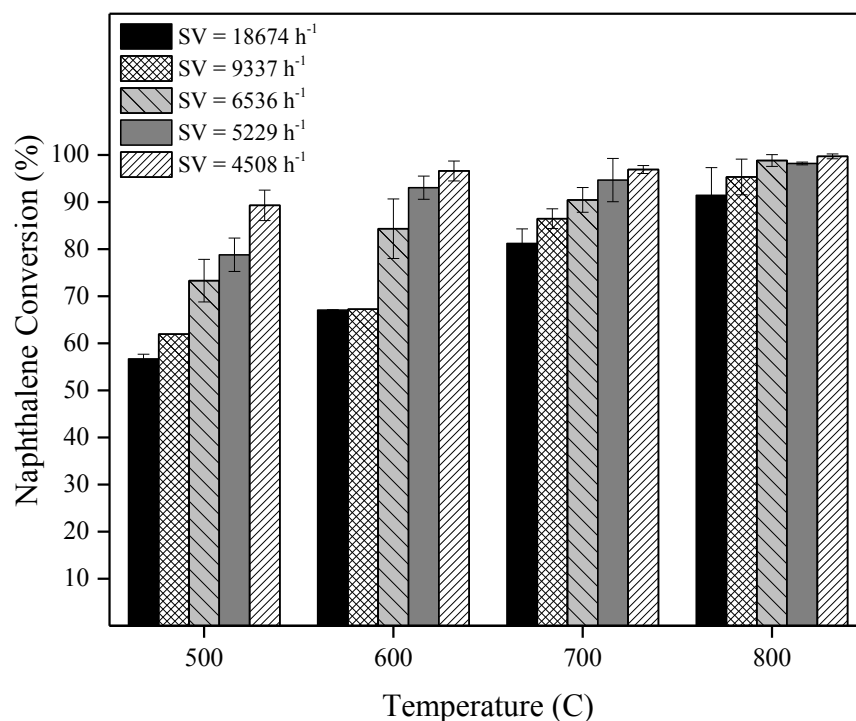


Figure 4.8: Effect of space velocity and temperature on naphthalene conversion in pure N₂-environment at space velocities of 4500-19,000 h⁻¹ and temperatures of 500-800°C

As can be seen, increasing the temperature, and increasing the space velocity both resulted in an increase in naphthalene conversion, which is consistent with the preliminary test results. Moreover, it can be seen that the gas space velocity had a less pronounced effect on improving the catalyst naphthalene removal activity at the higher temperatures tested. At a reactor temperature of 800°C for instance, the same conversion was achieved at a space velocity of 6536 h⁻¹ as with 4508 h⁻¹.

4.5.2 Kinetic Analysis

In order to determine the apparent reaction rate constant and the apparent activation energy of the cracking reaction(s), it was necessary to make several assumptions, such as steady state conditions, as well as plug flow of the feed in the reactor (Appendix H). Moreover since the amount of gaseous products formed during the reaction was very small, the volumetric flow rate in the reactor was assumed to remain unchanged. This is discussed in more detail in Section 4.8. Since determining the exact reaction path of naphthalene cracking was not in the scope of the project, the constituents were lumped into one parameter and fitted to a kinetic model. Considering the design equation of packed bed reactors, the following equations can be derived for a 1st order reaction with respect to naphthalene:

$$\frac{dF_A}{dW} = -k \cdot C_A \quad \text{E4.1}$$

Substituting for F_A and C_A :

$$F_A = F_{A0} \cdot (1 - X) \quad \text{E4.2}$$

$$C_A = C_{A0} \cdot (1 - X) \quad \text{E4.3}$$

Results in:

$$F_{A0} \left(\frac{dX}{dW} \right) = k \cdot C_{A0} \cdot (1 - X) \quad \text{E4.4}$$

$$F_{A0} = C_{A0} \cdot \dot{V} \quad \text{E4.5}$$

$$\frac{dX}{(1 - X)} = \frac{k dW}{\dot{V}} \quad \text{E4.6}$$

$$\ln(1 - X) = k \frac{W}{\dot{V}} \quad \text{E4.7}$$

Defining τ , as the mass of catalyst divided by the volumetric flow rate of the feed ($\frac{W}{\dot{V}}$):

$$\ln(1 - X) = k \cdot \tau \quad \text{E4.8}$$

If the initial assumption of the reaction being 1st order is correct, a plot of $\ln(1-X)$ vs. τ should result in a straight line with a slope of k that passes through the origin. This is shown to be so in Fig. 4.9. Hence the experimental data were first fitted into the first order kinetic model for each temperature tested. If the data did not follow the first order trend, they were fitted to higher or lower order models according to the following equation scheme:

$$\frac{dF_A}{dW} = -k \cdot C_A^n \quad \text{E4.9}$$

Substituting for F_A and C_A as before:

$$C_A = C_{A0} \cdot (1 - X) \quad \text{E4.10}$$

$$F_{A0} = C_{A0} \cdot \dot{V} \quad \text{E4.11}$$

$$F_A = F_{A0} \cdot (1 - X) = C_{A0} \cdot \dot{V} \cdot (1 - X) \quad \text{E4.12}$$

So that:

$$\frac{dX}{(1-X)^n} = \frac{kC_{A0}^{n-1}}{\dot{V}} \cdot dW \quad \text{E4.13}$$

For $n \neq 1$:

$$\frac{(1-X)^{1-n}}{1-n} = \frac{kC_{A0}^{n-1}}{\dot{V}} \cdot W \quad \text{E4.14}$$

Rearranging gives:

$$(C_{A0} \cdot (1-X))^{1-n} = \frac{k}{\dot{V}} \cdot W \cdot (1-n) \quad \text{E4.15}$$

Taking the logarithm of both sides leads to:

$$(1-n) \cdot \log(C_{A0} \cdot (1-X)) = \log\left(\frac{W}{\dot{V}}\right) + \log(k \cdot (1-n)) \quad \text{E4.16}$$

Defining the following:

$$Y = \log\left(\frac{W}{\dot{V}}\right) \quad \text{E4.17}$$

$$Z = \log(C_{A0} \cdot (1-X)) \quad \text{E4.18}$$

$$b = \log(k \cdot (1-n)) \quad \text{E4.19}$$

The equation can be simplified to a simple linear form:

$$Y = (1-n) \cdot Z - b \quad \text{E4.20}$$

Hence plotting the defined parameter Y vs. Z should result in a line, from the slope of which the reaction order, n, can be calculated. Data fittings were performed with commercial software OriginLab® that employs the Levenberg–Mardquardt algorithm. The resulting regression plots can be found in Appendix D. Once the value of n was known, the following were defined and calculated:

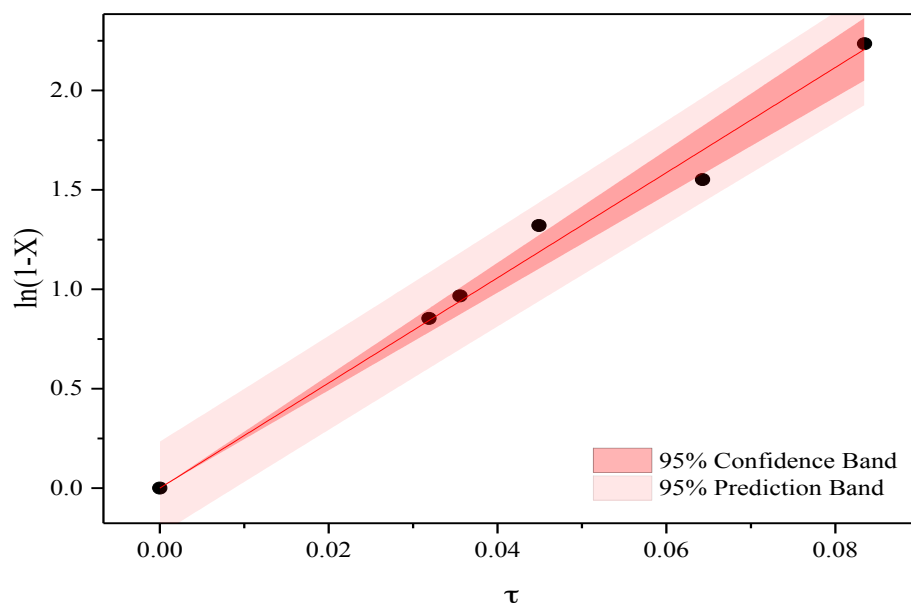
$$\tau = \frac{W.C_{A0}^{n-1}}{\dot{V}} \quad \text{E4.21}$$

$$Y_2 = \frac{(1 - X)^{1-n}}{1 - n} \quad \text{E4.22}$$

Substituting in E4.14 leads to:

$$Y_2 = \tau.k + 1 \quad \text{E4.23}$$

Hence plotting Equation E4.23, would result in a straight line with a slope of k that passes through (0,1) (Figs. 4.9-4.12). The results of this analysis are included below. Note that the higher order reaction scheme was only investigated for data sets that did not fit in the first order reaction model.



Intercept Value	Slope Value	Slope Standard Error	Statistics R-Square
0	26.44	0.73	0.995

Figure 4.9: Kinetic results of N_2 tests at 500°C ; Fitted to a first order model
($n = 1, k = 26.44 \pm 0.73$ with 95% confidence)

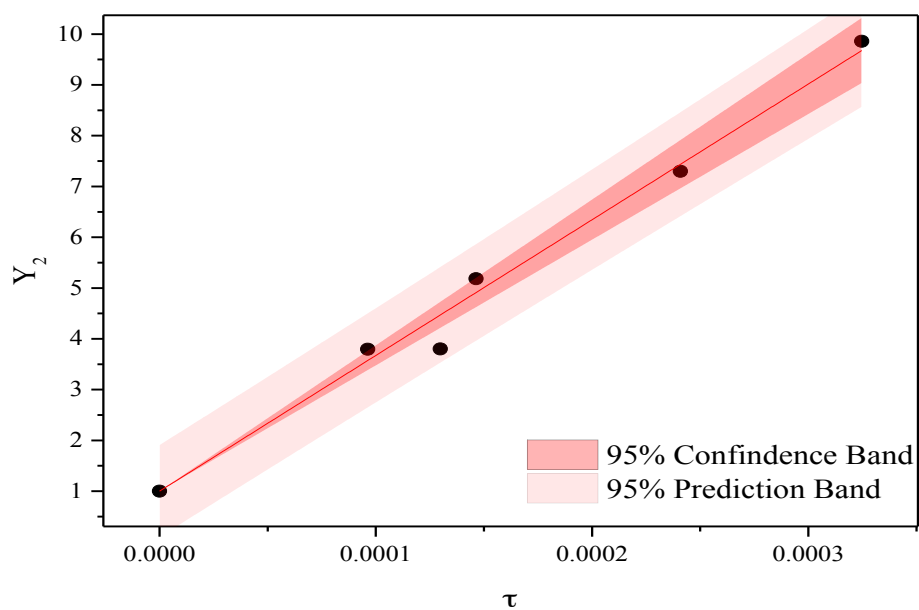
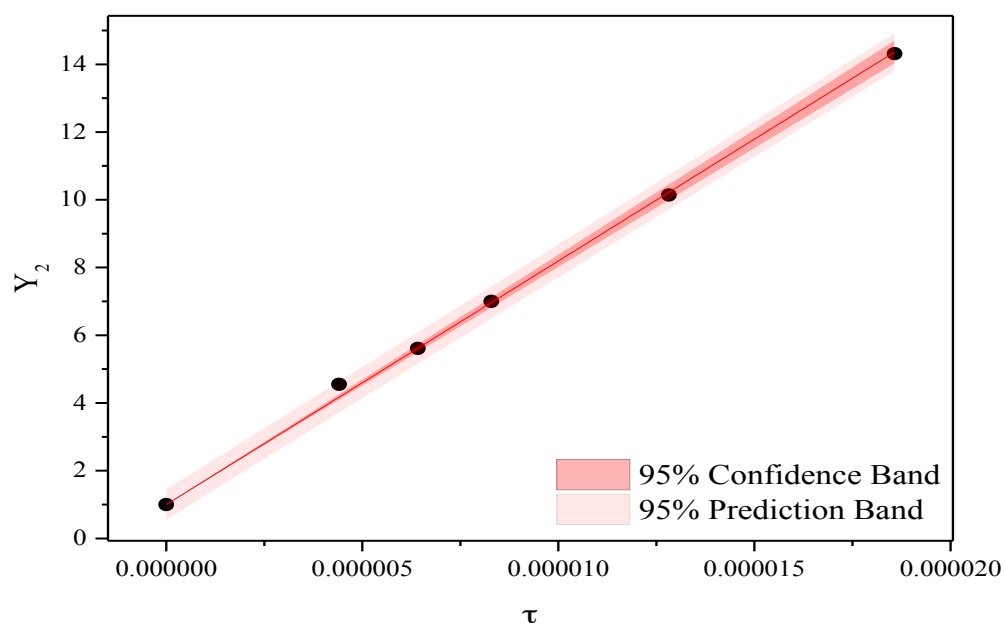


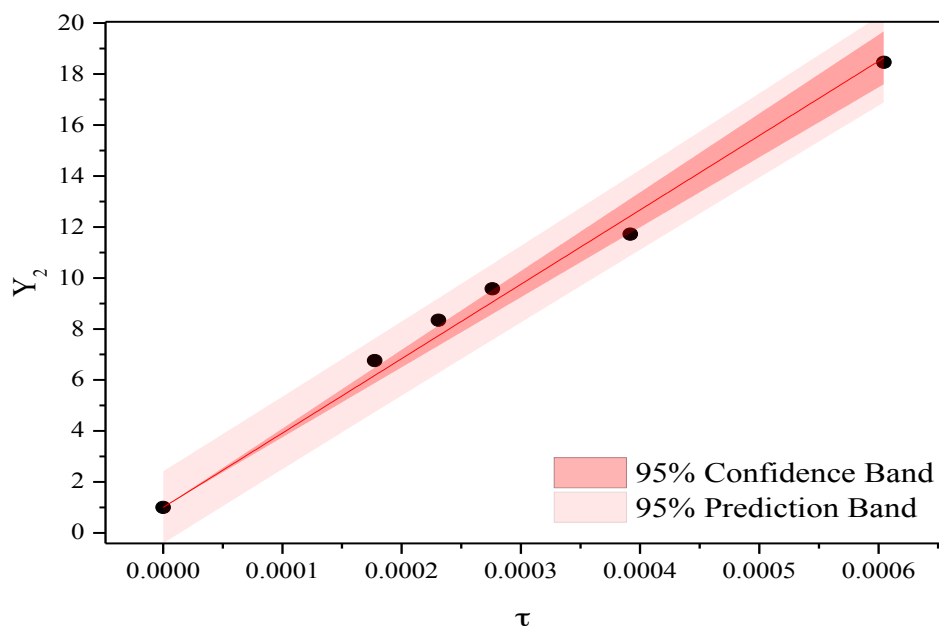
Figure 4.10: Kinetic results of N_2 tests at 600°C
 $(n = 1.42 \pm 0.06, k = 26724 \pm 768)$



Intercept Value	Slope Value	Slope Standard Error	Statistics R-Square
1	719414	6949	0.99955

Figure 4.11: Kinetic results of N_2 tests at 700°C

($n = 1.64 \pm 0.08$, $k = 719414 \pm 6949$)



Intercept Value	Slope Value	Slope Standard Error	Statistics R-Square
1	29175	667	0.99736

Figure 4.12: Kinetic results of N_2 tests at 800°C

$$(n = 1.35 \pm 0.05, k = 29175 \pm 667)$$

As can be seen in Fig. 4.9, the data from the tests performed at 500°C fitted in the first order kinetics model; however, results from tests at $600\text{--}800^\circ\text{C}$ had to be fitted in higher order reaction schemes. To do so, the raw lab data were first fitted in equation E4.20 by means of linear regression. From this, the reaction order (n) was found to be 1.42 ± 0.06 , 1.64 ± 0.08 and 1.35 ± 0.05 ¹ for temperatures of 600 , 700 and 800°C , respectively

¹ The number of significant figures in the reported values were consulted with professor J. Petkau, in the Department of Statistics at the University of British Columbia.

(Appendix D). Having evaluated the reaction order, the average values of naphthalene conversion were fitted to equation E4.23 using weighted least-square method to further confirm the accuracy of the calculated reaction orders (Figs. 4.9-4.12). The slope of each of the lines generated corresponds to the apparent reaction rate constant. Since the reaction order varied with temperature, it was not possible to fit the kinetics data in the Arrhenius equation for activation energy evaluation. A summary of the apparent reaction order and rate constants is provided in Table 4.1.

Table 4.1: Apparent Kinetic Parameters of Inert Tests for Temperatures of 600-800°C

Temperature	Parameter	Unit	Estimate	Standard Error
500°C	n		1	-
	k	$\text{m}^3.\text{kg}^{-1}.\text{h}^{-1}$	26.44	± 0.73
600°C	n		1.42,	± 0.06
	k	$\text{L}^{1.4}.\text{kg}^{-1}.\text{h}^{-1}.\text{mol}^{-0.4}$	26724	± 768
700°C	n		1.64	± 0.08
	k	$\text{L}^{1.6}.\text{kg}^{-1}.\text{h}^{-1}.\text{mol}^{-0.6}$	719414	± 6949
800°C	n		1.35	± 0.05
	k	$\text{L}^{1.4}.\text{kg}^{-1}.\text{h}^{-1}.\text{mol}^{-0.4}$	29175	667

The kinetics results become more clear when we consider the physical and chemical changes taking place on the surface of the catalyst through the various stages of the reaction. Hence it is important to review these characterization results before proceeding with discussion of the results.

4.5.3 Catalyst Characterization

4.5.3.1 Catalyst Surface Area

Literature studies (e.g. [26]), suggest that high calcination temperatures would result in pronounced sintering in red mud. Hence, it was crucial to investigate this phenomenon to reveal the temperature at which catalytic cracking could operate without causing a large decrease in surface area. Therefore, the as-received red mud powder was calcined for 3 h in air at temperatures between 300 and 950°C and the surface area was determined by single-point BET. The BET results are depicted in Fig 4.13. It can be seen that a steady decrease in surface area occurred from 300 to 600°C, followed by a more pronounced drop between 600 and 900°C indicating severe thermal sintering effects in the catalyst especially at temperatures > 600°C. Indeed, knowing the melting point of the compound, it is possible to obtain an approximate temperature where sintering effects begin based on general sintering theories. The onset of sintering effects in solids is commonly calculated based on the Tamman and Huttig temperatures of the material [120-123], which are related to the melting point (T_m) according to:

$$T_{Tamman} = 0.5 * T_m \quad E4.24$$

$$T_{Huttig} = 0.3 * T_m \quad E4.25$$

Assuming a melting point of 1250°C for red mud [124] this temperature should approximately be between 375 and 625°C, which visually matches with the experimental results observed.

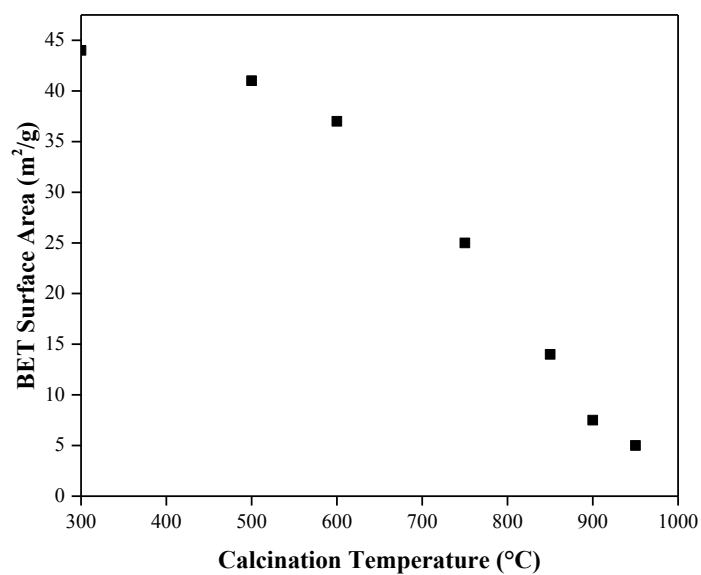


Figure 4.13: Effect of calcination on the surface area of as-received red mud powder determined by single point BET

In order to determine whether the effect of temperature on the surface area would differ with the addition of a binder to the red mud powder and the pelletization of the catalyst, the same tests were repeated for the prepared red mud catalyst pellets, where the particles were calcined for 2 h in air and the effect of temperature on the BET surface area was examined with multipoint BET.

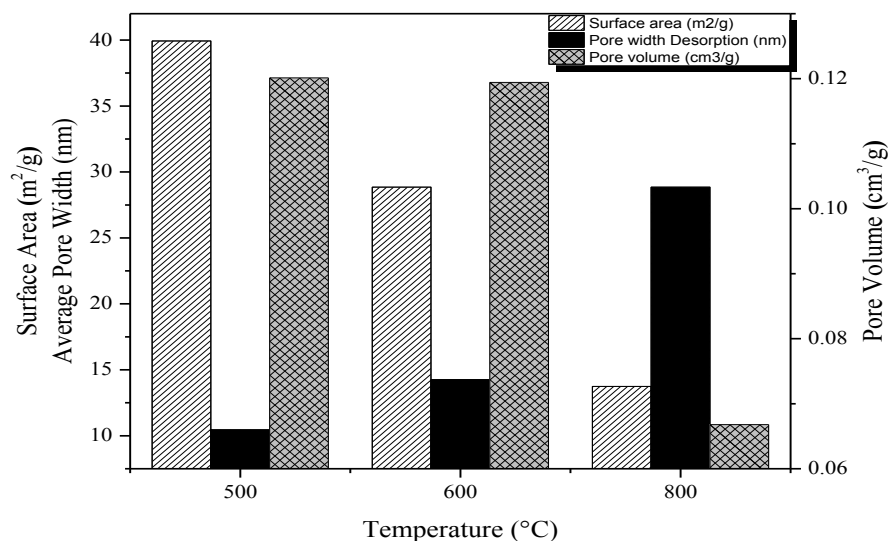


Figure 4.14: Effect of calcination on surface area of pelletized red mud catalyst with multipoint BET

Due to limited resources, the tests could only be performed once. Hence differences that could arise due to batch-to-batch variability or standard errors in the measurement are not reflected in the reported values. Moreover, an important parameter that could be studied in future tests is the effect of calcination time on the surface area, which was not investigated in the current study.

As can be seen in Fig. 4.14, the effect of calcination temperature on the surface area seemed to follow the same trend as before where most of the sintering in the catalyst occurred at temperatures $> 600^{\circ}\text{C}$. The addition of the binder did not appear to have any effect on limiting the sintering of the catalyst. Since most of the surface area of a solid catalyst is normally due to its internal pores rather than the outer surface area, the catalyst

total surface area and pore volume are directly related [125]. This can be seen in Fig. 4.14 where the catalyst pore volume followed the same trend as surface area.

The catalyst average pore size suggests that the catalyst samples tested were mesoporous. The average pore width seemed to increase slightly from 500 to 600°C followed by a drastic increase from 600 to 800°C. This trend could again be due to thermal sintering effects in the catalyst with calcination and, as expected, follows the same trend as the other two parameters discussed.

Figure 4.15 summarizes the evolution of the pore size distribution of the catalyst with temperature. Calcination of the catalyst up to a temperature of 600°C did not appear to result in any observable changes in the pore size distribution of the catalyst. However, calcination at 800°C led to an increase in the average pore size as is evident from the second maximum appearing on the distribution graph. The fact that this maximum occurs at a higher pore size range than for the previous two samples, as well as the drastic decrease of one order of magnitude in the ratio of the pore volume to pore size (tabulated on the y-axis) further highlights the effect of sintering in the catalyst with calcination at temperatures > 600°C.

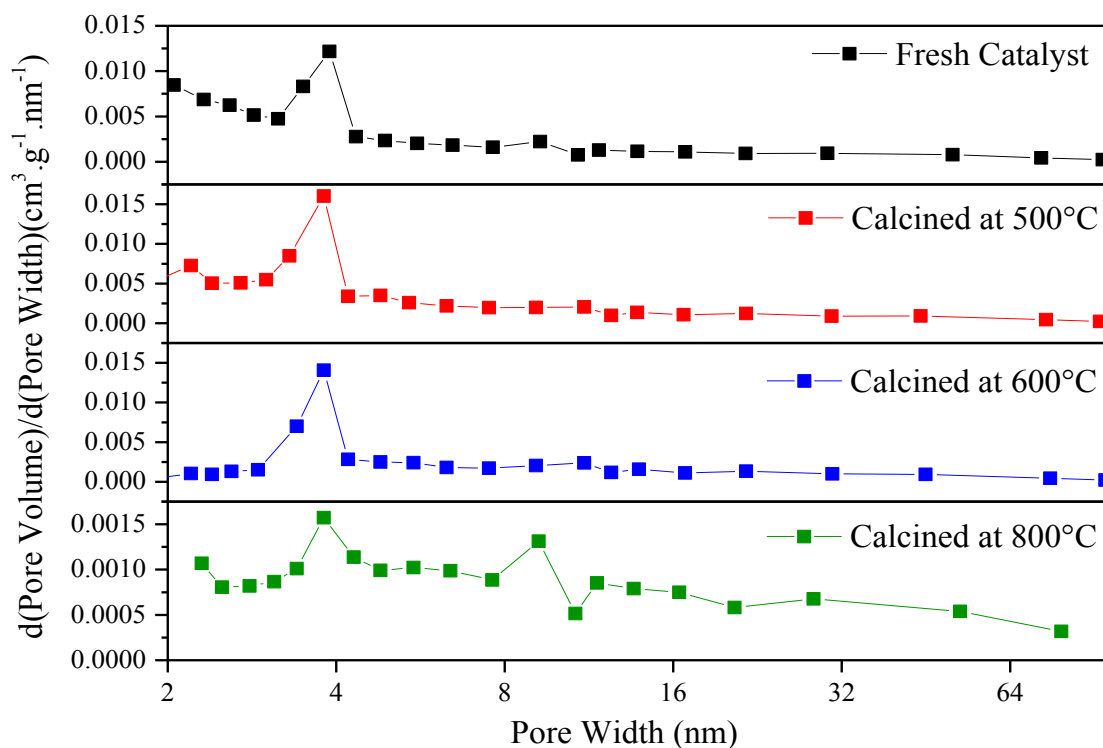


Figure 4.15: Effect of calcination on the pore size distribution of the catalyst

Since the surface area of the catalyst has such an important effect on its performance, it was crucial to determine the amount of surface area reduction after the naphthalene cracking tests to examine the effect of coke formation, which exists in addition to the sintering effects studied previously. Hence, catalyst samples that had been used in the inert catalytic tests at temperatures of 500-800°C and a space velocity of 4500 h⁻¹ were analyzed in the multi-point BET unit to determine their corresponding surface area and pore size distribution (Figs. 4.16 & 4.17).

As can be seen in Fig. 4.16, the degree of surface area reduction was more pronounced at the higher reaction temperatures tested. This is due to the fact that both sintering and coke formation rates are greater at higher temperatures. The surface area remained almost constant between temperatures of 600 and 700°C. Looking at the naphthalene conversion

rates at these two temperatures at a space velocity of 4500 h^{-1} , it can be postulated that the amount of coke formation at both temperatures was probably very similar since the naphthalene conversion measured was close for both of these temperatures (Fig. 4.8). Since the previous study on the effect of calcination was not performed at 700°C , it is very difficult to test this hypothesis as it is not possible to verify whether the level of sintering in the catalyst would remain the same between the temperatures of 600 and 700°C .

In addition to coke formation and sintering, another factor that could be intensifying the loss of surface area in the catalyst is the reaction of naphthalene and the possible by-products of the cracking reaction such as hydrogen on the surface. These reactions could lead to chemical transformations inside the catalyst and could increase the level of sintering. The XRD results of the surface of the catalyst (included in the following section), demonstrate some of these chemical transformations.

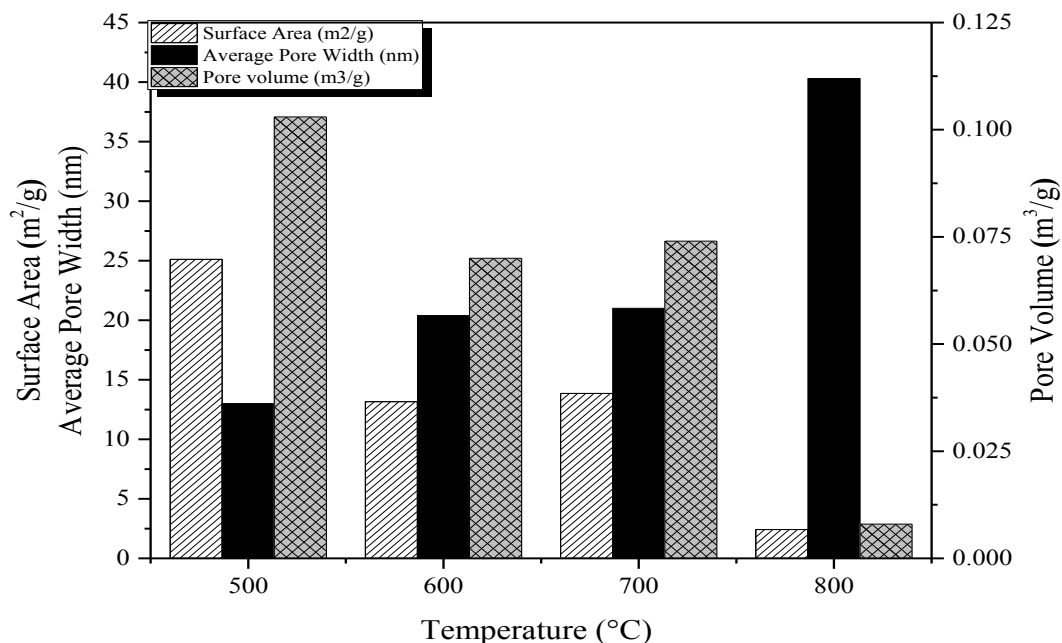


Figure 4.16: Surface area of post reaction pellets tested in an inert environment

Looking closely at Fig. 4.16 again, it can be seen that the pore volume decreased significantly between the temperatures of 500 and 600°C. Since the pore volume was found to remain unchanged between these two temperatures in the previous calcination tests, this sudden loss could be due to the changes in the catalyst surface as a result of the reaction as well as pore blockage due to coke formation. The coke, a product of cracking reactions, deposits on the surface of the catalyst and blocks active sites. The measured pore volume seems to have remained unchanged between 600 and 700°C. This might again be justifiable with the fact that the degree of naphthalene conversion (Fig. 4.8) was found to be nearly the same. However, a drastic decrease can be observed at the reaction temperature of 800°C, where possibly the majority of the coke formation and deposition as well as chemical transformation of the surface of the catalyst take place.

These results are reflected accordingly in the measured values of the average pore size. In order to determine the pore size region, which seemed to be more active in catalytic cracking reactions, the BJH pore size distribution of the tested samples were superimposed in Figure 4.17. As can be seen, the majority of the pores were in the range of 30-40 Å. However, as the reaction temperature increased to 600°C the majority of the pores seem to have been blocked/sintered until they were completely vanished at 800°C. Comparing this to the pore distribution graph obtained previously, Figure 4.15, where the pore size distribution remained almost unchanged up to a temperature of 600°C, one could arrive at the conclusion that the majority of the pore blockage observed in Figure 4.17 was due to the reaction itself. Moreover, it seems reasonable to conclude that the smaller pores (20-50 Å) were more active in the cracking reaction.

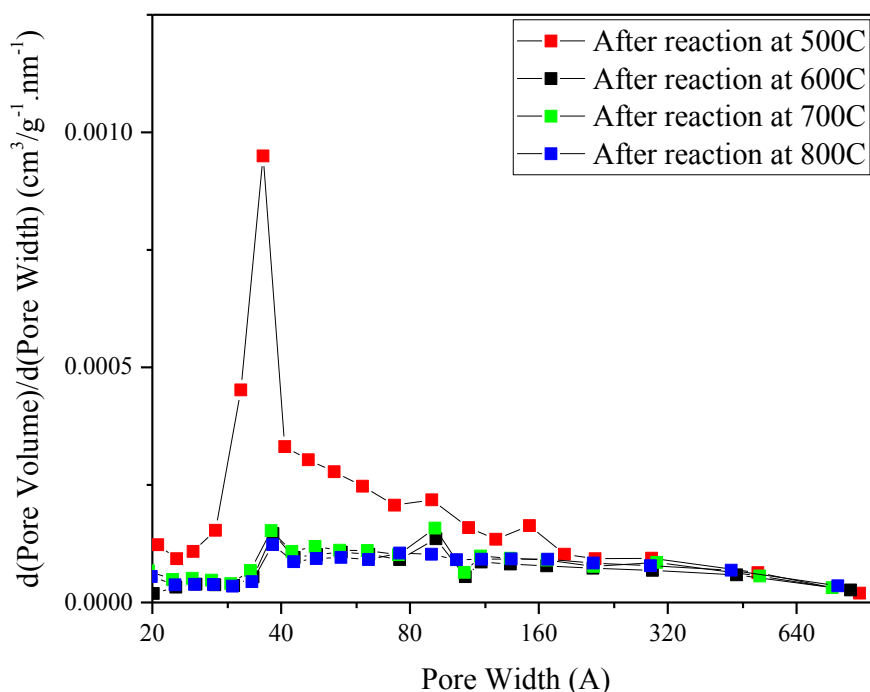


Figure 4.17: BJH pore width distribution of fresh red mud catalyst compared with spent catalyst after reaction at temperatures of 500 to 800°C

It is generally accepted that physical properties of catalysts such as surface area and pore structure play an important role in the activity of the catalysts; however, chemical properties such as crystalline phase and oxidation states of the active sites could have much greater influence than their physical properties [88]. This is further examined in Section 4.5.3.3.

4.5.3.2 Structural Analysis

The microscopic structure and qualitative physical changes of the red mud due to calcination, pelletization as well as catalytic tar cracking was analyzed using a Hitachi S3000N scanning electron microscope (SEM).

Figures 4.18 and 4.19 show the as-received red mud and the prepared red mud catalyst, respectively. No significant difference can be seen between the two materials. Even though the prepared red mud catalyst seems to be slightly smoother than the raw material, no obvious agglomeration was observed. The smoother structures are most probably due to the pre-treatment at 350°C (Section 3.1). Both materials have a high porosity with a hole diameter ranging between 0.5 and 2 μm . Figures 4.20 and 4.21 show red mud catalyst used for naphthalene conversion over 5 h at 850°C and a space velocity of 19000 h^{-1} . The surface of the used catalyst appears significantly smoother than the raw material. This change in structure is probably by agglomeration due to exposure to 850°C in addition to coke deposition in pores. These structural changes are in line with the findings of Wang et al. [126], who reported the formation of larger grains in a mixture catalyst of Ni, Fe_2O_3 and dolomite. They reported the disappearance of porosity after calcination at 1100°C.

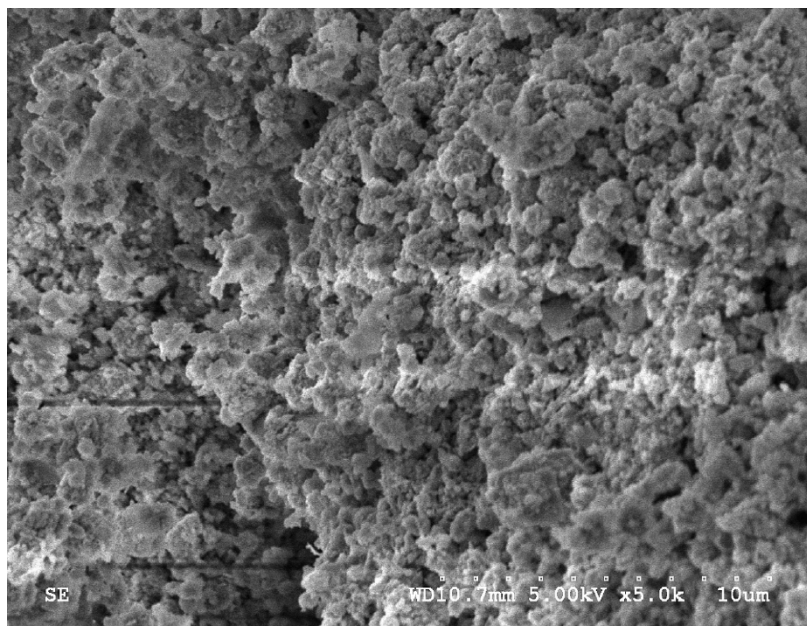


Figure 4.18: SEM image of the as-received red mud powder

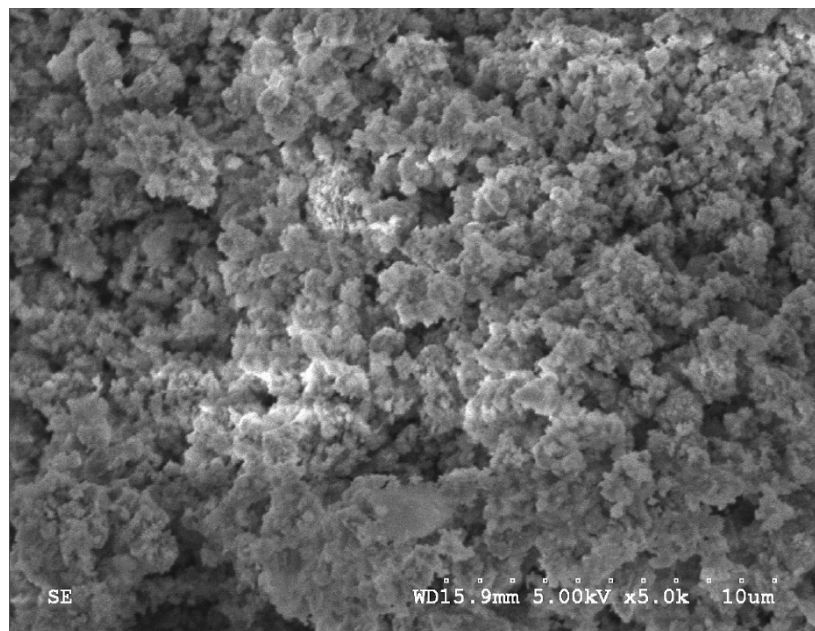


Figure 4.19: SEM image of the prepared red mud pellet prior to any reaction

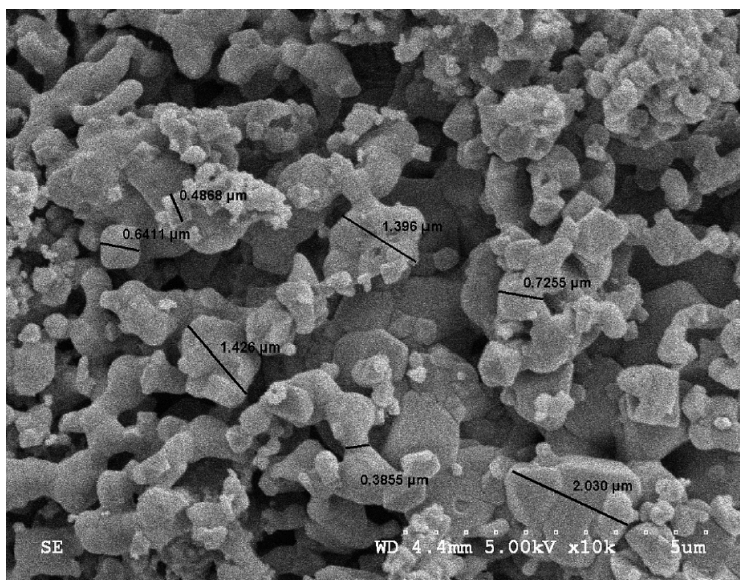


Figure 4.20: SEM image of the red mud pellet after reaction at 850°C

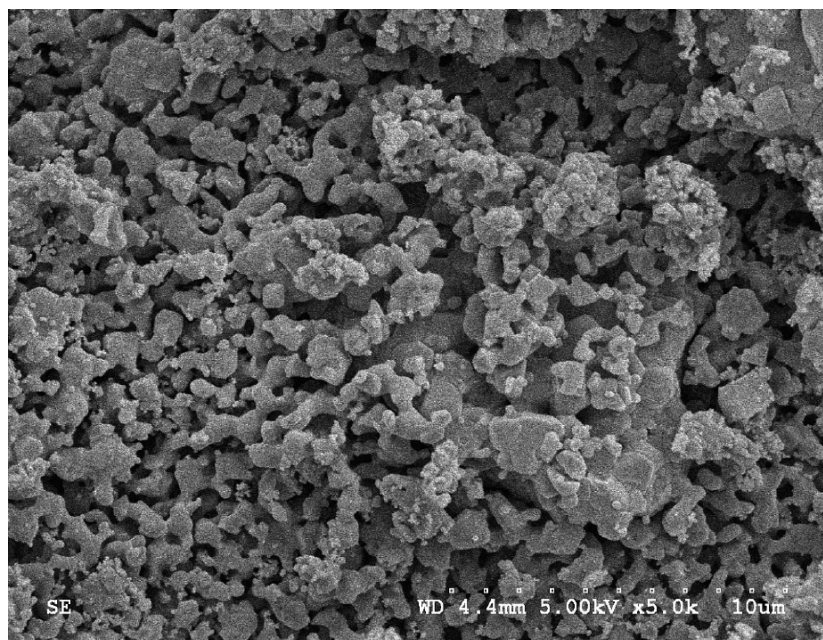


Figure 4.21: SEM image of the red mud pellet after reaction at 850°C

4.5.3.3 Catalyst Chemical Composition

Powder x-ray diffraction (XRD) in conjunction with thermogravimetric analysis (TGA) were used to provide information about the nature of the constituent crystalline phases of the catalyst, as well as to track the evolution of the phases after exposure to naphthalene at high temperatures. Experiments were conducted on both the synthesized red mud pellets and the spent catalyst at various temperatures. Nordgren et al. [19] investigated the catalytic activity of iron-based granules as a tar cracking catalyst in biomass gasification and found that catalysts in their metallic states exhibit a better tar cracking capacity compared with their corresponding oxide phases. The extent to which each phase (metallic or oxide) is present on the catalyst surface is very important. However, it was not in the scope of this project to provide detailed quantitative characterization of the

phases present. Further investigation including thorough quantification and characterization of the catalyst surface would therefore be of great interest.

The XRD pattern of all samples discussed in this section can be found in Appendix E. Table 4.2 summarizes the mineralogical phases identified in the as-received red mud powder compared to those identified in a sample of a red mud pellet prepared according to the pelletization method described previously in Section 3.1. As can be seen, the addition of the binder and acid treatment of the catalyst did not result in any discernible changes in the crystalline phases of the catalyst.

Table 4.2: Crystalline phases identified by powder XRD in the as received RM sample at 25°C (left) vs. fresh unspent pelletized RM (right)

As-received	Pellet
Hematite	Hematite
Antase	Antase
Quartz	Quartz
Goethite	Goethite
Calcite	Calcite
Gibbsite	Gibbsite
Titanite	Titanite
Boehmite	Boehmite
NaAlSiO ₃ C(OH)	NaAlSiO ₃ C(OH)

Figure 4.22 depicts the total weight loss of the synthesized red mud pellets in the temperature range of 24-1000°C (~7.6%), found through TGA under N₂ flow at a heating rate of 10°C/min. As shown, the mass loss region can be divided into three sections. In order to determine the exact mineralogical phases in the catalyst as well as the reactions that take place in each section, the same TGA analysis was repeated three times: up to a temperature of 350°C, 550°C and finally to 1000°C. Powder XRD was then performed on each of the catalyst samples retrieved after being tested with TGA to determine the nature of the species formed/decomposed at each stage.

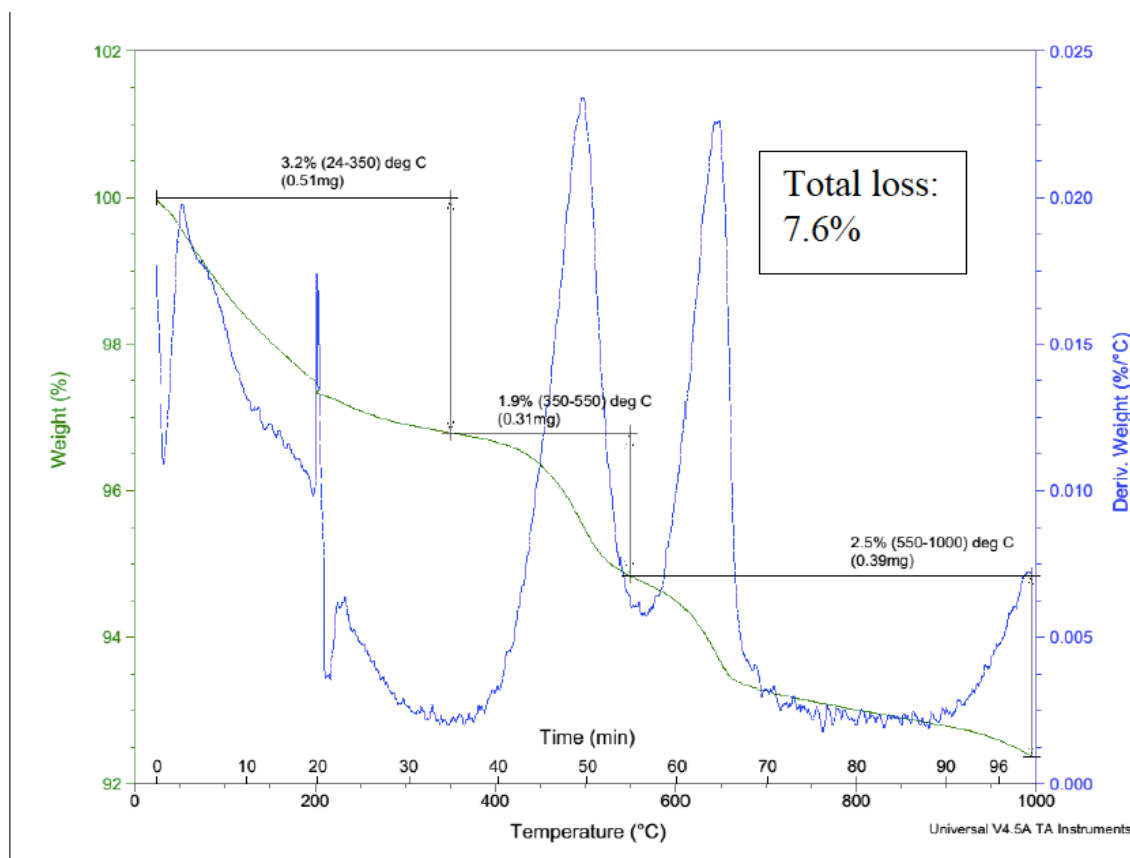


Figure 4.22: Thermogravimetric analysis of unspent red mud pellet with nitrogen

The first mass loss step of the sample (3.2%) observed in the range of 24-350°C could be attributed to three separate processes occurring within this temperature range: evaporation of the free water which occurs within the range of 24-150°C [8-10], decomposition of goethite to hematite (R4.1)[95, 110, 114, 127] and dehydroxylation of gibbsite to boehmite at 150-350°C (R4.2)[91, 95, 108, 110, 113, 114, 127-129]. XRD analysis of the post-TGA sample further confirmed these postulates, since goethite and gibbsite peaks could not be identified in the XRD profile after the TGA analysis (Table 4.3).

i. Transformation of Goethite into Hematite:



ii. Dehydroxylation of Gibbsite into Boehmite:



Another possibility is the dehydroxylation of gibbsite into anhydrous alumina (R4.3) [91, 95, 110]. However, this could not be confirmed since no corresponding peaks could be identified for anhydrous alumina in the powder XRD pattern. This could be either due to the alumina phase contributing towards the formation of Sodium Aluminum Silicate Carbonate Hydrate, or alternatively, transforming to the amorphous phase.



Table 4.3: Crystalline phases identified by powder XRD at 25°C (left) vs. at 350°C (right) after exposing fresh unspent catalyst to different temperatures in a N₂ environment

25°C	350°C
Hematite	Hematite
Antase	Antase
Quartz	Quartz
Goethite	-
Calcite	Calcite
Gibbsite	-
Titanite	Rutile
Boehmite	Boehmite
NaAlSiO ₃ C(OH)	NaAlSiO ₃ C(OH)

The second mass loss step (1.9%) observed in the range 350-550°C could be due to the evaporation of interstitial water, which exhibits red mud's good water-retention

properties [130]. XRD analysis of the sample after TGA indicated the disappearance of the boehmite phase which had been formed in the previous step. All other phases, however, remained intact. Hence the decomposition of boehmite could be another possible route causing mass loss in this stage. From the literature, two possible reactions could be responsible:

i. Dehydration of boehmite into anhydrous alumina [91, 95, 110, 127, 128] according to:



Since no traces of anhydrous alumina were identified in the XRD profile, this reaction could not be confirmed, given that there is the possibility of the product being in the amorphous phase.

ii. Complete conversion of Boehmite to Sodium Aluminum Silicate Carbonate Hydrate, which was identified in the XRD patterns.

Table 4.4: Crystalline phases identified with powder XRD at 350°C (left) and 550°C (right) after exposing fresh unspent catalyst to different temperatures in N₂ environment

Calcined at 350°C	Calcined at 550°C
Hematite	Hematite
Antase	Antase
Quartz	Quartz
Calcite	Calcite
Rutile	Rutile
NaAlSiO ₃ C(OH)	NaAlSiO ₃ C(OH)
Boehmite	-

The third mass loss region (2.5%) was observed within the range of 550-1000°C. Considering the phases identified in the XRD profile at 1000°C, the mass loss could be

attributed to the evaporation of the structural water existing in the hydrate salts and at higher temperatures to the decomposition of calcite to calcium oxide and CO₂ (R4.5) [95, 108, 112-114, 127, 128, 131-133]. Another possibility is the reaction of calcium oxide with titanium and silicon oxides according to reaction scheme 6 [95, 110].



Above 800°C Sodium Aluminium Silicate Carbonate Hydrate could decompose into Nepheline [114, 133, 134]. Another change that can be expected is the transformation of quartz to its polymorph beta-cristobalite [110, 114].



Table 4.5: Crystalline phases identified by XRD at 550°C (left) and 1000°C (right) after exposing fresh unspent catalyst to temperature in a N₂ environment

Calcined at 550°C	Calcined at 1000°C
Hematite	Hematite
Antase	Goethite
Quartz	Nepheline
Calcite	Titanite
Rutile	Cristobalite, beta
NaAlSiO ₃ C(OH)	NaAlSiO ₃ C(OH)

Figure 4.23 depicts the result obtained for TGA analysis of the as received red mud samples under N₂. As can be seen the total mass loss observed was about 11.1%. The higher amount of mass loss in this case compared with the synthesized catalyst pellet (Fig 4.22) is due to the fact that the particles are heated to 350°C as part of the pellet preparation procedure which consequently would remove a large portion of the water

content that could perhaps still exist in the as received powder.

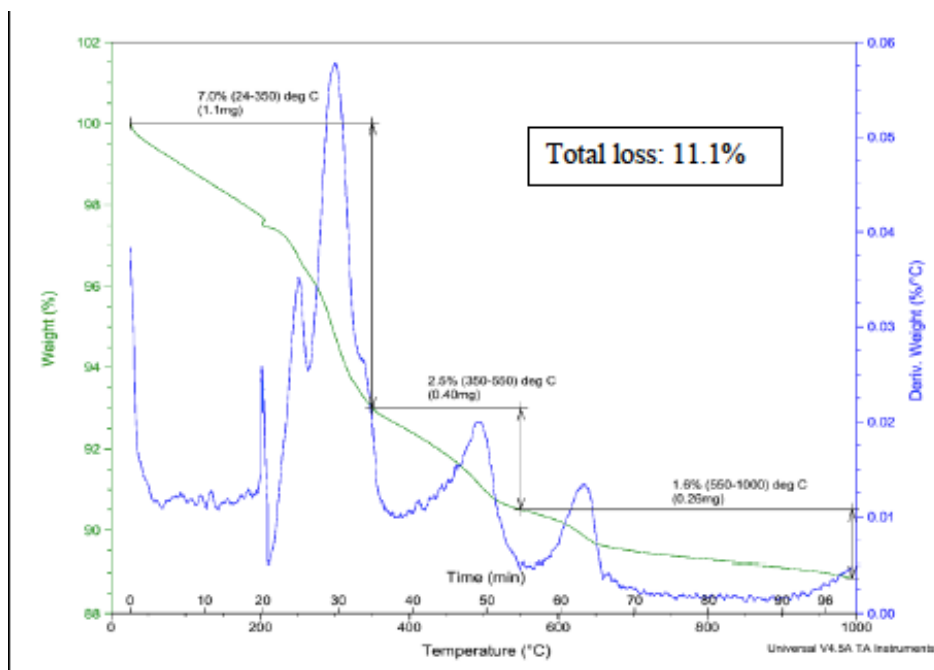


Figure 4.23: Thermogravimetric analysis of as received red mud powder prior to any processing with nitrogen

Figure 4.24 shows the TGA curve of spent red mud catalyst which had previously been reacted with naphthalene at a temperature of 800°C. As can be seen, the sample exhibited a total mass loss of 3.43%. Since all samples were stored in air-tight, sealed glass vials at room temperature after the reaction, the probability of moisture adsorption on the catalyst surface is low. One possibility contributing to the observed mass loss could be the reaction of the carbon atoms deposited on the surface of the catalyst with oxygen containing species of the catalyst to form CO₂ [135]. This could be confirmed in future tests by analyzing the outlet gas composition of the gas exiting the TGA device.

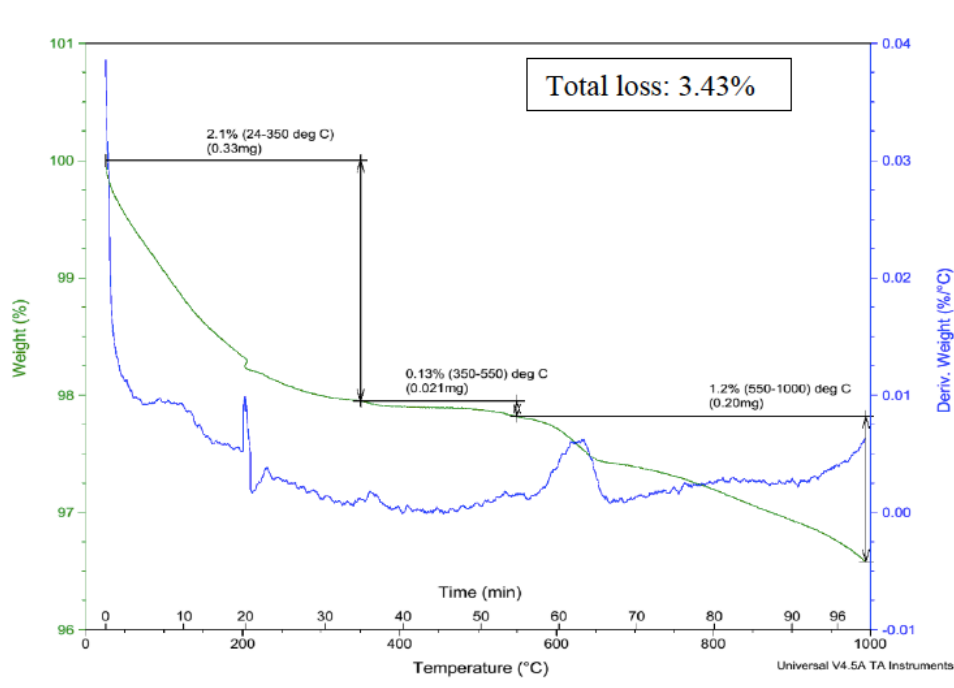


Figure 4.24: Thermogravimetric analysis (under N₂) of spent red mud pellet after exposure to a reactor temperature of 800°C

Comparing the crystalline phases identified in the unspent catalyst exposed to 1000°C with spent catalyst pellets after 1 and 14 h of reaction leads to some interesting conclusions, specifically with regards to the iron and iron oxide phases present in the samples. As can be seen in Table 4.6, with the unspent catalyst the only phases of iron present were hematite and goethite, even after exposure to a temperature of 1000°C. However, these phases were transformed to magnetite, wustite and metallic iron once exposed to naphthalene at 800°C for a duration of one hour. When the catalyst was exposed to the reactant for a longer period, i.e., for 14 h, the only remaining iron phases were metallic iron and ilmenite.

These phenomena may be explained by the following reaction scheme. As the cracking reaction of naphthalene takes place, hydrogen and coke as well as lighter hydrocarbons

are formed in the reactor. Hematite could both react with the released hydrogen according to R4.8 to form magnetite and water, or be reduced by the coke generated to metallic iron [136]. This is in line with visual observations during the experiment. A significant amount of water was found to have formed during the reaction, on multiple occasions leading to blockages in the naphthalene collection bottle once the water entered the colder temperature ice bath and solidified. Moreover, it has been shown in the literature [137-139] that the temperature of the iron oxide reduction reaction (R4.9) could be lowered to 800-900°C in the presence of highly reactive coke. As the reaction proceeds, magnetite could also react with coke and be reduced to wustite and CO (R4.11). This is in line with the findings of Cahyono et al. [140] who also reported the reduction of their starting material, iron ore, to FeO as a result of tar decomposition at a temperature of 800°C.

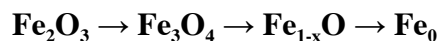
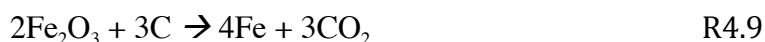


Table 4.6: Crystalline phases identified with powder XRD in fresh unspent catalyst pellet heated at 1000°C in N₂ atmosphere (left) compared with spent catalyst pellets after 1 hour of reaction (middle) and 14 h of reaction (right)

1000°C	Post Reaction (1h)	Post reaction (14h)
Hematite	Magnetite	Iron
Goethite	Iron	Ilmenite
Nepheline	Wustite	Nepheline
Titanite	Perovskite	Perovskite
Cristobalite, beta	Nepheline	

4.5.4 Discussion

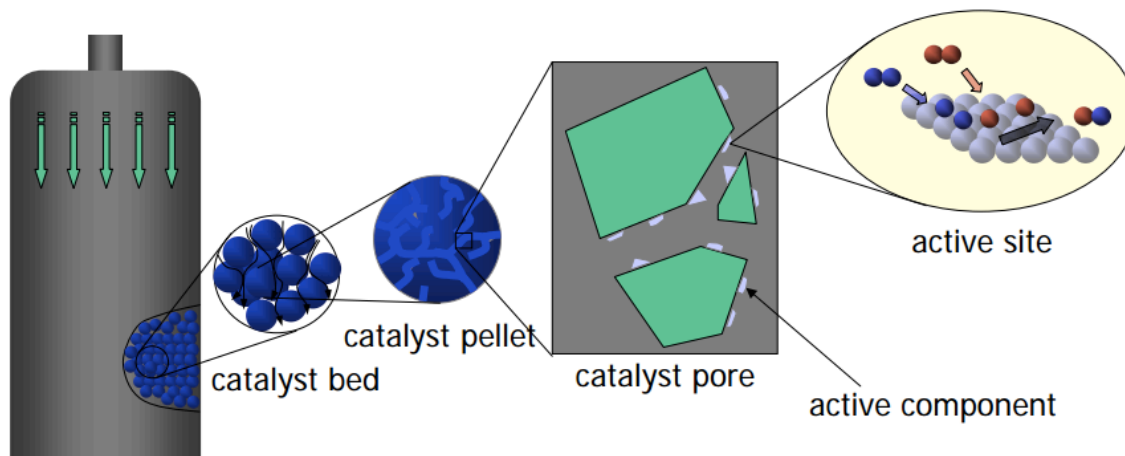


Figure 4.25: The complexity of heterogeneous catalysis [141]

As can be seen in Fig. 4.25, heterogeneous catalysis is a complex process involving not only the chemical reaction but also material transport at all scales and includes many steps that ultimately affect the overall kinetics of the process [141]. These include:

Transport of material from the bulk to the surface of the catalyst	→ External diffusion
Diffusion of reactant from the surface of the catalyst through the internal pore	→ Internal diffusion
Adsorption of the reactant on the active site(s)	} → Surface reaction
Chemical reaction	
Desorption of product(s) from the active site(s)	} → Internal diffusion
Diffusion of the products out through the internal pores	
Bulk diffusion of the products out of the system	→ External diffusion

What is evident from the catalyst characterization results is the physical and chemical evolution of the catalyst pellets as a result of being exposed to different temperatures and reactive media. As could be seen from the powder XRD results, the nature of the phases of iron present in the catalyst was a direct function of the temperature it was exposed to in addition to the reaction time. Hence it may not be unreasonable to imagine that the pathway that the reaction takes place at each temperature tested could differ from the other as a result of these differences in the chemical structure of the catalyst. This is directly reflected in the apparent reaction orders found from the experimental data (Figs. 4.9-4.12 & Table 4.1). It can be seen that the reaction order (n) changed from 1 to 1.42, 1.63 and ultimately to 1.35 for reactor temperatures of 500°C to 800°C.

Moreover, as the catalyst is exposed to different temperatures, the degree of pore volume and surface area loss is also varied. These changes are functions of the degree of sintering, as well as fouling due to carbon deposition that takes place during the reaction as reflected in the BET surface measurement data previously reported (Figs. 4.14 & 4.16). As a result, there would be significant differences in the internal mass transfer resistances through the catalyst pores at each reaction condition tested. Hence, looking back at Fig. 4.25, the catalyst would be going through various changes: from changes in the nature of the active sites due to chemical transformation of the iron component, to changes in the internal pores of the catalyst as a result of sintering and fouling, to finally overall changes in the catalyst pellet that result in deactivation and decay over reaction time.

The other interesting observation from the kinetics data is the fractional (non-integer) nature of the apparent reaction order at temperatures of 600, 700 and 800°C. This effect could be indicative of two points:

- The reaction is not elementary and involves a complex reaction network involving various intermediate and final products in the process. Since the nature of the reaction products could not be identified with the resources available, and determining the mechanism of the reactions taking place was not part of the project objectives, this point has not been explored further.
- Considering the Langmuir-Hinshelwood equation for surface reactions:

$$-r_A = \frac{k_A \cdot C_A^n}{\sum_i^n (k_i \cdot C_i)} \quad (\text{E24})$$

the non-integer nature of the reaction order could indicate that the denominator of the Langmuir-Hinshelwood equation is becoming dominant, i.e., the occupation of the active sites by the adsorbed reactant as well as adsorbed products cannot be neglected and is manifested in the apparent reaction rate measured.

Moreover, the effect of temperature on coke generation was very striking (Fig. 4.26); however, as mentioned previously, the deactivation mechanisms and kinetics were beyond the scope of the current study.

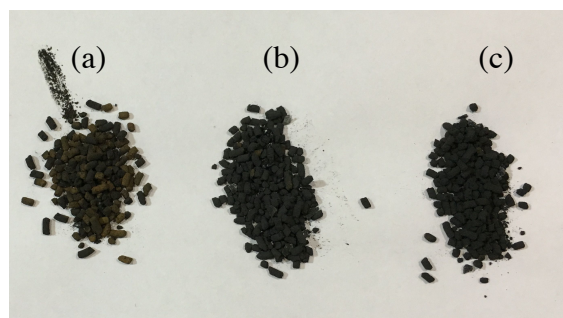


Figure 4.26: Carbonaceous deposits on the surface of the catalyst at (a) 600°, (b) 700°C, (c) 800°C

4.6 Tests with H₂

4.6.1 Catalytic Activity and Kinetic Results

Figure 4.27 summarizes the findings from the naphthalene conversion experiments in the presence of 13 vol.% H₂ with balance N₂, conducted at four temperatures and four space velocities. As with previous tests with N₂, hydrogen tests exhibited a similar trend where increasing the space velocity and the temperature both had a significant effect on improving the tar removal efficiency. Figures 4.28-4.31 compare the naphthalene removal efficiency of the catalyst in the presence and absence of H₂ at each of the space velocities tested.

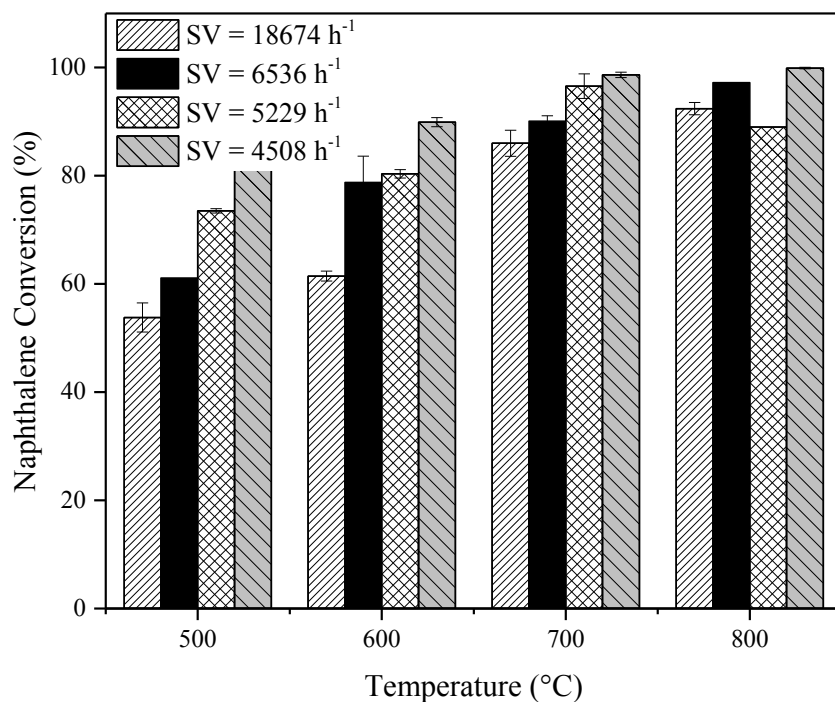


Figure 4.27: Results of naphthalene cracking tests performed at temperatures of 500-800°C at space velocities of 4508-18674 h⁻¹ with 13 vol.% H₂ in balance N₂

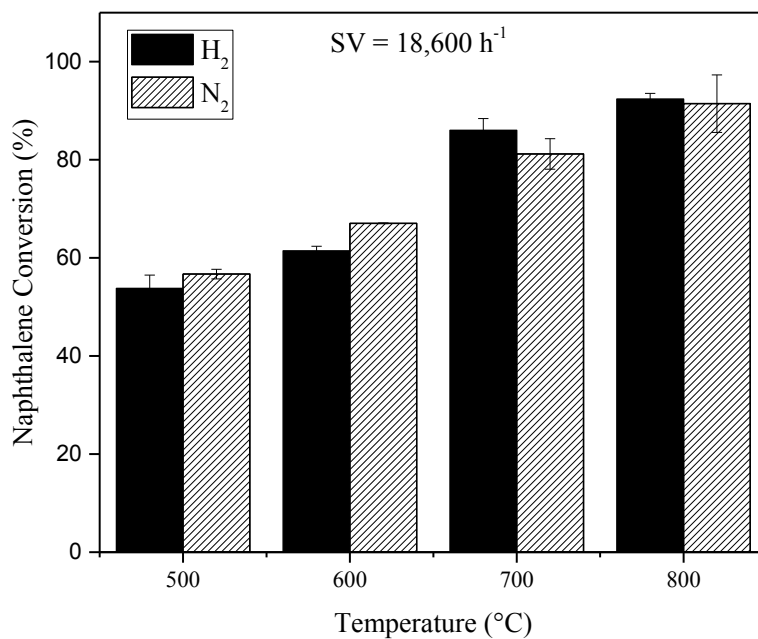


Figure 4.28: Results of naphthalene cracking test with 13 vol.% H₂ at a space velocity of 18,600 h⁻¹

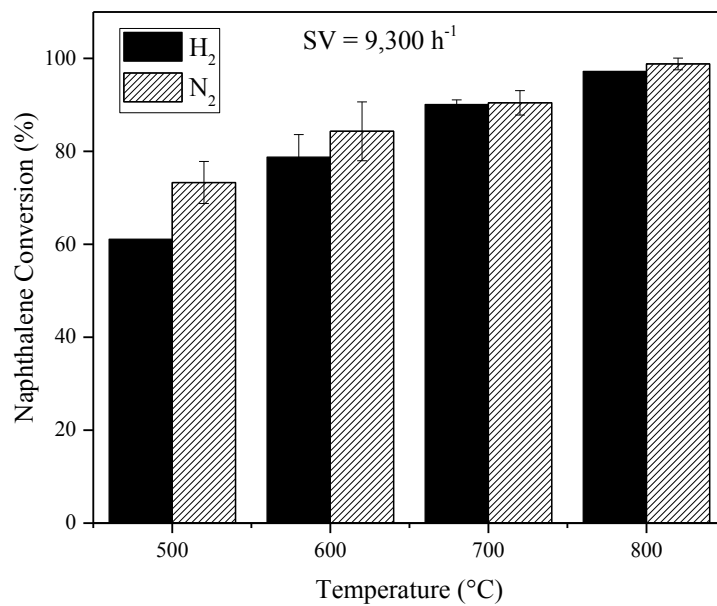


Figure 4.29: Results of naphthalene cracking test with 13 vol.% H₂ in balance N₂ at SV = 9,300 h⁻¹

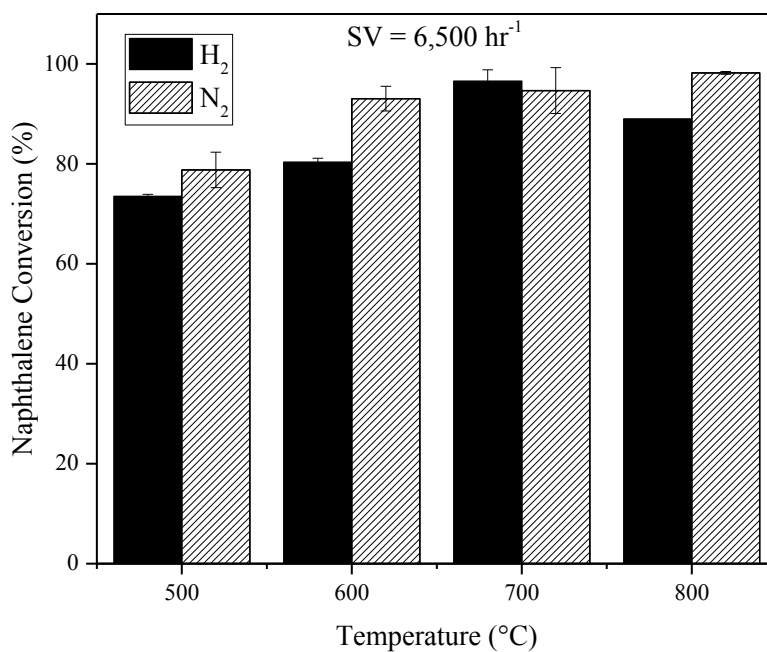


Figure 4.30: Results of naphthalene cracking test with 13 vol.% H₂ at SV = 6500 h⁻¹

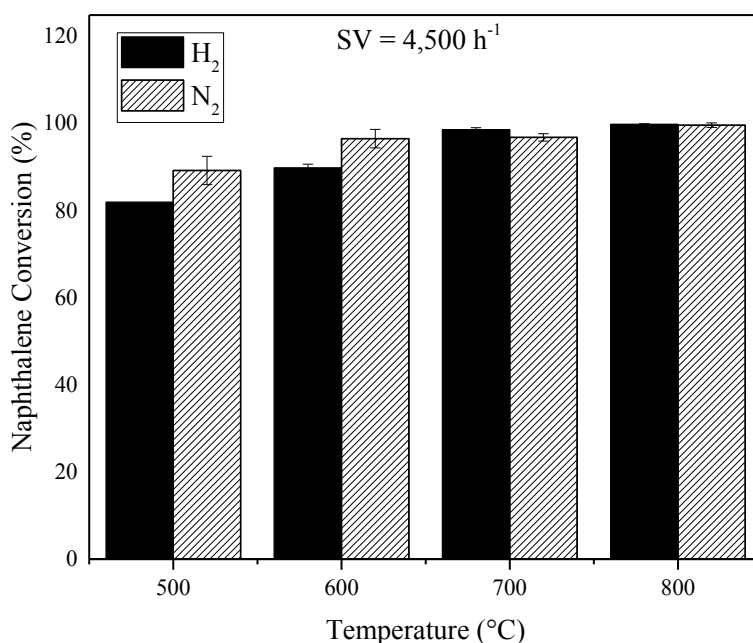
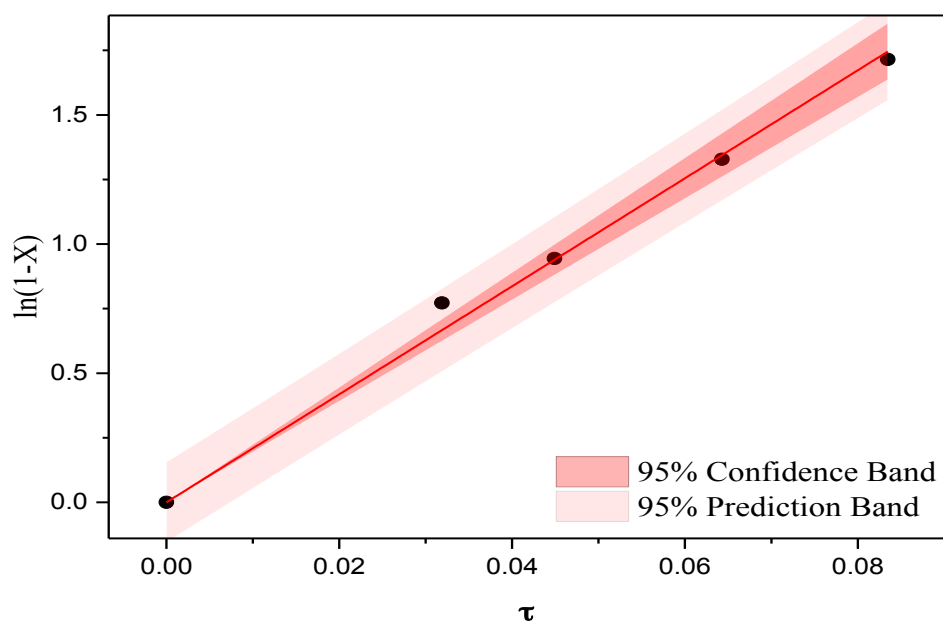


Figure 4.31: Results of naphthalene cracking test with 13 vol.% H₂ in balance N₂ at SV=4,500 h⁻¹

As with the nitrogen tests, a similar attempt was made to determine the kinetic parameters of the reaction with H₂, the results of which are summarized in Figures 4.32-4.35. As can be seen, the reaction was found to be 1st order for all the temperatures tested in the presence of H₂, with the slope of each plot representing the reaction rate constant (*k*) (Table 4.7). Since the order of the reaction remained the same (1st order) in all the tests, the Levenberg-Marquardt algorithm was used to fit the reaction rate constants found in the Arrhenius equation using commercial software OriginLab®.

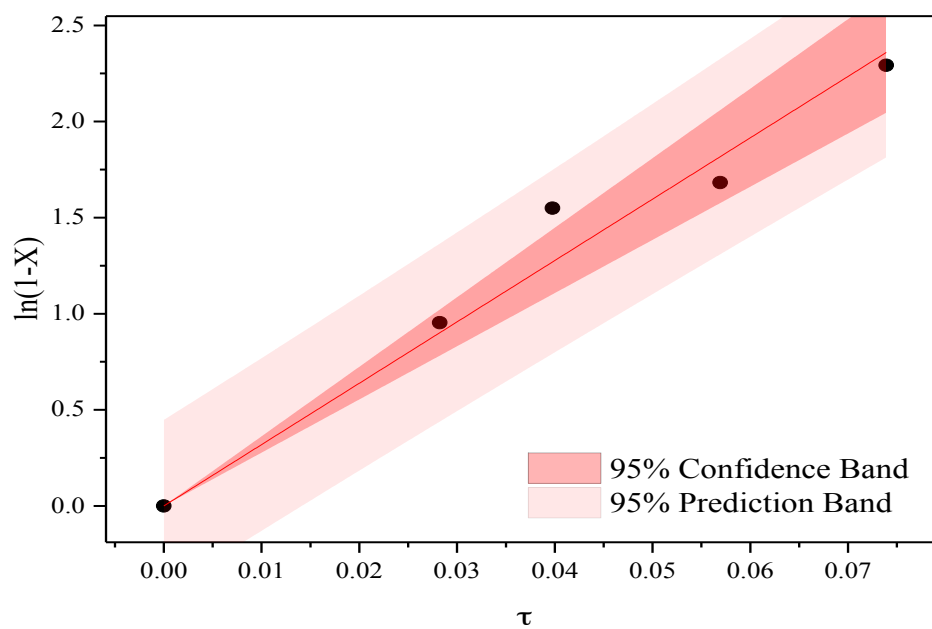
$$k = Ae^{-\frac{E_A}{RT}} \quad \text{E4.24}$$

Hence, the apparent activation energy of the reaction (in 13% H₂) was found to be 37.3 ± 4.0 kJ/mol (Fig. 4.36).



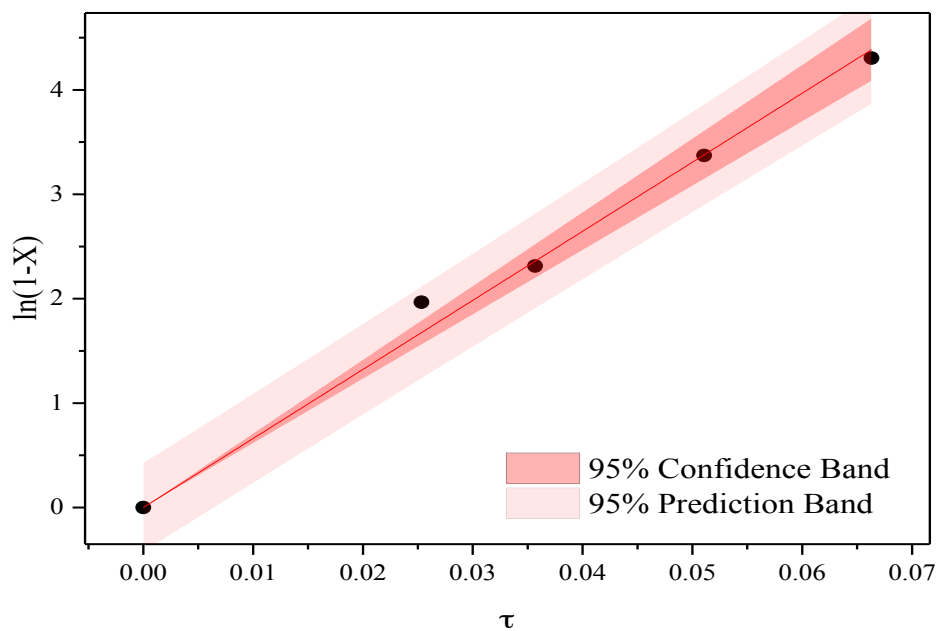
Intercept Value	Slope Value	Slope Standard Error	Statistics R-Square
0	20.91	0.47	0.998

Figure 4.32: Results of the kinetic analysis for test with 13 vol.% H₂ test at 500°C



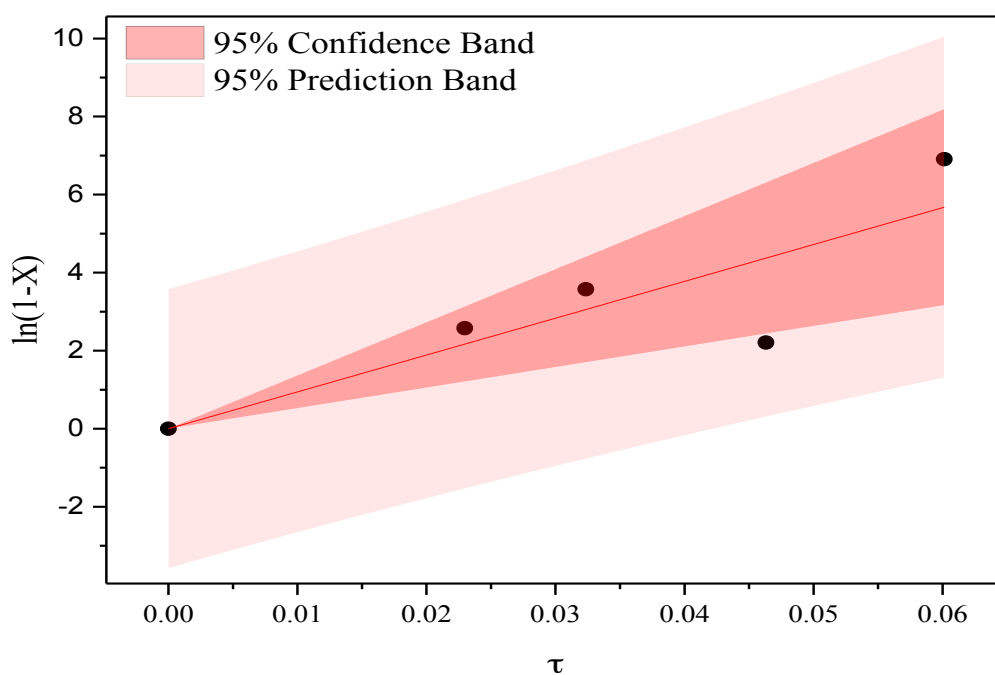
Intercept Value	Slope Value	Slope Standard Error	Statistics R-Square
0	31.92	1.53	0.989

Figure 4.33: Results of the kinetic analysis for experiment with 13 vol.% H₂ test at 600°C



Intercept Value	Slope Value	Slope Standard Error	Statistics R-Square
0	66.14	1.62	0.997

Figure 4.34: Results of the kinetic analysis for experiment with 13 vol.% H₂ test at 700°C



Intercept Value	Slope Value	Slope Standard Error	Statistics R-Square
0	94.41	15.04	0.885

Figure 4.35: Results of the kinetic analysis for experiment with 13 vol.% H₂ test at 800°C

Table 4.7: Kinetic rate constant of naphthalene cracking with red mud in presence of 13 vol.% H₂ at the reaction temperatures tested

Temperature (°C)	k (m ³ .kg ⁻¹ .h ⁻¹)	Standard error
500	20.91	0.47
600	31.92	1.53
700	66.14	1.62
800	94.41	15.04

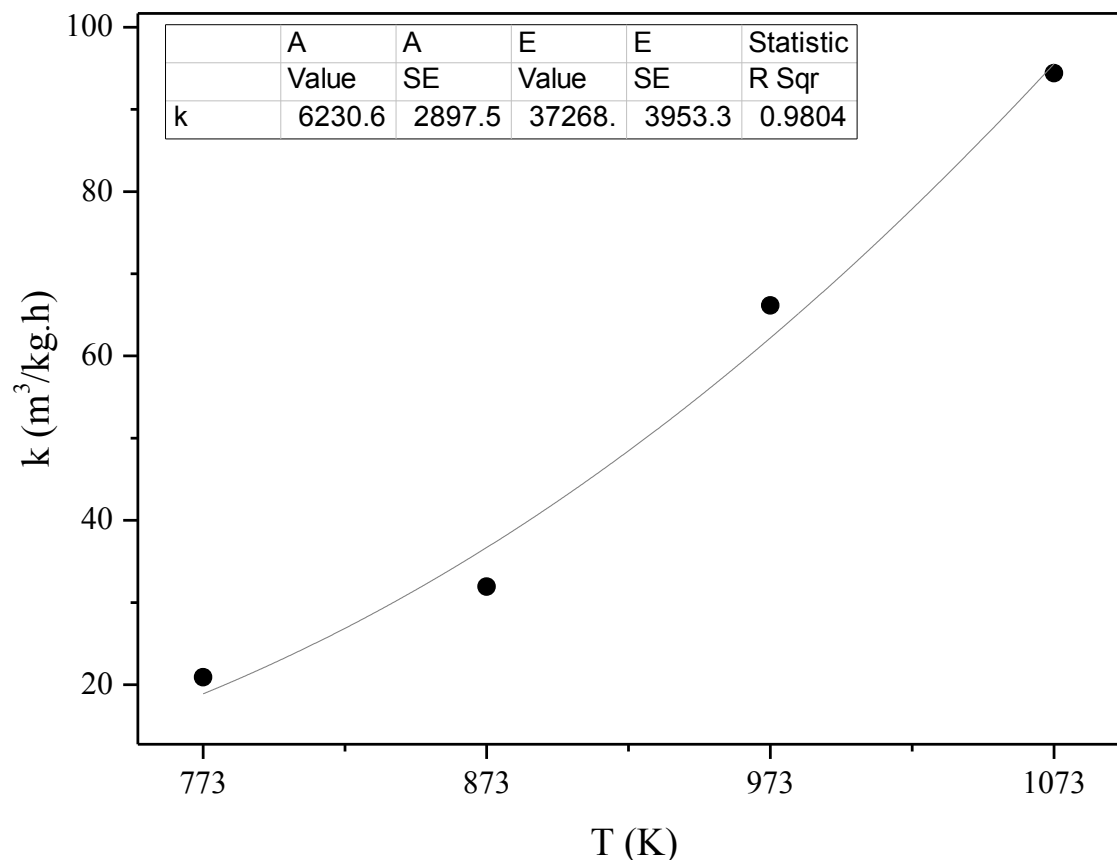


Figure 4.36: Activation energy for naphthalene cracking on red mud with 13 vol.% H₂ in balance N₂

As in the previous section, it is essential to review the results of the catalyst characterization tests in order to better understand the kinetics results.

4.6.2 Catalyst Characterization

4.6.2.1 Catalyst Surface Area

In addition to the effects of sintering discussed previously, the introduction of H₂ to the system and the consequent reduction of the catalyst particles would have a direct effect on the catalyst physical properties such as its surface area and pore size. In order to

investigate this effect, the prepared catalyst pellets were reduced in 13 vol.% H₂ in N₂ for 2 h and then analyzed with multi-point BET for surface characterization.

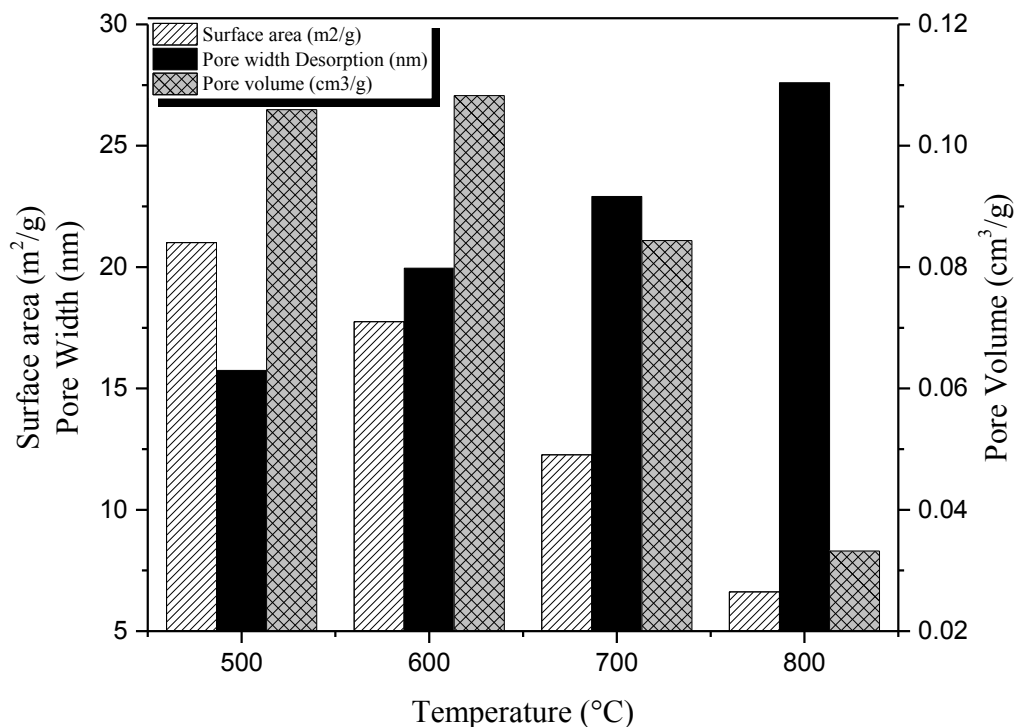


Figure 4.37: Multi-point BET surface area of reduced red mud pellet

As can be seen in Figure 4.37, the reduction of the catalyst pellets had a drastic impact on their surface area, as well as pore volume and pore size even at the lowest temperature tested (500°C). The surface area was measured to be 20.0, 17.8, 12.3 and 6.6 m²/g at temperatures of 500, 600, 700 and 800°C, respectively, showing a drastic reduction compared to the original catalyst surface area of 38.1 m²/g. Moreover, comparing these values to the results from Figure 4.14, where the effect of calcination temperature was examined, it can be immediately noticed that the surface area measured was almost halved by the addition of hydrogen at each of the temperatures tested. This is similar to

the findings of Costa et al. [115] who also studied the effect of reduction with H₂ on the surface area of red mud, and observed an increase in the degree of surface area reduction in their catalyst with increasing temperature. The authors attributed this decrease to the reduction of the iron oxide, “the breakdown of Al-hydroxides and sodalite-type minerals”, as well as sintering, all of which are pronounced with temperature. Bukur et al. [142] studied the same phenomena on an iron-based Fischer-Tropsch (FT) catalyst and observed minimal decrease in catalyst surface area at a calcination temperature of 300°C. However, when the same catalyst was reduced with H₂ at 280°C, the surface area was found to have been reduced from the initial value of 295 to 136 m²/g, i.e., more than 50% lower than the original surface area due to the collapse of the Fe₂O₃/FeOOH network. Bian et al. [142] also found a decrease in their FT iron catalyst surface area, in their case from 38 to 7 m²/g after reduction with H₂ at 300°C.

It should be emphasized that an important factor that could have an impact on the degree of surface sintering, and consequently the surface area of the catalyst could be the rate of temperature increase in the system, which was not investigated in the current study. Decreasing the temperature ramping rate of the reactor should be studied in the future as a possible way of minimizing the surface area losses in the catalyst.

4.6.2.2 Catalyst Chemical Composition

In order to determine the nature of the crystalline phases in the catalyst after reduction with H₂, powder XRD technique was again used on samples reduced at 500 and 800°C (Table 4.8). It can be seen that the entire iron phase of the catalyst was reduced to metallic iron, in spite of the high degree of sintering and surface area reduction that occurred in the catalyst at these temperatures, especially at 800°C. In contrast, Bian et al. [143] found that not all of the iron oxide phase of their catalyst was reduced to metallic iron. This was due to the quick sintering of their catalyst in the presence of H₂, which inhibited the internal iron oxide-containing particles from reduction. In their case, this was resolved by reducing the temperature ramping rate to 0.2°C/min.

Table 4.8: Crystalline phases of RM by Powder XRD after reduction with 13 vol.% H₂

Calcined at 1000°C	Reduced at 500°C	Reduced at 800°C
Hematite	Iron	Iron
Goethite	Anatase	Nepheline
Nepheline	Rutile	Perovskite
Titanite	Calcite	
Cristobalite, beta	Quartz	
NaAlSiO ₃ C(OH)	NaAlSiO ₃ C(OH)	
	Nepheline	

Table 4.9: Crystalline phases of RM as determined by Powder XRD after reaction with naphthalene in the presence of 13 vol.% H₂

1h Reaction with H ₂	14h Reaction with H ₂
Iron	Iron
Nepheline	Nepheline
Titanium oxide	Aluminum oxide
Aluminum oxide	Titanium oxide
	Rutile

4.6.3 Discussion

Returning to our original discussion of the catalytic activity and looking at Figs. 4.28-4.31, it can be seen that at the lower reaction temperatures tested (500 and 600°C), the first-hour conversion was slightly lower when H₂ was present than with pure N₂; however, for the higher temperatures tested (700 and 800°C) there were no significant differences in the level of conversion with the addition of H₂, with the exception of SV = 6300 h⁻¹ and T = 800°C, where the 1-hour conversion was recorded to be lower in the presence of H₂. However, since the replicates of this data point had to be disregarded due to instabilities in the hourly naphthalene feed during the experiment (explained in more detail in Chapter 3), the errors associated with this data point might be significant.

These observations are in contrast to the findings of Tamhankar et al. [87] who investigated benzene conversion with an iron-oxide/silica catalyst at a reactor temperature of 650°C and found that under identical conditions the catalyst performed significantly better in the presence of hydrogen. In that case, Mossbauer spectroscopic analysis of the catalyst revealed that the hematite phase only reduced to magnetite in the absence of hydrogen, while it was further reduced to metallic iron in the presence of H₂, which the authors believed explained the improvement in catalytic performance. Attempts to perform the Mossbauer analysis on our tested catalysts were unsuccessful, since to the best of my knowledge only one such device is in operation in Canada. Instead, X-ray powder diffraction techniques were utilized, with the results being previously presented. From Table 4.5, it can be seen that iron oxide in the form of magnetite and wustite were detected in addition to metallic iron when pure N₂ was used, whereas, when H₂ was used no iron oxides were detected (Table 4.8). However, since the quantities of these phases were not measured, it is difficult to draw any conclusions from these observations.

Moreover, the apparent reaction order was found to be equal to one for all reaction temperatures tested. This once again differed from what was previously found in reactions with pure N₂ and could be explained by differences in reaction pathways in the presence and absence of H₂. This is evident from the differences in physical and chemical characteristics of the catalyst between these two cases, which were discussed in more detail in the previous section; specifically the differences in the phases of iron present in the catalyst and consequently the nature of the active sites.

From the Arrhenius plot generated from the naphthalene conversion measurements, the activation energy of the reaction was calculated to be 37.3 ± 4.0 kJ/mol. The low level of the activation energy calculated could be justified considering the size of the catalyst pellets used in the experiments, 2 x 7.5 mm, which would result in large internal mass transfer limitation effects. Generally, without the use of any catalyst, reforming of tars mainly occurs at high activation energies of 250–350 kJ/mol [13]. For instance, the activation energy for thermal conversion of naphthalene with H₂O and H₂, in the absence of any catalysts, has been reported to be 350 kJ/mol [144]. This value, however, can be significantly lowered with the use of an appropriate catalyst. Table 4.10 summarizes some of the reported values in the literature for naphthalene reforming. It should be noted that a main problem in comparing these values is the fact that they have been conducted in different reaction conditions such as different media, different naphthalene loadings, as well as different reactors with different boundary conditions which, in addition to differences in the cracking reaction paths, could result in vast differences among them.

Table 4.10: Comparison of activation energies reported in the literature for naphthalene cracking with various catalysts

Media	Catalyst	E_{app} (kJ/mol)	Reference
H ₂ O + H ₂	Ni	332	[118]
Air	Pt/Al ₂ O ₃	150	[145]
Syngas	Olivine	141	[146]
8% H ₂ in N ₂ + H ₂ O	Char	63-72	[27]
O ₃ + O ₂ + N ₂	Pt/Al ₂ O ₃	68	[147]
N ₂	Ni-Fe-dolomite	64	[148]
H ₂ O + syngas	Char	61	[149]
13 wt.% H ₂ in N ₂	Red mud	37	This study

4.7 Long-term Tests

Due to restrictions in time and resources, long term tests were only performed for a space velocity of 5229 hr⁻¹ and a reactor temperature of 700°C, and, unfortunately, could only be carried out once. The main objectives of this test were to observe the trend in catalyst deactivation and to determine whether the addition of hydrogen would have any effects in the long term activity of the catalyst compared with pure N₂ in terms of the rate of deactivation.

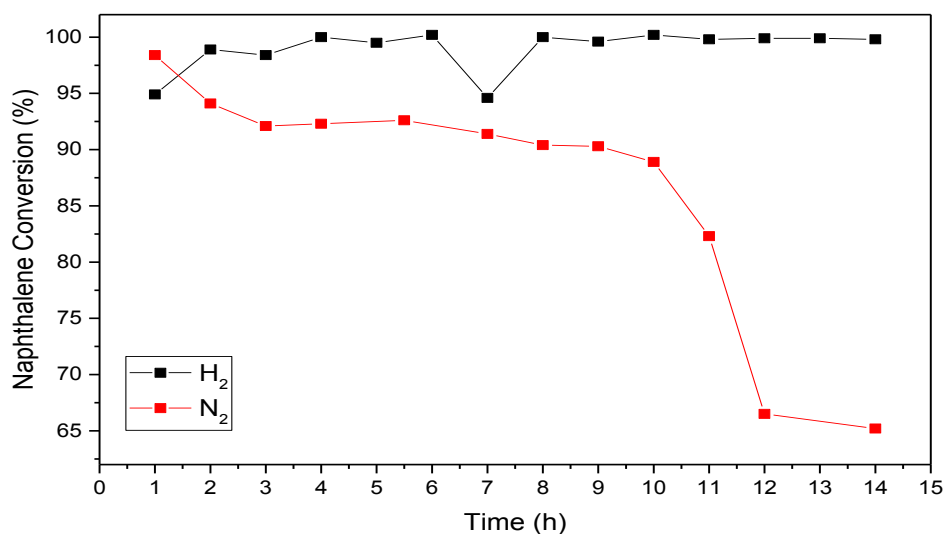


Figure 4.38: Long term activity of the RM catalyst in pure N₂ and 13 vol.% H₂ in balance N₂ at SV = 5229 h⁻¹

As can be seen in Fig. 4.38, in the absence of hydrogen there was a slow, steady decrease in the catalyst activity in the first 3 hours of the experiment. The activity remained relatively constant for the next 6 hours of the test, followed by a sharp decrease after the 10th hour, until the removal efficiency reduced to 65% at the end of the 14th hour. When hydrogen was added to the system, however, the activity of the catalyst improved from 95% to 99% within two hours of testing. This could be because the catalyst was not pre-reduced prior to the test and hence once the iron containing phase of the catalyst was fully reduced during the first two hours of the experiment, the removal efficiency improved. This is in line with the findings of Tamhankar et al. [87] who tested both pre-reduced and fresh iron oxide-based catalyst samples for benzene cracking and found that with the pre-reduced catalyst 100% benzene conversion was reached instantly; while, with the fresh catalyst the conversion was lower in the beginning and improved to the same level as the pre-reduced catalyst after a time corresponding to the reduction time of the catalyst. Nordgreen et al. [19] tested iron oxides as well as metallic iron as a tar

cracking catalyst and found none of the iron oxides possessed catalytic activity towards carbon breaking, while metallic iron exhibited a good performance. The results of experiments of Noichi et al. [88] with Fe-Al and Fe-Zr catalysts for steam reforming of naphthalene also showed that metallic iron provided the catalytic active sites.

Over the 14 h of the experiment, the catalyst activity remained very high at 100%. This is again similar to the findings of Tamhankar et al. [87] who examined an iron based catalyst for cracking of benzene, and observed that their reactant conversion stayed very high for 9 h when hydrogen was added to the system compared to when tested in an inert reaction environment.

The addition of hydrogen to the reaction environment could affect the long term activity of the catalyst by not only changing the reaction path, but possibly also due to hydrogenation of intermediate cracking products, hence preventing the catalyst active sites from blockage by removing coke pre-cursors [87]. In order to test this hypothesis additional testing needs to be performed on the catalyst.

4.8 Products

The possible products expected from the naphthalene cracking reactions included other condensed tertiary tars such as benzene, alkyl tertiary tars such as toluene, paraffins, non-condensables (ethane, methane, H₂), as well as carbonaceous residue (coke). However, with the resources available for these experiments, the only reaction products that could be identified were coke residues deposited on the surface of the catalyst, as well as water.

As described in Chapter 3, the gaseous product from the cracking reaction exiting the reactor was first bubbled through a bottle of cooled acetone (at -60°C) in order to condense and collect the condensable reaction products from the gas stream, and was

consequently sent to a Mandel SRI 8610C GC for analysis to determine the remaining non-condensable products. From the analysis of the collected acetone solution in a Shimadzu QP-2010S GCMS, the only product that was ever identified in the liquid stream was the remaining unreacted naphthalene. Formation of water during the reaction was visually detected in the set up since the acetone-containing collection bottle was blocked on multiple occasions during the experiment due to the condensation of the water present in the gas phase. Moreover, no other gaseous products could be detected in the GC. Considering that only about 100 ppmV of naphthalene was ever fed to the system, this was possibly due to the very low concentrations of the by-products formed, which were probably below the detection limits of the GC available for these analysis. Considering the stoichiometry of the cracking reaction of naphthalene in N₂ to methane, for instance, it can be readily calculated that the maximum amount of methane formed during the reaction, assuming a complete conversion of naphthalene to methane would be ~8E-03 ppm, and hence very challenging to detect.



In simple thermal conversion of naphthalene with H₂ and steam without any catalysts, Jess et al. [118] found the main reaction products to be soot, CO, CO₂, benzene, methane and C₂ hydrocarbons (mainly ethene), as well as small amounts of indene, indane, dihydronaphthalene and toluene. In steam reforming of naphthalene on Fe-Zr and Fe-Al catalysts with 20 vol.% H₂ in N₂, Noichi et al. [88] found the reaction products to be CO, H₂ and small amounts of CO₂. Tamhankar et al. [87] found methane to be their only detectable product in catalytic cracking of benzene over an iron oxide-silica catalyst with 10-25 vol.% H₂ in N₂. Furusawa et al. [150] tested a Ni/MgO catalyst in steam reforming of naphthalene in an inert gas mix (N₂/Ar), and found H₂, CO₂, CO, CH₄ and C₂H₄ as their

reaction products; however, when they increased the Ni content of their catalyst no more CH_4 and C_2H_4 could be detected in their product stream.

The tendency towards coke formation during tar cracking increases with the molecular weight of the reactant [29]. According to Tamhankar et al. [87] the intermediate coke precursors in the form of reactive α -carbon could either react with the hydrogen present in the reaction environment to form methane or transform to a more stable, unreactive form of carbon, β -carbon, which is responsible for catalyst deactivation. Hence if the rate of formation of β -carbon is higher than hydrogenation of α -carbon, the catalyst will start to decay. In order to test this hypothesis, the surface of the catalyst would need to be examined more carefully at various stages of the experiment.

Figure 4.39 has been removed due to copyright restrictions. It was an image of the deactivation routes of the catalyst due to coke formation [16, 27].

In an attempt to determine the amount of carbon deposited on the catalyst surface during the reaction, CHN analysis was performed on a sample of the spent catalyst. To account for the amount of carbon that already existed in the catalyst from before, it was necessary to perform the same analysis on a sample of the fresh red mud catalyst to establish a baseline. Since the amount of carbon deposition was not uniform throughout the catalyst bed, with the majority of the carbon deposited on the upper catalyst particles, the entire catalyst sample collected after the experiment was ground and mixed before a small sample was taken for CHN analysis. The results of this analysis are summarized below.

Table 4.11: CHN analysis of the fresh and spent catalyst pellet

Sample	Results (%)		
	C	H	N
Fresh	0.68	<0.3	<0.3
Spent	0.69	0.61	<0.3

It can be seen that the degree of increase in the amount of carbon detected in the catalyst is very small when comparing the spent catalyst to the fresh sample. This is due to the highly alkaline nature of red mud and the fact that CO₂ from the atmosphere is adsorbed chemically into it. In fact there is a great body of literature related to the use of red mud as a carbon sequestration agent. Part of the CO₂ reacts chemically with Ca and Na hydroxides in the red mud and is bound to it chemically [151-155]. Since the CO₂ is adsorbed from the atmosphere, the majority of this would exist on the surface of the material. This is further supported by the atomic percentage of elements found on the near-surface region of the catalyst with XPS (Table 4.12).

Table 4.12: XPS analysis of fresh and spent RM catalyst surface

Sample	Atomic (%)							
	Si	C	O	Na	Al	Fe	Ti	Ca
RM Powder	2.80	49.90	34.31	2.84	7.82	1.23	0.75	0.35
Fresh RM Pellet	3.53	48.99	33.19	2.05	10.13	1.23	0.87	-
Fresh RM Pellet*	3.23	53.23	31.35	2.15	8.02	1.28	0.74	-
Spent RM	3.59	56.59	26.88	2.44	8.14	1.23	0.62	0.5

*Prepared right before analysis.

As described in Chapter 3, the last step of the catalyst preparation procedure includes heating the prepared pellets to 350°C. The fact that the amount of carbon detected in the fresh catalyst pellet is still very high, suggests that the adsorbed carbon from the atmosphere cannot be easily removed by simple heating. In order to test this hypothesis and investigate whether the detected carbon could have been adsorbed on the surface of the catalyst in the time interval between catalyst preparation and testing, XPS was repeated on a catalyst sample which had been freshly prepared and heated right before the analysis at 350°C for 24 hours, and similar results were observed. This proves that indeed the detected carbon on the catalyst surface could not be removed by heating. Moreover, the amount of carbon that could potentially be formed through the course of the reaction and be deposited on the catalyst is very small compared to the carbon adsorbed from the atmosphere in the form of CO₂. Let us consider the naphthalene feeding rate which is 0.014 g/h (i.e. 0.013 g of C/h). Even assuming the most extreme case, i.e., 100% conversion of the reactant to coke deposited on the surface of the catalyst this would only constitute 0.22 wt.% of the total mass of the catalyst. Hence, measuring the amount of deposited carbon from naphthalene during the reaction on the catalyst surface would be very challenging. This problem may be avoided by using higher naphthalene concentrations in the feed and/or prolonging the duration of the experiment in future tests in order to generate enough coke deposit on the catalyst surface for analysis. Moreover, the results found may be indicating to the fact that coke deposition may not be a major factor in catalyst deactivation in the tests conducted, and perhaps catalyst sintering and chemical structure change are the major causes of deactivation.

There could also potentially be two main problems with this analysis. One, is that the catalyst consists of about 10% silicon oxide, which according to the literature may interfere with the CHN carbon content analysis by forming silicon carbide [117]. The second is that a fraction of the carbon was deposited on the bed support material as well

as the reactor surface, in close proximity to the catalyst, which was not accounted for in the previous analyses.

An attempt to perform TGA on the spent catalyst pellet with air also proved to be unsuccessful for measuring the amount of carbon deposited on the catalyst surface. This was due to the oxidation of the iron-containing phases present in the catalyst with air that resulted in a mass gain of ~4% in the catalyst (Fig. 4.40). Combining the TGA analysis with mass spectrometry and the analysis of the evolved gases, would enable the determination of the amount of carbon deposited on the catalyst in future tests.

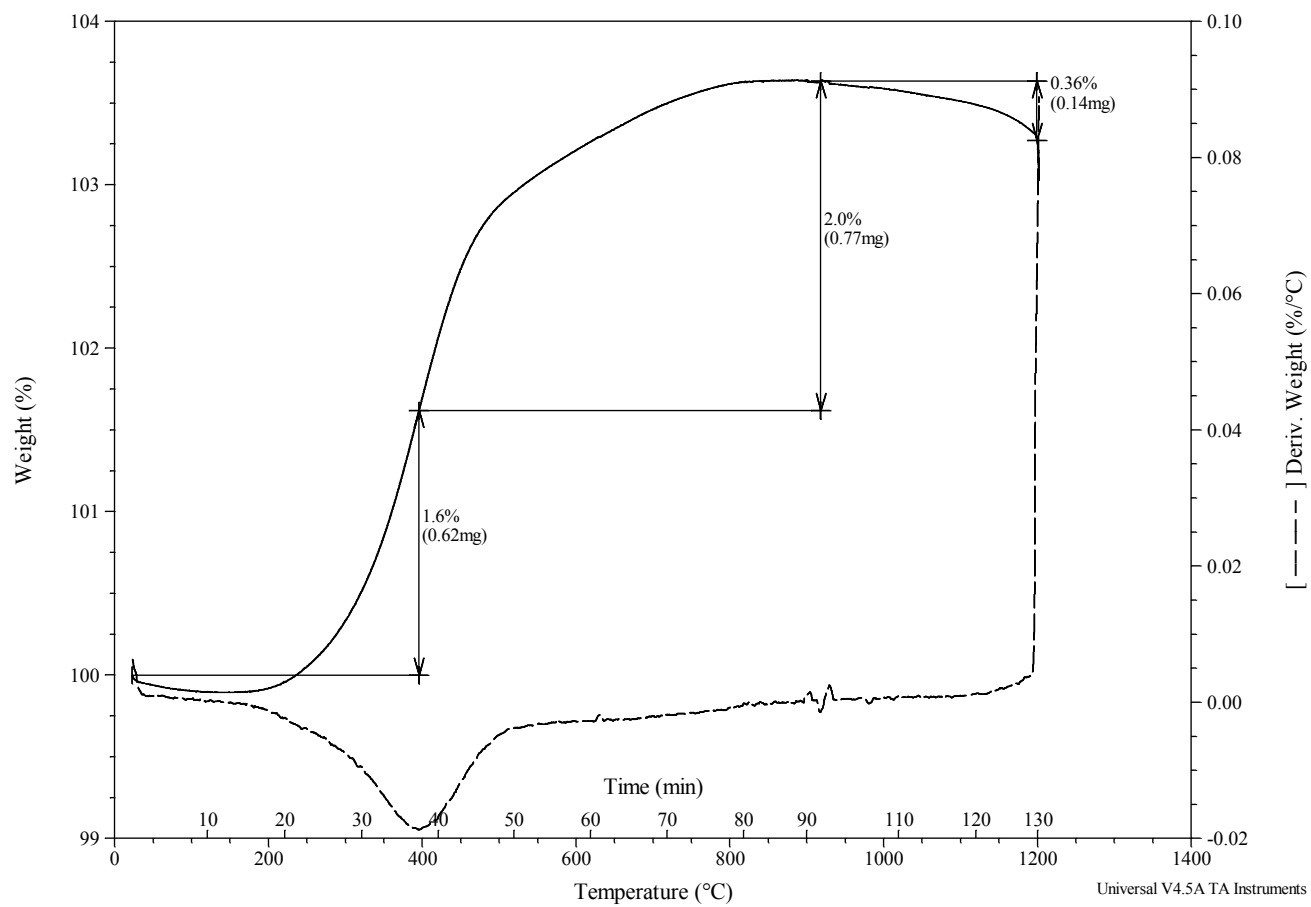


Figure 4.40: TGA analysis of spent catalyst with air

Chapter 5

Conclusion

The main focus of the research project at hand was to investigate the performance of red mud in removal of naphthalene as a model compound of biomass gasification tar. This was achieved by measuring the hourly naphthalene conversion of the catalyst at five space velocities and four reactor temperatures in the range of 500-800°C, in both a N₂ environment, and with 13 vol.% H₂ with balance N₂. The information gained from these tests was used to determine the apparent kinetic parameters of the reaction with red mud. Moreover, the activity of the catalyst was studied for a duration of 14 hours in both reaction environments to determine the long-term performance of the catalyst. The physical and chemical characteristics of the catalyst were studied prior to and after exposure to naphthalene to track the evolution of the catalyst as a result of the chemical reaction. In addition, the effects of calcination temperature and catalyst reduction with H₂ on the surface characteristics were investigated. Some of the insights gained through these experiments are summarized below:

- Temperature and space velocity were both found to have strong effects on improving the conversion of naphthalene with red mud.
- Preliminary benchmark tests revealed that the activity of the red mud catalyst was comparable to industrial Ni catalyst at temperatures of 800 and 850°C and a gas space velocity of 19,000 h⁻¹.

- The addition of hydrogen to the reaction environment did not result in any changes in the activity of the catalyst at the higher temperatures tested (700 and 800°C); however, at the lower reactor temperatures of 500 and 600°C, the performance of the catalyst was better in the N₂ environment.
- For the N₂ tests, kinetic analysis of the data showed a change in the apparent order of the reaction from 1 to 1.42, 1.64, and 1.35 for reaction temperatures of 500, 600, 700 and 800°C, respectively. Surface analysis of the catalyst, using BET analysis, SEM and XRD revealed drastic physical and chemical changes in the catalyst with temperature. This could potentially result in changes in reaction mechanism, which would ultimately be manifested in the kinetic parameters measured.
- The non-integer form of the reaction orders measured suggest that the kinetics of the adsorption of the other species present in the reaction environment on the catalytic active sites become non-negligible, affecting the apparent reaction order, considering the Langmuir-Hinshelwood equation.
- In the N₂ environment tests of naphthalene with red mud, the iron oxide phase of the catalyst was found to have transformed from hematite and goethite to magnetite, wustite and metallic iron after 1 hour of experimentation at 800°C. When tested for 14 hours, these phases were found to have transformed completely to metallic iron and ilmenite.
- For the tests in the reducing reaction environment, the reaction was found to be of 1st order for all temperatures tested. From the observed kinetic rate constants, the activation energy of the reaction was calculated to be 37.3 ± 4 kJ/mol.

- The reduction of the catalyst with hydrogen was found to have a severe impact on the surface area of the catalyst, reducing it by ~50%. XRD analysis of the catalyst surface revealed the only iron-containing phase of the catalyst to be metallic iron after reduction with H₂.
- Measurements of the activity of the catalyst over 14 hours of experimentation, showed the activity of the catalyst to decrease with time as a result of catalyst deactivation when tested in a N₂ reaction environment. In the presence of 13 vol.% H₂, however, the activity was found to remain very high for the entire duration of the experiment.
- CHN and XPS analyses of the catalyst revealed a high carbon content on the surface of the catalyst as a result of CO₂ adsorption from the atmosphere. The adsorbed carbon could not be removed from the catalyst by simple heating under air.
- The only reaction products detected during the tests were water and carbonaceous species (coke) on the surface of the catalyst.

5.1 Recommendations

There are many areas of this project that should be investigated in more depth in future tests. These include:

- Investigating the effect of calcination time and heating rate on the surface area and pore size distribution of the catalyst.
- Performing quantitative XRD analysis of the catalyst. Qualitative powder XRD has already been performed in this study to evaluate the evolution of the crystalline phases of the catalyst as a result of calcination, reduction and

exposure to the reaction conditions, and to determine the nature of the iron oxide species formed at each stage. Quantifying the amount of each mineral phase present would help gain more insight about the catalyst.

- The TGA measurements should be coupled with mass spectrometry to determine the nature of the products formed during the thermal analysis tests. Additionally, this would allow for the measurement of the amount of carbonaceous species existing on the spent catalyst.
- Further investigation of the long-term activity and exploration of the deactivation rate of the catalyst should be conducted, in both N₂ and H₂ environments. Moreover, the regenerability of the catalyst should be tested. This could be achieved by heating the spent catalyst pellets in the reactor in presence of oxygen to burn the deposited coke. The catalyst should then be tested again in the reactor to determine its performance.
- Different pre-treatment processes of red mud should be explored to further increase the surface area and decrease the degree of sintering (as a result of calcination and reduction with H₂). In this study, catalyst particles in the shape of cylindrical pellets were tested. Various other particle shapes of the catalyst, for instance spherical, should be tested. Moreover, the catalyst pellets could be pre-reduced in a stream of hydrogen at elevated temperatures of ~800°C in order to convert the iron-oxide content of the red mud to metallic iron prior to testing with naphthalene.
- The conversion of naphthalene should be tested in the presence of syngas. This was one of the preliminary objectives of the project; however, limitations in time did not allow further investigation. Since iron-based catalysts are very

active in Fischer-Tropsch synthesis, the activity of the catalyst needs to be first evaluated only with syngas, without the input of any tar compounds to determine the conversion level of CO. The addition of syngas to the system could lead to a significant increase in the carbon formation and deposition on the catalyst as a result of the Fischer-Tropsch synthesis.

- Investigate the activity of the red mud catalyst in cracking other tar compounds such as benzene, toluene, and phenol. Moreover, the simultaneous addition of two or more of these compounds in the system would allow the selectivity of the catalyst towards reforming each compound to be determined.
- Investigate the ability of various catalyst promoters and support materials to increase the surface area and durability of the catalyst, as well as to enhance the tar cracking activity.
- Test the catalyst with slip-streams from the Highbury/UBC Dual Fluidized Bed Gasifier, and the Nexterra/UBC Bioenergy Research and Demonstration Facility (BRDF).

References

[1] Climate Change 2014 Synthesis Report Summary for Policymakers, Intergovernmental panel on climate change (2014).

[2] Y. Richardson, J. Blin, A. Julbe, A short overview on purification and conditioning of syngas produced by biomass gasification: Catalytic strategies, process intensification and new concepts, *Progress in Energy and Combustion Science*. 38 (2012) 765-781.

[3] T. Fouilland, J.R. Grace, N. Ellis, Recent advances in fluidized bed technology in biomass processes, *Biofuels*. 1 (2010) 409-433.

[4] S. Anis, Z. Zainal, Tar reduction in biomass producer gas via mechanical, catalytic and thermal methods: A review, *Renewable and Sustainable Energy Reviews*. 15 (2011) 2355-2377.

[5] J. Gil, J. Corella, M.P. Aznar, M.A. Caballero, Biomass gasification in atmospheric and bubbling fluidized bed: Effect of the type of gasifying agent on the product distribution, *Biomass Bioenergy*. 17 (1999) 389-403.

[6] N. Xu, S.S. Kim, A. Li, J.R. Grace, C.J. Lim, T. Boyd, Investigation of the influence of tar-containing syngas from biomass gasification on dense Pd and Pd–Ru membranes, *Powder Technol.* 290 (2016) 132-140.

[7] Bioenergy Research and Demonstration Facility. 2016.

[8] M.L. Brown, W.S. Bulpitt, J.L. Walsh Jr, T.F. McGowan, Biomass and alternate fuel systems: an engineering and economic guide, John Wiley & Sons, 2011.

[9] S. Bengtsson, The CHRISGAS project, *Biomass Bioenergy*. 35 (2011) S2-S7.

[10] M. Cargobike, Max Planck, Fraunhofer institutes tap biomass for hydrogen, *Fuel Cells Bulletin* (2007).

[11] Energy research Centre of the Netherlands . 2016.

[12] H. Knoef, J. Ahrenfeldt, Handbook biomass gasification, BTG biomass technology group The Netherlands, 2005.

- [13] C. Xu, J. Donald, E. Byambajav, Y. Ohtsuka, Recent advances in catalysts for hot-gas removal of tar and NH₃ from biomass gasification, *Fuel*. 89 (2010) 1784-1795.
- [14] P.C. Bergman, S.V. van Paasen, H. Boerrigter, The novel "OLGA" technology for complete tar removal from biomass producer gas. 30 (2002).
- [15] D. Sutton, B. Kelleher, J.R.H. Ross, Review of literature on catalysts for biomass gasification, *Fuel Process Technol.* 73 (2001) 155-173.
- [16] S.S. Tamhankar, K. Tsuchiya, J.B. Riggs, Catalytic cracking of benzene on iron oxide-silica: catalyst activity and reaction mechanism, *Applied catalysis*. 16 (1985) 103-121.
- [17] T. Nordgreen, T. Liliedahl, K. Sjöström, Elemental iron as a tar breakdown catalyst in conjunction with atmospheric fluidized bed gasification of biomass: a thermodynamic study, *Energy Fuels*. 20 (2006) 890-895.
- [18] T. Nordgreen, V. Nemanova, K. Engvall, K. Sjöström, Iron-based materials as tar depletion catalysts in biomass gasification: Dependency on oxygen potential, *Fuel*. 95 (2012) 71-78.
- [19] T. Nordgreen, T. Liliedahl, K. Sjöström, Metallic iron as a tar breakdown catalyst related to atmospheric, fluidised bed gasification of biomass, *Fuel*. 85 (2006) 689-694.
- [20] V. Nemanova, T. Nordgreen, K. Engvall, K. Sjöström, Biomass gasification in an atmospheric fluidised bed: Tar reduction with experimental iron-based granules from Höganäs AB, Sweden, *Catalysis Today*. 176 (2011) 253-257.
- [21] M. Azhar Uddin, H. Tsuda, S. Wu, E. Sasaoka, Catalytic decomposition of biomass tars with iron oxide catalysts, *Fuel*. 87 (2008) 451-459.
- [22] A. Khelifa, V. Sharypov, G. Fiqueneisel, J.V. Weber, Catalytic pyrolysis and gasification of *Miscanthus Giganteus*: Haematite (Fe₂O₃) a versatile catalyst, *J. Anal. Appl. Pyrolysis*. 84 (2009) 84-88.
- [23] S. Hurley, C.C. Xu, F. Preto, Y. Shao, H. Li, J. Wang, G. Tourigny, Catalytic gasification of woody biomass in an air-blown fluidized-bed reactor using Canadian limonite iron ore as the bed material, *Fuel*. 91 (2012) 170-176.
- [24] R.T. Alcan, Production trends.
- [25] L.Y. Li, A study of iron mineral transformation to reduce red mud tailings, *Waste Manage.* 21 (2001) 525-534.
- [26] S. Sushil, V.S. Batra, Catalytic applications of red mud, an aluminium industry waste: A review, *Applied Catalysis B: Environmental*. 81 (2008) 64-77.

- [27] D. Fuentes-Cano, A. Gómez-Barea, S. Nilsson, P. Ollero, Decomposition kinetics of model tar compounds over chars with different internal structure to model hot tar removal in biomass gasification, *Chem. Eng. J.* 228 (2013) 1223-1233.
- [28] M.D. Brenes, *Biomass and bioenergy: new research*, Nova Publishers, 2006.
- [29] R. Coll, J. Salvadó, X. Farriol, D. Montané, Steam reforming model compounds of biomass gasification tars: conversion at different operating conditions and tendency towards coke formation, *Fuel Process Technol.* 74 (2001) 19-31.
- [30] D. Rulerk, *Removal of tar from biomass gasification process by steam reforming over nickel catalysts* (2011).
- [31] S. Ruyters, J. Mertens, E. Vassilieva, B. Dehandschutter, A. Poffijn, E. Smolders, The red mud accident in Ajka (Hungary): plant toxicity and trace metal bioavailability in red mud contaminated soil, *Environ. Sci. Technol.* 45 (2011) 1616-1622.
- [32] T.A. Milne, N. Abatzoglou, R.J. Evans, *Biomass gasifier" tars": Their nature, formation, and conversion*, National Renewable Energy Laboratory Golden, CO, 1998.
- [33] R.J. Evans, T.A. Milne, Molecular characterization of the pyrolysis of biomass, *Energy Fuels.* 1 (1987) 123-137.
- [34] V. Nemanova, *BIOMASS GASIFICATION IN ABFB: TAR MITIGATION* (2014).
- [35] Z. Abu El-Rub, E. Bramer, G. Brem, Review of catalysts for tar elimination in biomass gasification processes, *Ind Eng Chem Res.* 43 (2004) 6911-6919.
- [36] A. Bridgwater, The technical and economic feasibility of biomass gasification for power generation, *Fuel.* 74 (1995) 631-653.
- [37] W. Torres, S.S. Pansare, J.G. Goodwin, Hot Gas Removal of Tars, Ammonia, and Hydrogen Sulfide from Biomass Gasification Gas, *Catalysis Reviews.* 49 (2007) 407-456.
- [38] W. de Jong, Ö Ünal, J. Andries, K.R. Hein, H. Spliethoff, Biomass and fossil fuel conversion by pressurised fluidised bed gasification using hot gas ceramic filters as gas cleaning, *Biomass Bioenergy.* 25 (2003) 59-83.
- [39] C. Li, K. Suzuki, Tar property, analysis, reforming mechanism and model for biomass gasification—An overview, *Renewable and Sustainable Energy Reviews.* 13 (2009) 594-604.
- [40] K. Maniatis, A. Beenackers, Tar protocols. IEA bioenergy gasification task, *Biomass Bioenergy.* 18 (2000) 1-4.

- [41] D.C. Elliott, Relation of reaction time and temperature to chemical composition of pyrolysis oils, in: , 1988.
- [42] de Sousa, Luiz Carlos Reichenbach, , Gasification of wood, urban wastewood (Altholz) and other wastes in a fluidised bed reactor (2001).
- [43] A. Ponzio, S. Kalisz, W. Blasiak, Effect of operating conditions on tar and gas composition in high temperature air/steam gasification (HTAG) of plastic containing waste, *Fuel Process Technol.* 87 (2006) 223-233.
- [44] D. Bangala, N. Abatzoglou, E. Chornet, **Steam reforming of naphthalene on Ni-Cr/Al₂O₃ catalysts doped with MgO, TiO₂, and La₂O₃**, *AIChE.* 44 (1998) 927.
- [45] C.H. Bartholomew, R.J. Farrauto, *Fundamentals of industrial catalytic processes*, John Wiley & Sons, 2011.
- [46] L. Liinanki, N. Lindman, S. Sjöberg, E. Ström, Methane yield from biomass gasification at high temperature and pressure, in: *Fundamentals of thermochemical biomass conversion*, Springer, 1985, pp. 923-936.
- [47] W. Van de Kamp, P. De Wild, U. Zielke, M. Suomalainen, H. Knoef, J. Good, T. Liliedahl, C. Unger, M. Whitehouse, J. Neeft, Tar measurement standard for sampling and analysis of tars and particles in biomass gasification product gas (2005).
- [48] M.M. Yung, W.S. Jablonski, K.A. Magrini-Bair, Review of catalytic conditioning of biomass-derived syngas, *Energy Fuels.* 23 (2009) 1874-1887.
- [49] P.A. Simell, J. Bredenberg, Catalytic purification of tarry fuel gas, *Fuel.* 69 (1990) 1219-1225.
- [50] P.R. Buchireddy, R.M. Bricka, J. Rodriguez, W. Holmes, Biomass gasification: catalytic removal of tars over zeolites and nickel supported zeolites, *Energy Fuels.* 24 (2010) 2707-2715.
- [51] B. Dou, J. Gao, X. Sha, S.W. Baek, Catalytic cracking of tar component from high-temperature fuel gas, *Appl. Therm. Eng.* 23 (2003) 2229-2239.
- [52] A. Corma, G.W. Huber, L. Sauvanaud, P. O'connor, Processing biomass-derived oxygenates in the oil refinery: catalytic cracking (FCC) reaction pathways and role of catalyst, *Journal of Catalysis.* 247 (2007) 307-327.
- [53] J.D. Adjaye, N.N. Bakhshi, Production of hydrocarbons by catalytic upgrading of a fast pyrolysis bio-oil. Part II: Comparative catalyst performance and reaction pathways, *Fuel Process Technol.* 45 (1995) 185-202.

- [54] P.A. Simell, J.B.-. Bredenberg, Catalytic purification of tarry fuel gas, *Fuel*. 69 (1990) 1219-1225.
- [55] A. Corma, State of the art and future challenges of zeolites as catalysts, *Journal of Catalysis*. 216 (2003) 298-312.
- [56] W.Y. Wen, E. Cain, Catalytic pyrolysis of a coal tar in a fixed-bed reactor, *Industrial & Engineering Chemistry Process Design and Development*. 23 (1984) 627-637.
- [57] O. Cairon, K. Thomas, A. Chambellan, T. Chevreau, Acid-catalysed benzene hydroconversion using various zeolites: Brønsted acidity, hydrogenation and side-reactions, *Applied Catalysis A: General*. 238 (2003) 167-183.
- [58] A. Primo, H. Garcia, Zeolites as catalysts in oil refining, *Chem. Soc. Rev.* 43 (2014) 7548-7561.
- [59] S. Gao, C. Rhodes, J.B. Moffat, Ring-expansion of methylcyclopentane to cyclohexane and ring-contraction of cyclohexane to methylcyclopentane on silica-supported 12-tungstophosphoric acid and stoichiometric and nonstoichiometric microporous silver 12-tungstophosphate, *Catalysis letters*. 55 (1998) 183-188.
- [60] G. Jin, H. Iwaki, N. Arai, K. Kitagawa, Study on the gasification of wastepaper/carbon dioxide catalyzed by molten carbonate salts, *Energy*. 30 (2005) 1192-1203.
- [61] D.W. McKee, Mechanisms of the alkali metal catalysed gasification of carbon, *Fuel*. 62 (1983) 170-175.
- [62] Y. Huang, X. Yin, C. Wu, C. Wang, J. Xie, Z. Zhou, L. Ma, H. Li, Effects of metal catalysts on CO₂ gasification reactivity of biomass char, *Biotechnol. Adv.* 27 (2009) 568-572.
- [63] N. Choudhary, D. Saraf, Hydrocracking: A Review, *Industrial & Engineering Chemistry Product Research and Development*. 14 (1975) 74-83.
- [64] K. Polychronopoulou, J.L.G. Fierro, A.M. Efstathiou, The phenol steam reforming reaction over MgO-based supported Rh catalysts, *Journal of Catalysis*. 228 (2004) 417-432.
- [65] D. Duprez, P. Pereira, A. Miloudi, R. Maurel, Steam dealkylation of aromatic hydrocarbons: II. Role of the support and kinetic pathway of oxygenated species in toluene steam dealkylation over group VIII metal catalysts, *Journal of Catalysis*. 75 (1982) 151-163.
- [66] G.B. McVicker, M. Daage, M.S. Touvelle, C.W. Hudson, D.P. Klein, W.C. Baird Jr., B.R. Cook, J.G. Chen, S. Hantzer, D.E.W. Vaughan, E.S. Ellis, O.C. Feeley, Selective Ring Opening of Naphthenic Molecules, *Journal of Catalysis*. 210 (2002) 137-148.

- [67] D. Grenoble, The chemistry and catalysis of the water/toluene reaction: 2. The role of support and kinetic analysis, *Journal of Catalysis*. 51 (1978) 212-220.
- [68] D. Duprez, Selective steam reforming of aromatic compounds on metal catalysts, *Applied Catalysis A: General*. 82 (1992) 111-157.
- [69] Corella, - Two Advanced Models for the Kinetics of the Variation of the Tar Composition in Its Catalytic Elimination in Biomass Gasification, - *Ind. Eng. Chem. Res.* - 3001.
- [70] F. Auprêtre, C. Descorme, D. Duprez, Bio-ethanol catalytic steam reforming over supported metal catalysts, *Catalysis Communications*. 3 (2002) 263-267.
- [71] K. Tomishige, T. Miyazawa, M. Asadullah, S. Ito, K. Kunimori, Catalyst performance in reforming of tar derived from biomass over noble metal catalysts, *Green Chem*. 5 (2003) 399-403.
- [72] D. Sutton, S. Parle, J. Ross, The CO₂ reforming of the hydrocarbons present in a model gas stream over selected catalysts, *Fuel Process Technol*. 75 (2002) 45-53.
- [73] M. Asadullah, T. Miyazawa, S. Ito, K. Kunimori, K. Tomishige, Demonstration of real biomass gasification drastically promoted by effective catalyst, *Applied Catalysis A: General*. 246 (2003) 103-116.
- [74] T. Miyazawa, T. Kimura, J. Nishikawa, S. Kado, K. Kunimori, K. Tomishige, Catalytic performance of supported Ni catalysts in partial oxidation and steam reforming of tar derived from the pyrolysis of wood biomass, *Catalysis Today*. 115 (2006) 254-262.
- [75] H. Roh, K.Y. Koo, J.H. Jeong, Y.T. Seo, D.J. Seo, Y. Seo, W.L. Yoon, S.B. Park, Combined reforming of methane over supported Ni catalysts, *Catalysis Letters*. 117 (2007) 85-90.
- [76] Y. Matsumura, T. Nakamori, Steam reforming of methane over nickel catalysts at low reaction temperature, *Applied Catalysis A: General*. 258 (2004) 107-114.
- [77] Q. Zhang, Y. Li, B. Xu, Reforming of methane and coalbed methane over nanocomposite Ni/ZrO₂ catalyst, *Catalysis Today*. 98 (2004) 601-605.
- [78] B. Xu, J. Wei, Y. Yu, Y. Li, J. Li, Q. Zhu, Size limit of support particles in an oxide-supported metal catalyst: Nanocomposite Ni/ZrO₂ for utilization of natural gas, *The Journal of Physical Chemistry B*. 107 (2003) 5203-5207.
- [79] P.R. Buchireddy, R.M. Bricka, J. Rodriguez, W. Holmes, Biomass gasification: catalytic removal of tars over zeolites and nickel supported zeolites, *Energy Fuels*. 24 (2010) 2707-2715.
- [80] M. Inaba, K. Murata, M. Saito, I. Takahara, Hydrogen production by gasification of cellulose over Ni catalysts supported on zeolites, *Energy Fuels*. 20 (2006) 432-438.

- [81] C. Li, D. Hirabayashi, K. Suzuki, A crucial role of O₂- and O₂₂- on mayenite structure for biomass tar steam reforming over Ni/Ca₁₂Al₁₄O₃₃, *Applied Catalysis B: Environmental*. 88 (2009) 351-360.
- [82] S.M. Richardson, M.R. Gray, Enhancement of residue hydroprocessing catalysts by doping with alkali metals, *Energy Fuels*. 11 (1997) 1119-1126.
- [83] J. Juan-Juan, M. Román-Martínez, M. Illán-Gómez, Effect of potassium content in the activity of K-promoted Ni/Al₂O₃ catalysts for the dry reforming of methane, *Applied Catalysis A: General*. 301 (2006) 9-15.
- [84] J.H. Jeong, J.W. Lee, D.J. Seo, Y. Seo, W.L. Yoon, D.K. Lee, D.H. Kim, Ru-doped Ni catalysts effective for the steam reforming of methane without the pre-reduction treatment with H₂, *Applied Catalysis A: General*. 302 (2006) 151-156.
- [85] E. Nikolla, A. Holewinski, J. Schwank, S. Linic, Controlling carbon surface chemistry by alloying: carbon tolerant reforming catalyst, *J. Am. Chem. Soc.* 128 (2006) 11354-11355.
- [86] N. Vera, Biomass gasification in ABFB: Tar mitigation (2014).
- [87] S.S. Tamhankar, K. Tsuchiya, J.B. Riggs, Catalytic cracking of benzene on iron oxide-silica: catalyst activity and reaction mechanism, *Applied catalysis*. 16 (1985) 103-121.
- [88] H. Noichi, A. Uddin, E. Sasaoka, Steam reforming of naphthalene as model biomass tar over iron-aluminum and iron-zirconium oxide catalysts, *Fuel Process Technol.* 91 (2010) 1609-1616.
- [89] Z. Min, M. Asadullah, P. Yimsiri, S. Zhang, H. Wu, C. Li, Catalytic reforming of tar during gasification. Part I. Steam reforming of biomass tar using ilmenite as a catalyst, *Fuel*. 90 (2011) 1847-1854.
- [90] M. Koike, D. Li, H. Watanabe, Y. Nakagawa, K. Tomishige, Comparative study on steam reforming of model aromatic compounds of biomass tar over Ni and Ni-Fe alloy nanoparticles, *Applied Catalysis A: General*. 506 (2015) 151-162.
- [91] A. Atasoy, An investigation on characterization and thermal analysis of the Aughinish red mud, *Journal of thermal analysis and calorimetry*. 81 (2005) 357-361.
- [92] S. Sushil, V. Batra, CHARACTERIZATION OF INDIAN RED MUD FOR CATALYTIC APPLICATIONS, *The Journal of Solid Waste Technology and Management*. 37 (2011) 188-196.
- [93] H.S. Altundoğan, S. Altundoğan, F. Tuğmen, M. Bildik, Arsenic removal from aqueous solutions by adsorption on red mud, *Waste Manage.* 20 (2000) 761-767.

- [94] A. López, I. De Marco, B. Caballero, M. Laresgoiti, A. Adrados, A. Aranzabal, Catalytic pyrolysis of plastic wastes with two different types of catalysts: ZSM-5 zeolite and Red Mud, *Applied Catalysis B: Environmental*. 104 (2011) 211-219.
- [95] J. Pascual, F. Corpas, J. López-Beceiro, M. Benítez-Guerrero, R. Artiaga, Thermal characterization of a Spanish red mud, *Journal of Thermal Analysis and Calorimetry*. 96 (2008) 407-412.
- [96] S. Yokoyama, M. Yamamoto, Y. Maekawa, T. Kotanigawa, Catalytic activity of sulphate for hydroliquefaction of coal by using diphenylether and diphenylmethane, *Fuel*. 68 (1989) 531-533.
- [97] A. Mastral, C. Mayoral, M. Izquierdo, C. Pardos, Iron catalyzed hydrogenation of high sulphur content coals, *Fuel Process Technol.* 36 (1993) 177-184.
- [98] B. Klopries, W. Hodek, F. Bandermann, Catalytic hydroliquefaction of biomass with red mud and CoO-MoO₃ catalysts, *Fuel*. 69 (1990) 448-455.
- [99] I. Metecan, T. Karayildirim, J. Yanik, M. Saglam, M. Yuksel, The effect of sulfur-promoted red mud catalysts on hydroliquefaction of oil shale, *Oil Shale*. 20 (2003) 0208-189X.
- [100] S. Ordonez, H. Sastre, F. Díez, Catalytic hydrodechlorination of tetrachloroethylene over red mud, *J. Hazard. Mater.* 81 (2001) 103-114.
- [101] S. Ordóñez, H. Sastre, F.V. Díez, Characterisation and deactivation studies of sulfided red mud used as catalyst for the hydrodechlorination of tetrachloroethylene, *Applied Catalysis B: Environmental*. 29 (2001) 263-273.
- [102] J. Halász, M. Hodos, I. Hannus, G. Tasi, I. Kiricsi, Catalytic detoxification of C 2-chlorohydrocarbons over iron-containing oxide and zeolite catalysts, *Colloids Surf. Physicochem. Eng. Aspects*. 265 (2005) 171-177.
- [103] J.R. Paredes, S. Ordóñez, A. Vega, F.V. Díez, Catalytic combustion of methane over red mud-based catalysts, *Applied Catalysis B: Environmental*. 47 (2004) 37-45.
- [104] S. Khalafalla, L. Haas, The role of metallic component in the iron-alumina bifunctional catalyst for reduction of SO₂ with CO, *Journal of catalysis*. 24 (1972) 121-129.
- [105] H. Hosoda, T. Hirama, H. Aoki, SIMULTANEOUS REDUCTION TECHNIQUES OF NITROUS AND NITROGEN-OXIDES FROM FLUIDIZED-BED COAL COMBUSTOR, *Kagaku kogaku ronbunshu*. 21 (1995) 74-82.
- [106] A.I. Cakici, J. Yanik, S. Uçar, T. Karayildirim, H. Anil, Utilization of red mud as catalyst in conversion of waste oil and waste plastics to fuel, *Journal of Material Cycles and Waste Management*. 6 (2004) 20-26.

- [107] A. Iannibello, S. Marengo, A. Girelli, Bauxite-based catalysts in heavy crude oil hydrotreating, *Applied Catalysis*. 3 (1982) 261-272.
- [108] H. Nath, P. Sahoo, A. Sahoo, Characterization of Red Mud treated under high temperature fluidization, *Powder Technol.* 269 (2015) 233-239.
- [109] O. Teplov, N. Korenovskii, Y.A. Lainer, Thermogravimetric study of the dehydration and reduction of red mud, *Russian Metallurgy (Metally)*. 2015 (2015) 12-18.
- [110] S. Meher, Thermal analysis of nalco red mud, *Int.J.Chem.Stud.* 1 (2014) 1-9.
- [111] S. Sushil, V.S. Batra, Modification of red mud by acid treatment and its application for CO removal, *J. Hazard. Mater.* 203–204 (2012) 264-273.
- [112] P. Wang, D. Liu, Physical and chemical properties of sintering red mud and bayer red mud and the implications for beneficial utilization, *Materials*. 5 (2012) 1800-1810.
- [113] C. Wu, D. Liu, Mineral phase and physical properties of red mud calcined at different temperatures, *Journal of Nanomaterials*. 2012 (2012) 2.
- [114] J.R. Mercury, A. Cabral, A. Paiva, R. Angélica, R. Neves, T. Scheller, Thermal behavior and evolution of the mineral phases of Brazilian red mud, *Journal of thermal analysis and calorimetry*. 104 (2011) 635-643.
- [115] R.C. Costa, F.C. Moura, P.E. Oliveira, F. Magalhães, J.D. Ardisson, R.M. Lago, Controlled reduction of red mud waste to produce active systems for environmental applications: heterogeneous Fenton reaction and reduction of Cr (VI), *Chemosphere*. 78 (2010) 1116-1120.
- [116] S. Dulger Irдем, E. Parparita, C. Vasile, M.A. Uddin, J. Yanik, Steam Reforming of Tar Derived from Walnut Shell and Almond Shell Gasification on Red Mud and Iron–Ceria Catalysts, *Energy Fuels*. 28 (2014) 3808-3813.
- [117] C. Maloney, , Canadian microanalytical Services. Email correspondece.
- [118] A. Jess, Mechanisms and kinetics of thermal reactions of aromatic hydrocarbons from pyrolysis of solid fuels, *Fuel*. 75 (1996) 1441-1448.
- [119] Y. Wang, X. Hu, Y. Song, Z. Min, D. Mourant, T. Li, R. Gunawan, C. Li, Catalytic steam reforming of cellulose-derived compounds using a char-supported iron catalyst, *Fuel Process Technol.* 116 (2013) 234-240.
- [120] J.A. Moulijn, A. Van Diepen, F. Kapteijn, Catalyst deactivation: is it predictable?: What to do?, *Applied Catalysis A: General*. 212 (2001) 3-16.

- [121] X. Zhai, J. Shamoto, H. Xie, Y. Tan, Y. Han, N. Tsubaki, Study on the deactivation phenomena of Cu-based catalyst for methanol synthesis in slurry phase, *Fuel*. 87 (2008) 430-434.
- [122] H. Liu, *Ammonia Synthesis Catalysts: Innovation and Practice*, World Scientific, 2013.
- [123] V.I. Kanazirev, S.R. Caskey, , *Method of Making Supported Copper Adsorbents Having Copper at Selectively Determined Oxidation Levels* (2012).
- [124] G. Harada, T. Yen, M. Tomari, , *Process for treating molten steel slag with red mud from aluminum industry* (1979).
- [125] G. Leofanti, M. Padovan, G. Tozzola, B. Venturelli, Surface area and pore texture of catalysts, *Catalysis Today*. 41 (1998) 207-219.
- [126] T. Wang, J. Chang, P. Lv, J. Zhu, Novel catalyst for cracking of biomass tar, *Energy Fuels*. 19 (2005) 22-27.
- [127] A. Atasoy, The comparison of the Bayer process wastes on the base of chemical and physical properties, *Journal of Thermal Analysis and Calorimetry*. 90 (2007) 153-158.
- [128] Q. Yue, Y. Zhao, Q. Li, W. Li, B. Gao, S. Han, Y. Qi, H. Yu, Research on the characteristics of red mud granular adsorbents (RMGA) for phosphate removal, *J. Hazard. Mater.* 176 (2010) 741-748.
- [129] S.C. Kim, S.W. Nahm, Y. Park, Property and performance of red mud-based catalysts for the complete oxidation of volatile organic compounds, *J. Hazard. Mater.* 300 (2015) 104-113.
- [130] D. Lu, Y. Qi, Q. Yue, F. Xi, B. Gao, Properties and mechanism of red mud in preparation of ultra-lightweight sludge-red mud ceramics, *Journal of Central South University*. 19 (2012) 231-237.
- [131] Y. Liu, C. Lin, Y. Wu, Characterization of red mud derived from a combined Bayer Process and bauxite calcination method, *J. Hazard. Mater.* 146 (2007) 255-261.
- [132] Q. Liu, R. Xin, C. Li, C. Xu, J. Yang, Application of red mud as a basic catalyst for biodiesel production, *Journal of Environmental Sciences*. 25 (2013) 823-829.
- [133] A. Alp, M. Goral, The influence of soda additive on the thermal properties of red mud, *Journal of thermal analysis and calorimetry*. 73 (2003) 201-207.
- [134] V.M. Sglavo, R. Campostrini, S. Maurina, G. Carturan, M. Monagheddu, G. Budroni, G. Cocco, Bauxite 'red mud' in the ceramic industry. Part 1: thermal behaviour, *Journal of the European Ceramic Society*. 20 (2000) 235-244.

- [135] B. Li, R.D. Gonzalez, The measurement of small amounts of coke by a sensitive TGA/FTIR technique, *Catalysis letters*. 54 (1998) 5-8.
- [136] A. Mnrrnws, Magnetite formation by the reduction of hematite with iron under hydrothermal conditions, *Am. Mineral*. 6 (1976) 927-932.
- [137] M. Grigore, R. Sakurovs, D. French, V. Sahajwalla, Influence of mineral matter on coke reactivity with carbon dioxide, *ISIJ Int*. 46 (2006) 503-512.
- [138] S. Nomura, H. Ayukawa, H. Kitaguchi, T. Tahara, S. Matsuzaki, M. Naito, S. Koizumi, Y. Ogata, T. Nakayama, T. Abe, Improvement in blast furnace reaction efficiency through the use of highly reactive calcium rich coke, *ISIJ Int*. 45 (2005) 316-324.
- [139] J. Yagi, Science and Technology of Innovative Ironmaking for aiming at Energy half consumption, *ISIJ*, Tokyo. 251 (2003).
- [140] R.B. Cahyono, N. Yasuda, T. Nomura, T. Akiyama, Optimum temperatures for carbon deposition during integrated coal pyrolysis–tar decomposition over low-grade iron ore for ironmaking applications, *Fuel Process Technol*. 119 (2014) 272-277.
- [141] K. Johnson, CHE 400 Reactive Process Engineering lecture notes (2008).
- [142] D.B. Bukur, K. Okabe, M.P. Rosynek, C. Li, D. Wang, K. Rao, G. Huffman, Activation studies with a precipitated iron catalyst for fischer-tropsch synthesis: I. characterization studies, *Journal of Catalysis*. 155 (1995) 353-365.
- [143] G. Bian, A. Oonuki, N. Koizumi, H. Nomoto, M. Yamada, Studies with a precipitated iron Fischer-Tropsch catalyst reduced by H₂ or CO, *Journal of Molecular Catalysis A: Chemical*. 186 (2002) 203-213.
- [144] A. Jess, Mechanisms and kinetics of thermal reactions of aromatic hydrocarbons from pyrolysis of solid fuels, *Fuel*. 75 (1996) 1441-1448.
- [145] J. Shie, C. Chang, J. Chen, W. Tsai, Y. Chen, C. Chiou, C. Chang, Catalytic oxidation of naphthalene using a Pt/Al₂O₃ catalyst, *Applied Catalysis B: Environmental*. 58 (2005) 289-297.
- [146] L. Devi, Catalytic removal of biomass tars: olivine as prospective in-bed catalyst for fluidized-bed biomass gasifiers (2005).
- [147] M. Yuan, C. Chang, J. Shie, C. Chang, J. Chen, W. Tsai, Destruction of naphthalene via ozone-catalytic oxidation process over Pt/Al₂O₃ catalyst, *J. Hazard. Mater*. 175 (2010) 809-815.

- [148] Y. Sun, J. Jiang, E. Kantarelis, J. Xu, L. Li, S. Zhao, W. Yang, Development of a bimetallic dolomite based tar cracking catalyst, *Catalysis Communications*. 20 (2012) 36-40.
- [149] Z. Abu El-Rub, E.A. Bramer, G. Brem, Experimental comparison of biomass chars with other catalysts for tar reduction, *Fuel*. 87 (2008) 2243-2252.
- [150] T. Furusawa, A. Tsutsumi, Comparison of Co/MgO and Ni/MgO catalysts for the steam reforming of naphthalene as a model compound of tar derived from biomass gasification, *Applied Catalysis A: General*. 278 (2005) 207-212.
- [151] D. Bonenfant, L. Kharoune, S. Sauvé, R. Hausler, P. Niquette, M. Mimeault, M. Kharoune, CO₂ sequestration by aqueous red mud carbonation at ambient pressure and temperature, *Ind Eng Chem Res*. 47 (2008) 7617-7622.
- [152] R.C. Sahu, R.K. Patel, B.C. Ray, Neutralization of red mud using CO₂ sequestration cycle, *J. Hazard. Mater*. 179 (2010) 28-34.
- [153] G. Jones, G. Joshi, M. Clark, D. McConchie, Carbon capture and the aluminium industry: preliminary studies, *Environmental Chemistry*. 3 (2006) 297-303.
- [154] P. Renforth, W. Mayes, A. Jarvis, I. Burke, D. Manning, K. Gruiz, Contaminant mobility and carbon sequestration downstream of the Ajka (Hungary) red mud spill: the effects of gypsum dosing, *Sci. Total Environ*. 421 (2012) 253-259.
- [155] V.S. Yadav, M. Prasad, J. Khan, S. Amritphale, M. Singh, C. Raju, Sequestration of carbon dioxide (CO₂) using red mud, *J. Hazard. Mater*. 176 (2010) 1044-1050.
- [156] ChERIC: Chemical engineering and materials research information centre. 2014.
- [157] Dortmund Data Bank. 2015.
- [158] PEACE Software. 2016.
- [159] S. Fogler, External Resistance to Mass Transfer, in: *Elements of Chemical Reaction Engineering*, Prentice Hall, 2006, pp. 786.
- [160] O. Levenspiel, Experimental Values for Axial Dispersion, in: *Tracer Technology: Modeling the Flow of Fluids*, Springer, New York, 2011, pp. 61.

Appendix A

Theoretical Naphthalene Feeding Rate

From the Antoine equation constants of naphthalene, the vapour pressure vs. temperature plot can be constructed as is shown in Figure A1.

Table A1: Antoine equation constants of naphthalene [156, 157]

$y = A*(\ln T) + B/T + C + D*T^2$					
T > 355 K	y	A	B	C	D
	$\ln(P_{vp})$	-7.6706	-8563.7	68.8881	2.8621E-06
$y = A - B/T$					
T < 355 K	y	A	B		
	$\log(P_{vp})$	11.579	3783		

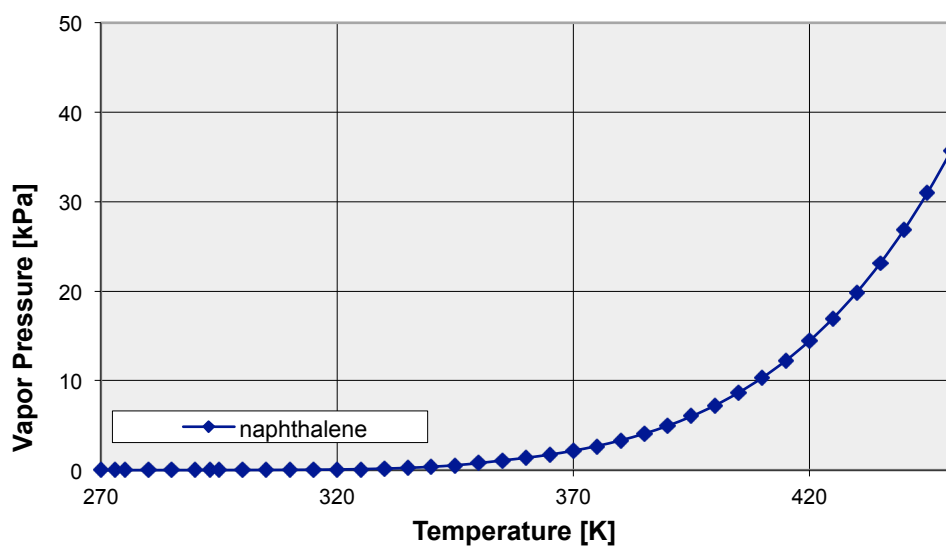


Figure A1: Equilibrium vapour pressure of naphthalene vs. temperature

Assuming an ideal gas mix, the following relation holds:

$$\frac{P_i}{P_T} = \frac{V_i}{V_T} \quad A - 1$$

Where P_i and P_T refer to the partial pressure of each gas component and the total pressure of the mixture, and V_i and V_T refer to the partial volume of the component and the total volume respectively.

From the Antoine equation, the partial pressure of naphthalene at an equilibrium temperature of 53°C is found to be 0.1310 kPa. Assuming atmospheric pressure in the feed flask, the volume fraction of naphthalene in the gas phase can be calculated as:

$$Vol \% = \frac{V_{naphthalene}}{V_T} = \frac{0.1310 \text{ kPa}}{101 \text{ kPa}} = 0.1297 \% \quad A - 2$$

$$V_T = V_{naphthalene} + V_{N_2} \quad A - 3$$

Since $V_{N_2} = 38 \text{ mL/min}$ at 53°C, $V_{naphthalene}$ is calculated to be 0.0455 mL/min.

Assuming the ideal gas law holds:

$$PV = nRT \quad A - 4$$

The molar flow of naphthalene is calculated to be 0.00171 mol/min. Hence, the theoretical hourly amount of naphthalene fed is calculated to be 0.01318 g/h.

Table A2: The theoretical net hourly amount of naphthalene feeding rate

MFC1_naph	L/min	0.035
MFC_N2 at 25°C	L/min	0.35
T naph	K	326.15
Vol.% naph		0.1310
ppmV naph		1310.326
Vol naph	L/min	0.00005
Mol mass naph	mol/min	0.00000
Mass naph	g/min	0.00022
Mass naph	g/h	0.01318
Concentration naph	g/m ³	6.278
Experimental time	h	1
Total naphthalene evaporated	g	0.01318

Appendix B

Benchmark Test Operating Parameters

The main test parameters of benchmark tar cracking experiments were developed in a joint meeting between UBC, Fraunhofer Umsicht and ISE and are summarized in Table B1.

Table B1: Main parameters of benchmark tar cracking experiments

Parameter	Unit	ISE	Umsicht	UBC
Reactor inner diameter (ID)	mm	21.00	18	15
Catalyst (bed) length	mm	42.00	34	30
Height to diameter ratio	-	2.00	1.9	2
Carrier gas	-	N ₂	Syngas	N ₂
Volumetric gas flow rate	L/min	1.60	2	0.398
Gas residence time	s	0.80	0.04	0.8
Gas velocity in reactor	cm/s	10.50	52	42.71
Space velocity at STP (GHSV)	h ⁻¹	4500.00	16 000	4500
Benzene load	Vol.%	0.13	0.15	
Benzene concentration	g/m ³	4.50	5.2	
Naphthalene load	ppmV	100.00	370	100
Naphthalene concentration	g/m ³		2.1	
Temperature range	°C	800 -1050	700 - 900	800-950

Agreed-upon Catalyst Activation Procedure

The benchmark catalyst was an industrial Ni-based catalyst provided by Johnson-Matthey©. In order to activate the catalyst, the desired amount was placed in the reactor and was heated at 650°C for 3 hours under a constant flow of 10 vol.% H₂ in balance N₂.

Table B2: Benchmark catalyst activation parameters

Carrier gas		N ₂
Gas mixture H ₂ concentration	%	5-10
Activation temperature	°C	650
Duration	h	3
Volume flow total	mL/min	44.0
Volume flow H ₂	mL/min	4.0
Volume flow N ₂	mL/min	40.0

Appendix C

Naphthalene Conversion Calculation

In order to perform the sample calculation, the 1st and 2nd hour measurements of one sample test are included below. The test was completed under 13 vol.% H₂ in balance N₂ over a duration of 1 hour with 3.85 g of catalyst (GHSV = 5229 h⁻¹) at 700°C.

From the mass of the impinger bottle prior to and after the addition of acetone, the net amount of acetone initially added to the bottle was calculated to be 177.6 g, which corresponds to 0.225 L of acetone. After the 1st hour of the experiment through the bypass line, three samples were taken from the impinger bottle (vials 1-1 to 1-3). The net amount of sample taken from each vial is measured. From the area of naphthalene found through the GCMS and the calibration constant, the concentration of naphthalene in each vial is calculated. The average weight of naphthalene in the impinger bottle and the corresponding standard error were then calculated according to:

$$m (avg) = V_i \cdot \frac{\sum C_i}{3} \quad C - 1$$

$$SE = \frac{\sigma}{\sqrt{n}} \quad C - 2$$

Where $m(avg)$ refers to the average weight of naphthalene in the impinger bottle, V_i refers to the volume of acetone in the impinger bottle (prior to taking the samples), C_i is

the concentration of naphthalene in each sample vial, σ is the standard deviation of the weight of naphthalene in the sample vials and n is the sample size (3).

As can be seen in Table C1, the first-hour amount of naphthalene measured through the bypass line was 0.0153g. This value was used as the hourly amount of feed to calculate the degree of conversion for all the following hours of the experiment.

The net amount of acetone left in the impinger bottle (V_i) was calculated by subtracting the amount of the samples taken during the 1st hour (Vials 1-1 to 1-3) from the initial amount of acetone in the bottle. As can be seen in Table C1, this was found to be 0.220 L. Using this value as the new value for V_i in equation C-1, as well as the measured naphthalene areas in vials 2-1 to 2-3 with the GCMS, the average weight of naphthalene in the impinger bottle after the second hour of the experiment and its standard error were calculated to be 0.01567g and 0.00015g respectively.

Subtracting the total weight of naphthalene measured during the second hour, 0.01567g, from the initial amount collected during the first hour, $m_1 = 0.01527$, the net amount of naphthalene condensed in the bottle during the second hour of the experiment (Δm) was found to be 0.0004g. Hence the degree of naphthalene conversion (X) could be calculated according to C-3 and was found to be 97.4% during this hour.

$$X (\%) = \left(1 - \frac{\Delta m}{m_1}\right) * 100\% \quad C - 3$$

Table C1: Sample data from test on red mud catalyst in presence of 13 vol.% H₂ in balance N₂ with 3.85g

			1 st hour - Bypass line			2 nd hour - T = 700C, m = 3.85g			
			Vial 1-1	Vial 1-2	Vial 1-3	Vial 2-1	Vial 2-2	Vial 2-3	
Weight empty impinger	g	266.5	2.17	2.18	2.17	2.16	2.15	2.15	
Weight impinge + acetone	g	444.1	3.28	3.36	3.34	3.34	3.27	3.36	
Net weight acetone	g	177.6	1.11	1.18	1.17	1.18	1.12	1.21	
Volume acetone	L	0.2246	0.0014	0.0015	0.0015	0.2202	0.0015	0.0014	0.0015
Area measured by GCMS			5153912	5210375	5201545		5415413	5527209	5348337
C naphthalene in vial	g/L		0.068	0.068	0.068		0.071	0.072	0.070
Average weight naphthalene	g	0.01527				0.01567			
Standard error in weight	g	0.00005				0.00015			
Net mass of naphthalene		0.0153				0.0004			
$\Delta m/m1$						0.0262			
Conversion (%)						97.4			

Appendix D

Kinetic parameters calculations

Linear Regression Plots

The procedure for determining the reaction orders was previously described in section 4.5.2. The results of linear regression performed by OriginLab© are included in Figures D1 to D3. Each experimental test condition was tested several times, the results of which were previously reported in Figure 4.8, with conversion (X) being the average value of all conversions found for each test condition, and the error bars corresponding to the standard deviation between these measurements. For instance, for a reactor temperature of 800°C and GHSV of 5229 h⁻¹, the experiment was repeated 3 times and the following experimental results were found:

Table D1: Experimental results found for T = 800°C, GHSV = 5229 h⁻¹ under pure N₂

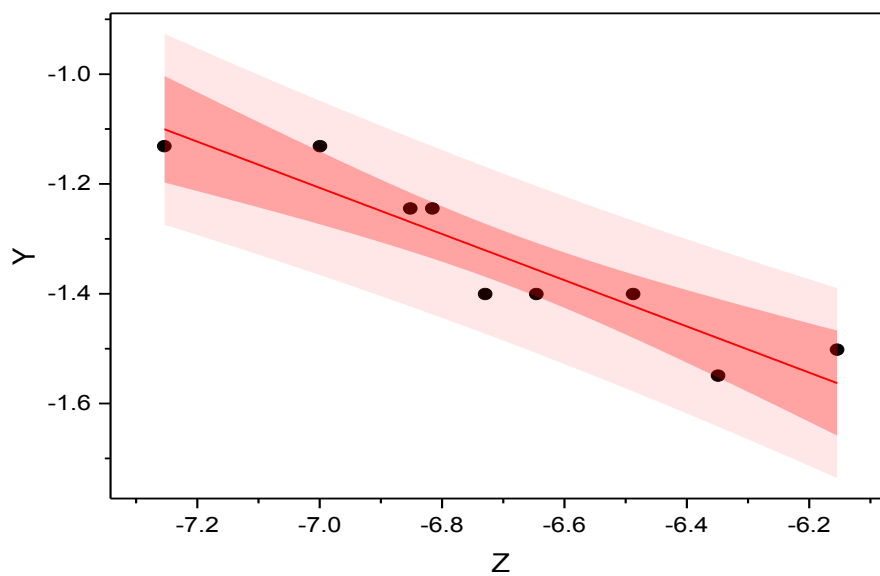
W cat (g)	m_naph (g/h)	X(%)	Ca ₀ (mol/L)
3.85	0.015	98.4	1.398E-06
3.85	0.016	98.0	1.467E-06
3.85	0.015	98.1	1.374E-06
Average Conversion (%)			98.2
Standard Deviation			0.208
Standard Error			0.120
Average Ca₀ (mol/L)			1.413E-06
Standard Error in Ca₀			4.816E-08

In order to perform linear regression on Equation 4.20 to find the reaction order, instead of using the average values of X and C_{A_0} , all experimental data points were plotted individually for better accuracy of the estimated parameter. For instance the data in Table D1 were used to construct the following:

Table D2: Derived parameters for the determination of the reaction order with linear regression for $T = 800^\circ\text{C}$, $\text{GHSV} = 5229 \text{ h}^{-1}$ under pure N_2

$W \text{ cat (g)}$	$m_{A_0}(\text{g/hr})$	$X (\%)$	$C_{A_0}(\text{mol/L})$	$\log(C_{A_0}(1-X))$	$\log(W/V)$
3.85	0.0149	98.4	1.398E-06	-7.65	-1.53
3.85	0.0156	98.0	1.467E-06	-7.53	-1.53
3.85	0.0146	98.1	1.374E-06	-7.58	-1.53

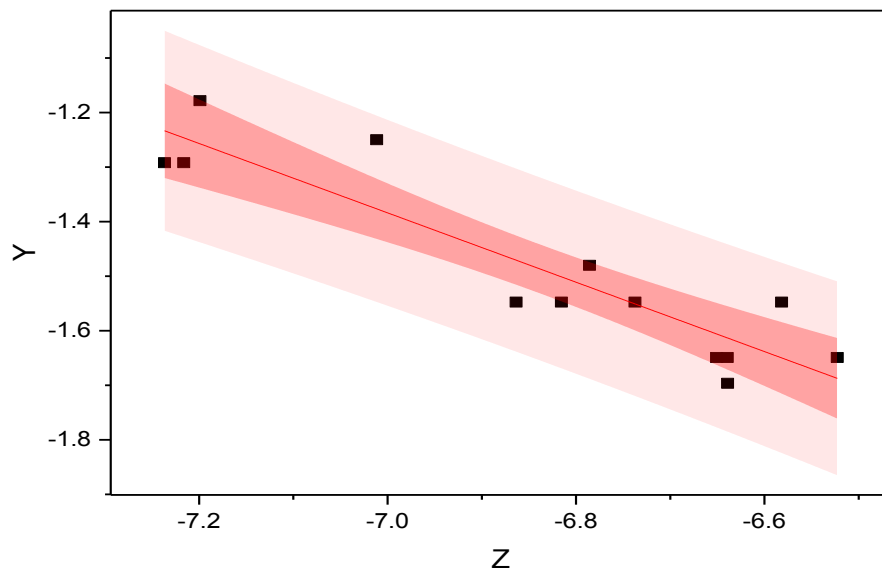
These parameters were then calculated for all other space velocities tested at each specific reactor temperature. As described in Section 4.5.2, the plot of Y (previously defined as $\log(W/V)$) vs. Z (defined as $\log(C_{A_0}(1-X))$), could be used to determine the reaction order, n , at each temperature through linear regression (Figures D1-D3); Note, however, that in constructing Figures 4.10-4.12 in section 4.5.2, the average values of conversion and C_{A_0} were used instead of each individual measurement.



n	n	b	b	Statistics
Value	Standard Error	Value	Standard Error	R-Square
1.42	0.06	4.15	0.43	0.83953

Figure D1: Linear regression for the estimation of reaction order.

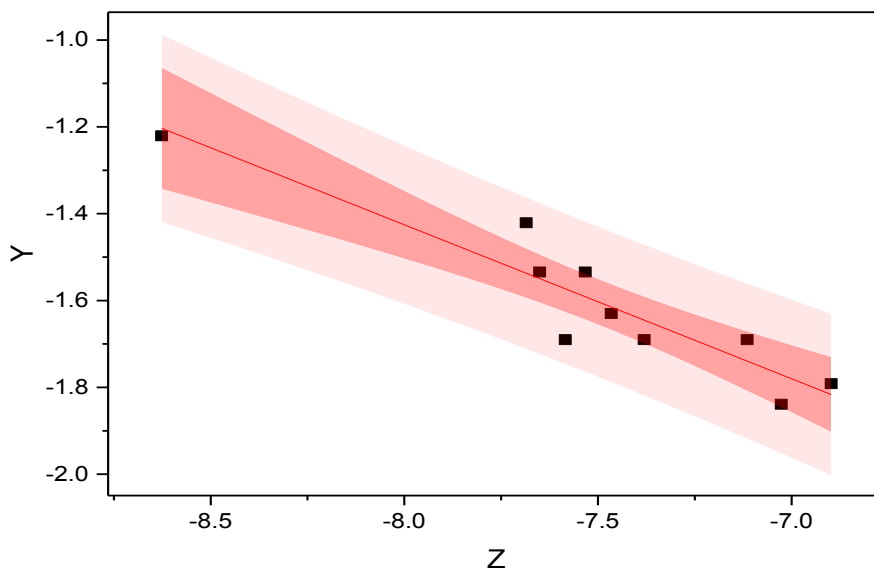
Pure N₂ environment, T = 600°C



n	n	b	b	Statistics	Statistics
Value	Standard Error	Value	Standard Error	Chi-Sqr	R-Square
1.63	0.08	5.83	0.58	0.0054	0.82249

Figure D2: Linear regression for the estimation of reaction order.

Pure N₂ environment, T = 700°C



n	n	b	b	Statistics	Statistics
Value	Standard Error	Value	Standard Error	Chi-Sqr	R-Square
1.35	0.05	4.26	0.37	0.00512	0.84813

Figure D3: Linear regression for the estimation of reaction order.

Pure N₂ environment, T = 800°C

Appendix E

X-ray Diffraction (XRD) Patterns

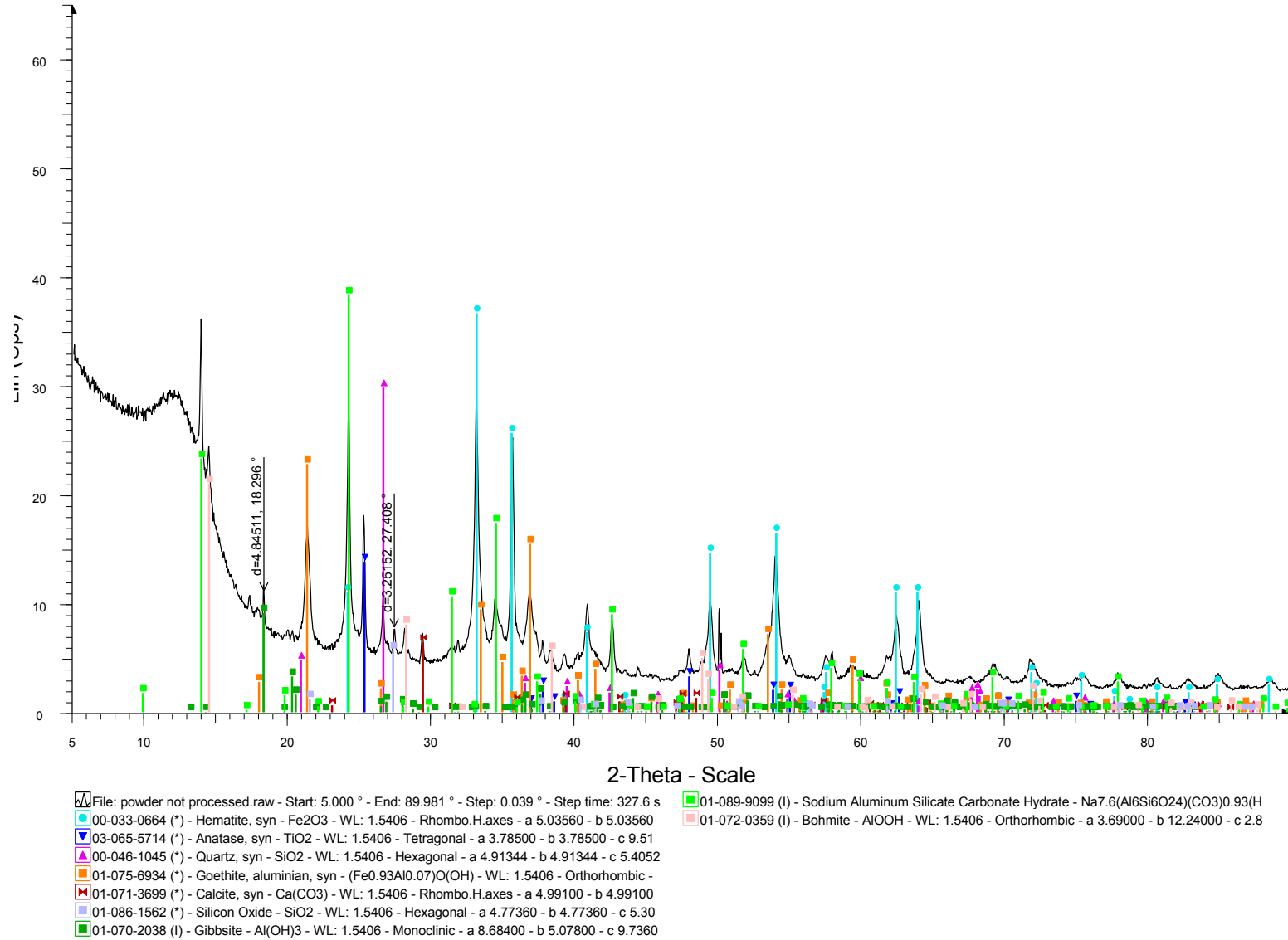
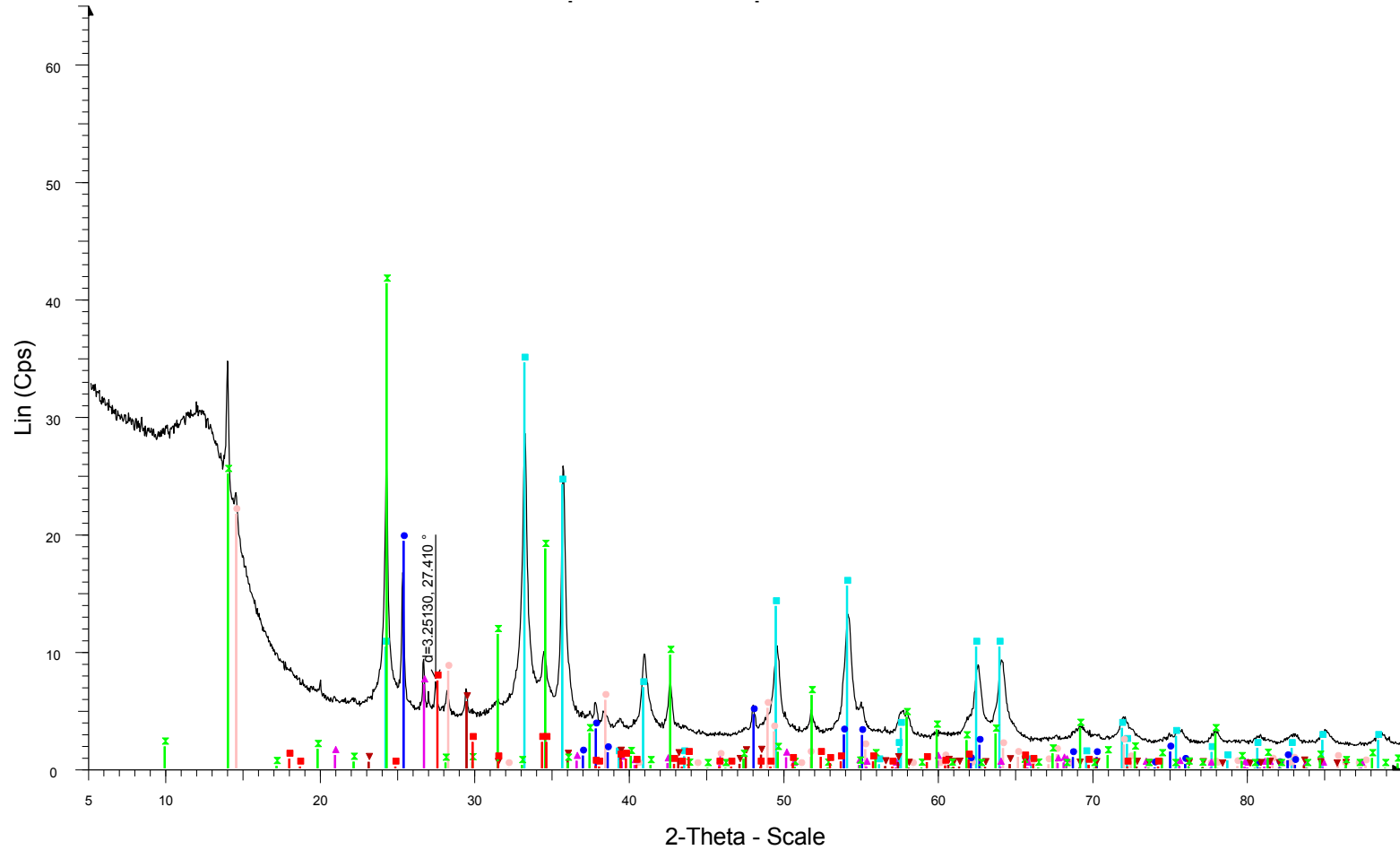
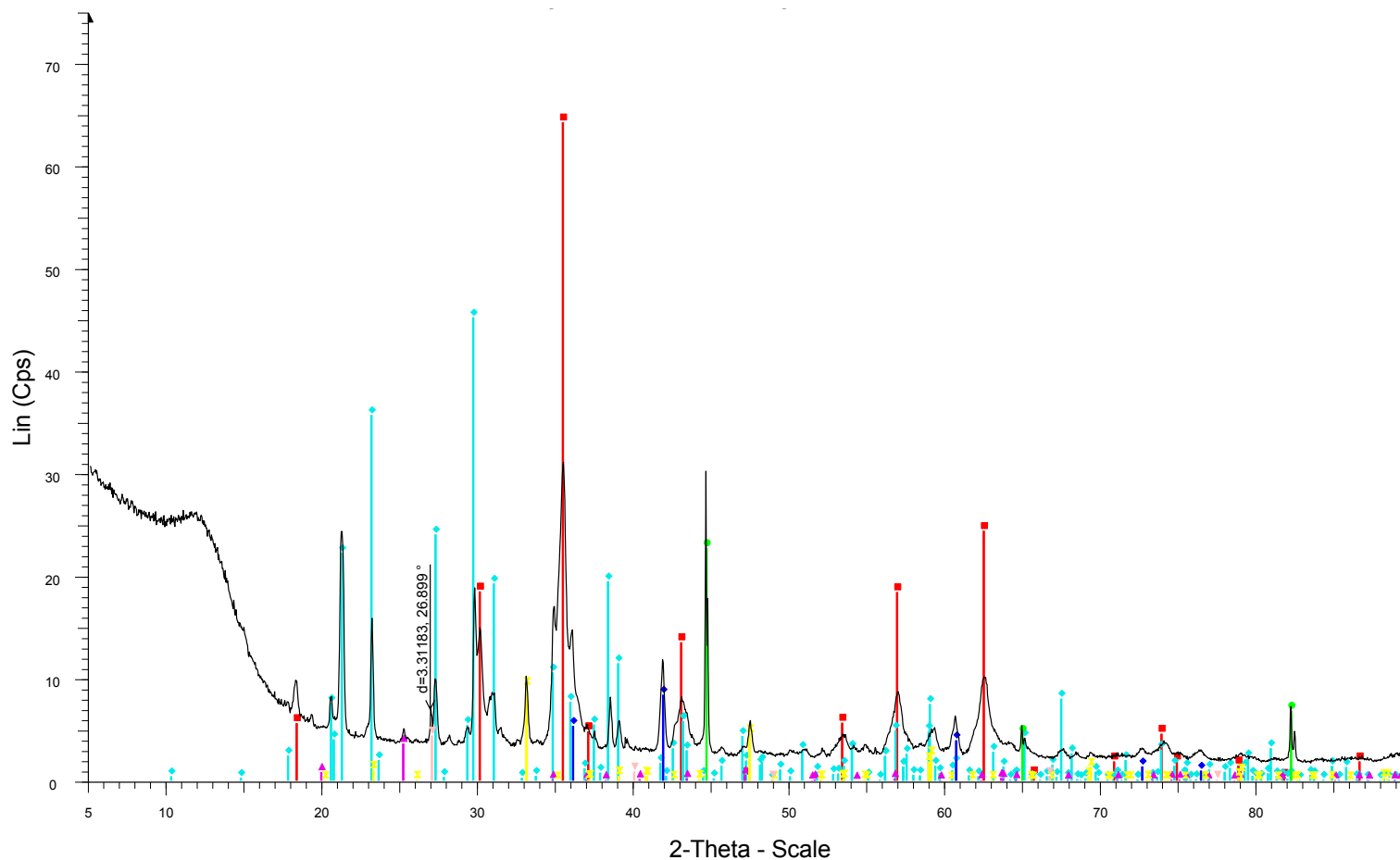


Figure E1: Powder XRD profile of the as-received red mud powder



File: processed pellet.raw - Start: 5.000 ° - End: 89.981 ° - Step: 0.039 ° - Step time: 327.6 s - Anode: Cu - WL1: 1.5406 - WL2: 1.54439 - kA2 Ratio: 0.5 - Generator kV: 40 kV - Generator mA: 40 mA -
 00-033-0664 (*) - Hematite, syn - Fe₂O₃ - WL: 1.5406 - Rhombo.H.axes - a 5.03560 - b 5.03560 - c 13.74890 - alpha 90.000 - beta 90.000 - gamma 120.000 - Primitive - R-3c (167) - 6 - 301.926 - I/c P
 01-072-0359 (I) - Bohmite - AlOOH - WL: 1.5406 - Orthorhombic - a 3.69000 - b 12.24000 - c 2.86000 - alpha 90.000 - beta 90.000 - gamma 90.000 - Base-centered - Amam (63) - 4 - 129.174 - I/c PDF
 03-065-5714 (*) - Anatase, syn - TiO₂ - WL: 1.5406 - Tetragonal - a 3.78500 - b 3.78500 - c 9.51400 - alpha 90.000 - beta 90.000 - gamma 90.000 - Body-centered - I41/amd (141) - 4 - 136.300 - I/c PD
 00-046-1045 (*) - Quartz, syn - SiO₂ - WL: 1.5406 - Hexagonal - a 4.91344 - b 4.91344 - c 5.40524 - alpha 90.000 - beta 90.000 - gamma 120.000 - Primitive - P3221 (154) - 3 - 113.010 - I/c PDF 3.4 -
 01-071-3699 (*) - Calcite, syn - Ca(CO₃) - WL: 1.5406 - Rhombo.H.axes - a 4.99100 - b 4.99100 - c 17.06200 - alpha 90.000 - beta 90.000 - gamma 120.000 - Primitive - R-3c (167) - 6 - 368.075 - I/c P
 01-089-9099 (I) - Sodium Aluminum Silicate Carbonate Hydrate - Na_{7.6}(Al₆Si₆O₂₄)(CO₃)_{0.93}(H₂O)_{2.93} - WL: 1.5406 - Cubic - a 8.99630 - b 8.99630 - c 8.99630 - alpha 90.000 - beta 90.000 - gamma
 00-025-0177 (I) - Titanite, syn - CaTiO(SiO₄) - WL: 1.5406 - Monoclinic - a 7.06600 - b 8.70500 - c 6.56100 - alpha 90.000 - beta 113.930 - gamma 90.000 - Base-centered - A2/a (15) - 4 - 368.874 - F30

Figure E2: Powder XRD profile of fresh pelletized red mud



File: post-reaction pellet.raw - Start: 5.000 ° - End: 89.981 ° - Step: 0.039 ° - Step time: 327.6 s - Anode: Cu - WL1: 1.5406 - WL2: 1.54439 - kA2 Ratio: 0.5 - Generator kV: 40 kV - Generator mA: 40 mA
 01-087-0244 (*) - Magnetite, syn - $\text{Fe}_2.964\text{O}_4$ - WL: 1.5406 - Cubic - a 8.39610 - b 8.39610 - c 8.39610 - alpha 90.000 - beta 90.000 - gamma 90.000 - Face-centered - Fd-3m (227) - 8 - 591.879 - I/lc P
 01-078-5177 (N) - Nepheline - $\text{K}_{1.43}\text{Na}_6(\text{AlSiO}_4)_8$ - WL: 1.5406 - Hexagonal - a 9.99567 - b 9.99567 - c 8.37777 - alpha 90.000 - beta 90.000 - gamma 120.000 - Primitive - P63 (173) - 1 - 724.908 - I/lc
 01-080-2147 (C) - Silicon Oxide - SiO_2 - WL: 1.5406 - Hexagonal - a 5.15390 - b 5.15390 - c 5.79810 - alpha 90.000 - beta 90.000 - gamma 120.000 - Primitive - P3221 (154) - 3 - 133.379 - I/lc PDF 2.9
 01-070-8503 (*) - Perovskite, syn - $\text{Ca}(\text{TiO}_3)$ - WL: 1.5406 - Orthorhombic - a 5.40430 - b 5.42240 - c 7.65100 - alpha 90.000 - beta 90.000 - gamma 90.000 - Primitive - Pbnm (62) - 4 - 224.207 - I/lc PD
 00-006-0696 (*) - Iron, syn - Fe - WL: 1.5406 - Cubic - a 2.86640 - b 2.86640 - c 2.86640 - alpha 90.000 - beta 90.000 - gamma 90.000 - Body-centered - Im-3m (229) - 2 - 23.5511 - F6=222(0.0040,6)
 00-038-0449 (Q) - Allophane - $\text{Al}_2\text{O}_3 \cdot 2\text{SiO}_2 \cdot 3\text{H}_2\text{O}$ - WL: 1.5406 - b 9.00000 - c 7.00000 -
 01-073-2143 (I) - Wustite, syn - $\text{Fe}_9.74\text{O}$ - WL: 1.5406 - Cubic - a 4.30880 - b 4.30880 - c 4.30880 - alpha 90.000 - beta 90.000 - gamma 90.000 - Face-centered - Fm-3m (225) - 4 - 79.9961 - I/lc PDF 4

Figure E3: Powder XRD profile of spent red mud pellet under pure N_2 environment at 800C for 1 hour

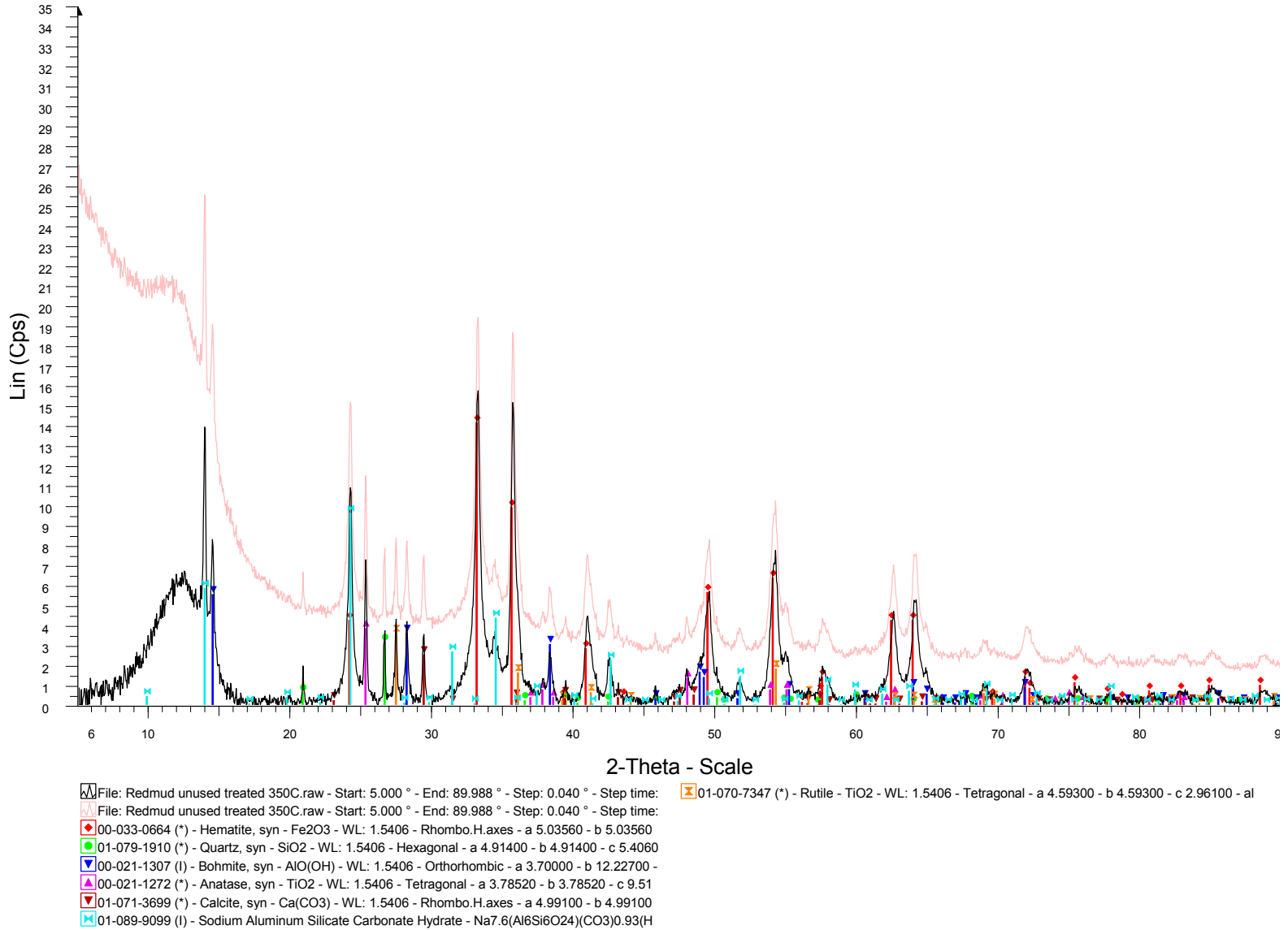


Figure E4: Powder XRD profile of fresh red mud pellet heated to 350C

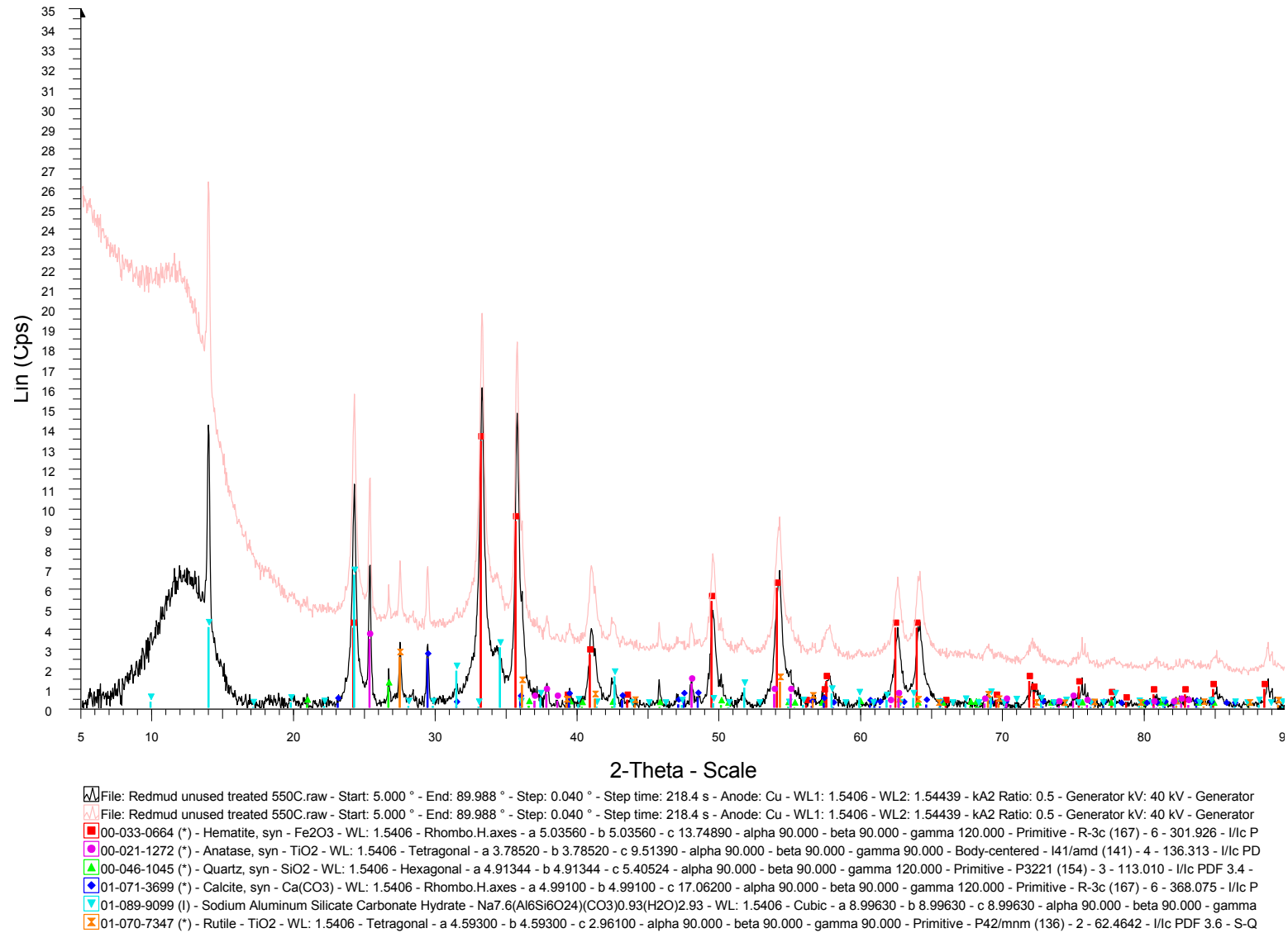


Figure E5: Powder XRD profile of fresh red mud pellet heated to 550C

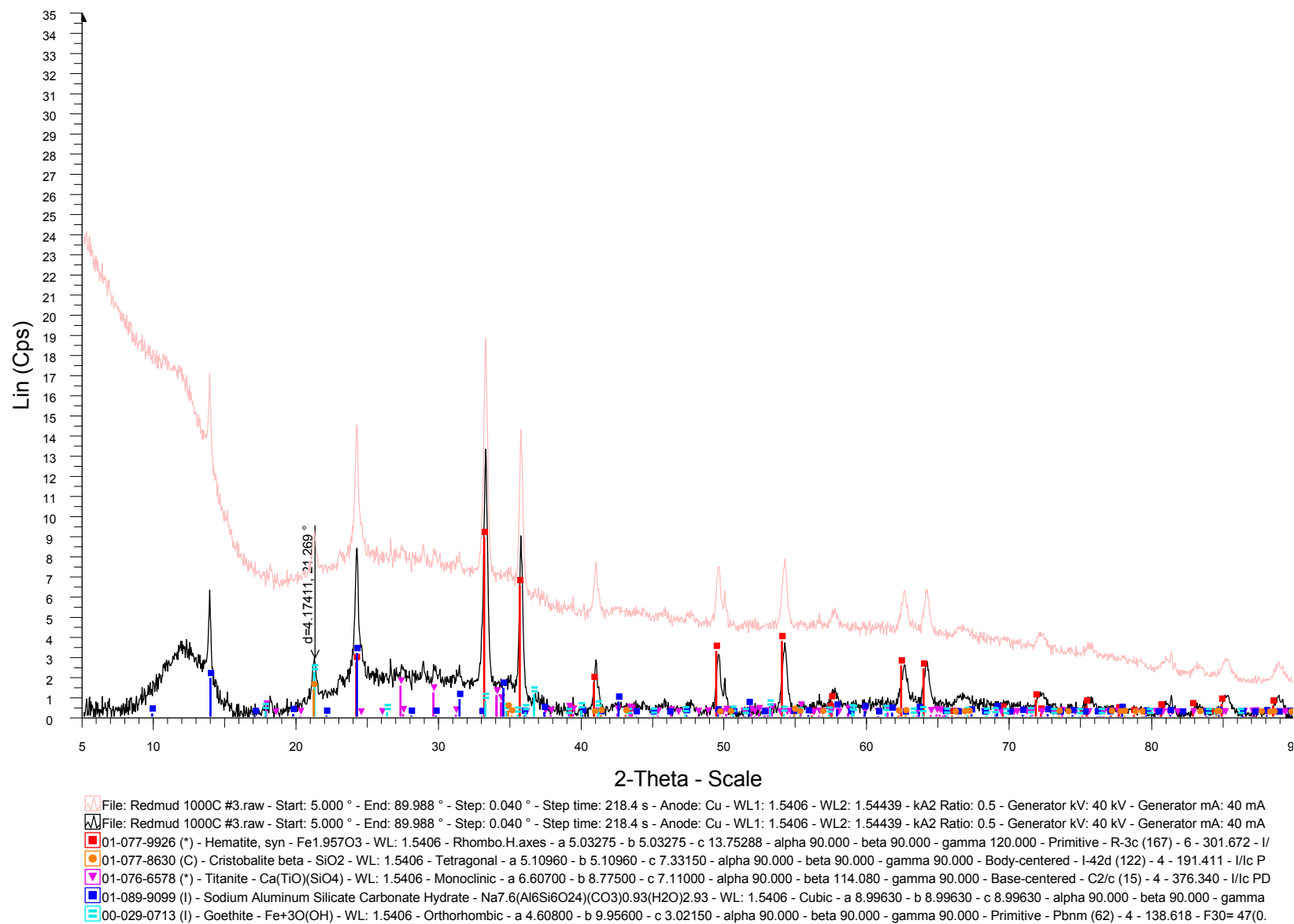


Figure E6: Powder XRD profile of fresh red mud pellet heated to 1000C

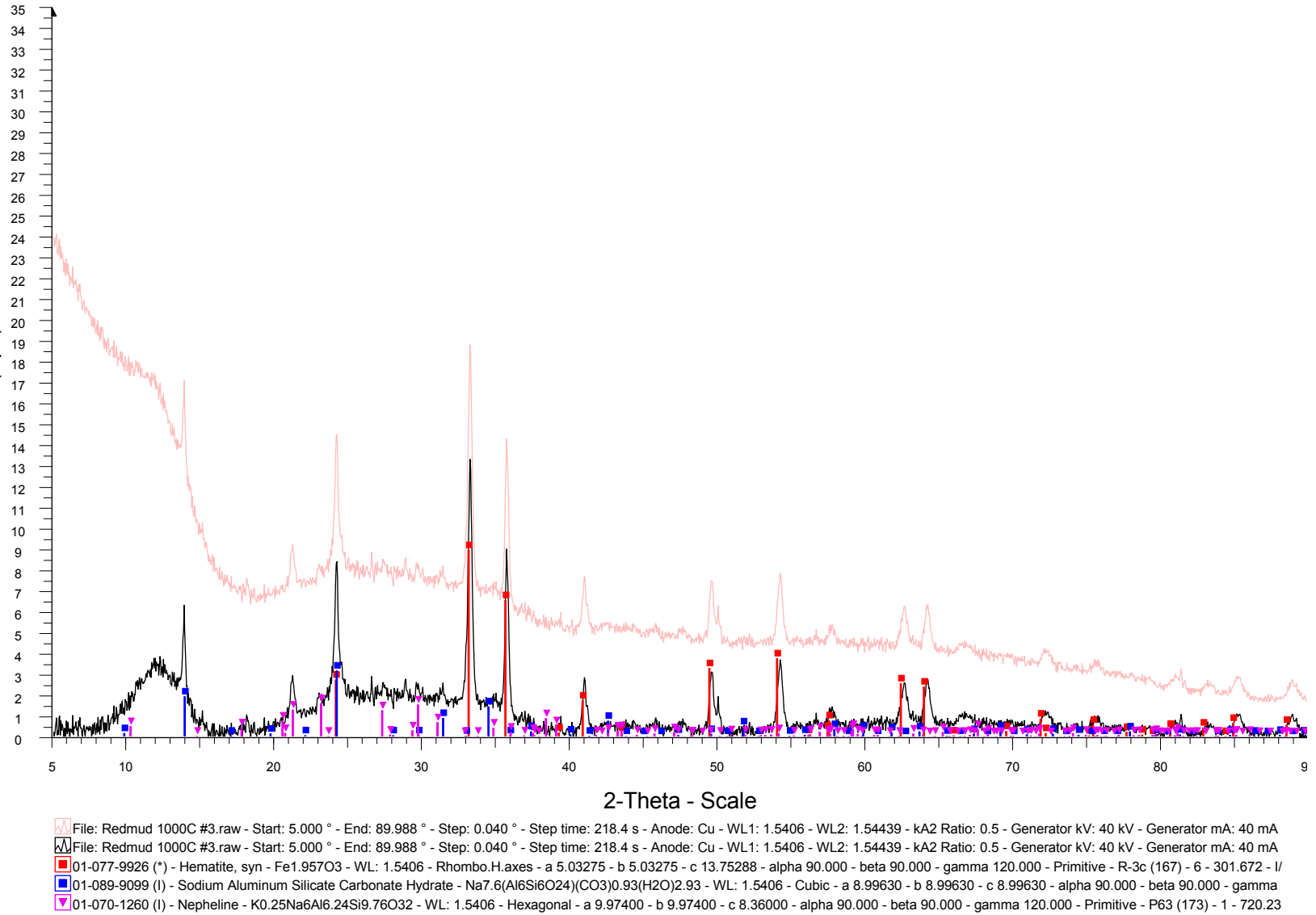


Figure E7: Powder XRD profile of fresh red mud pellet heated to 1000C

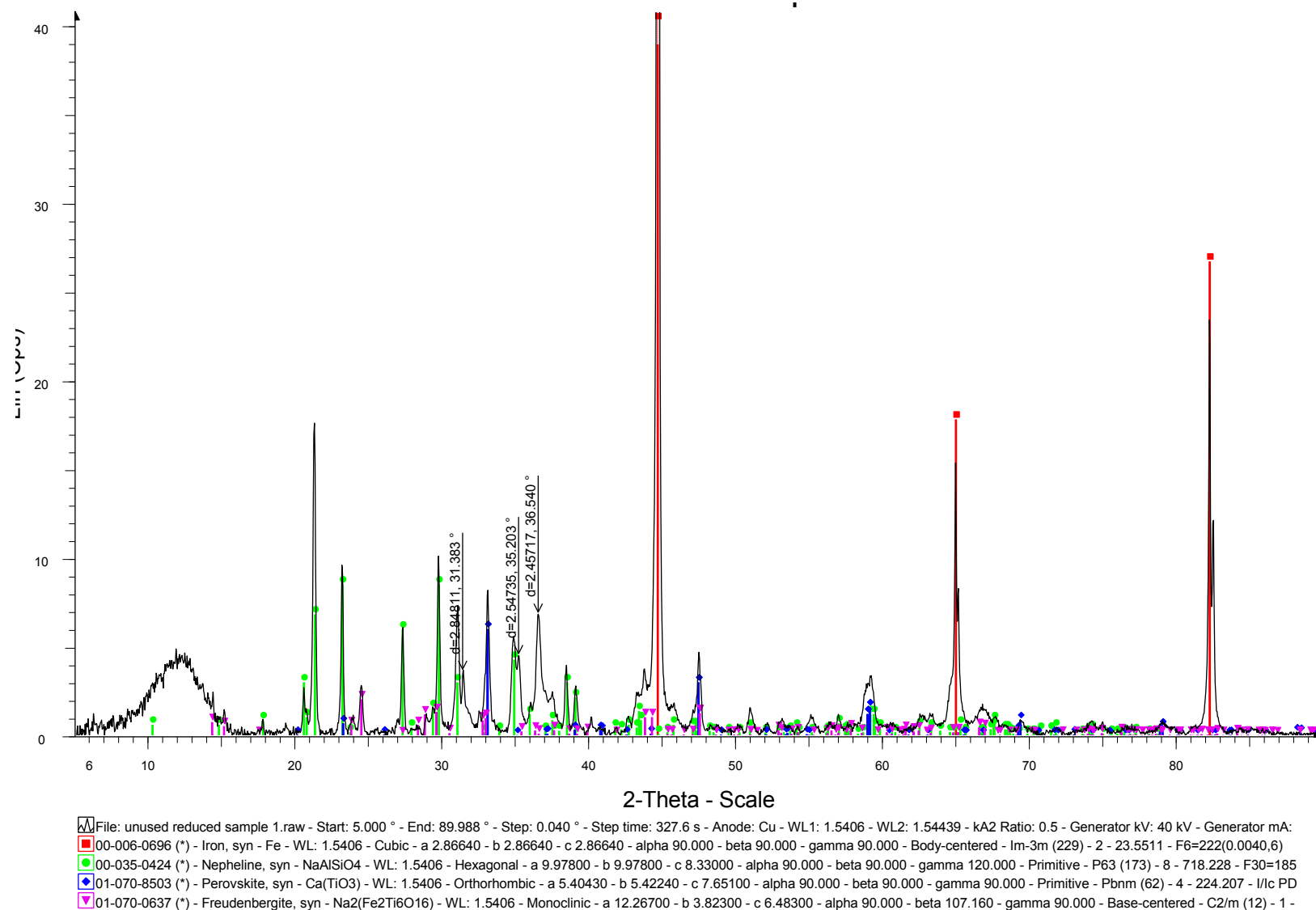


Figure E8: Powder XRD profile of fresh red mud pellet reduced at 800C

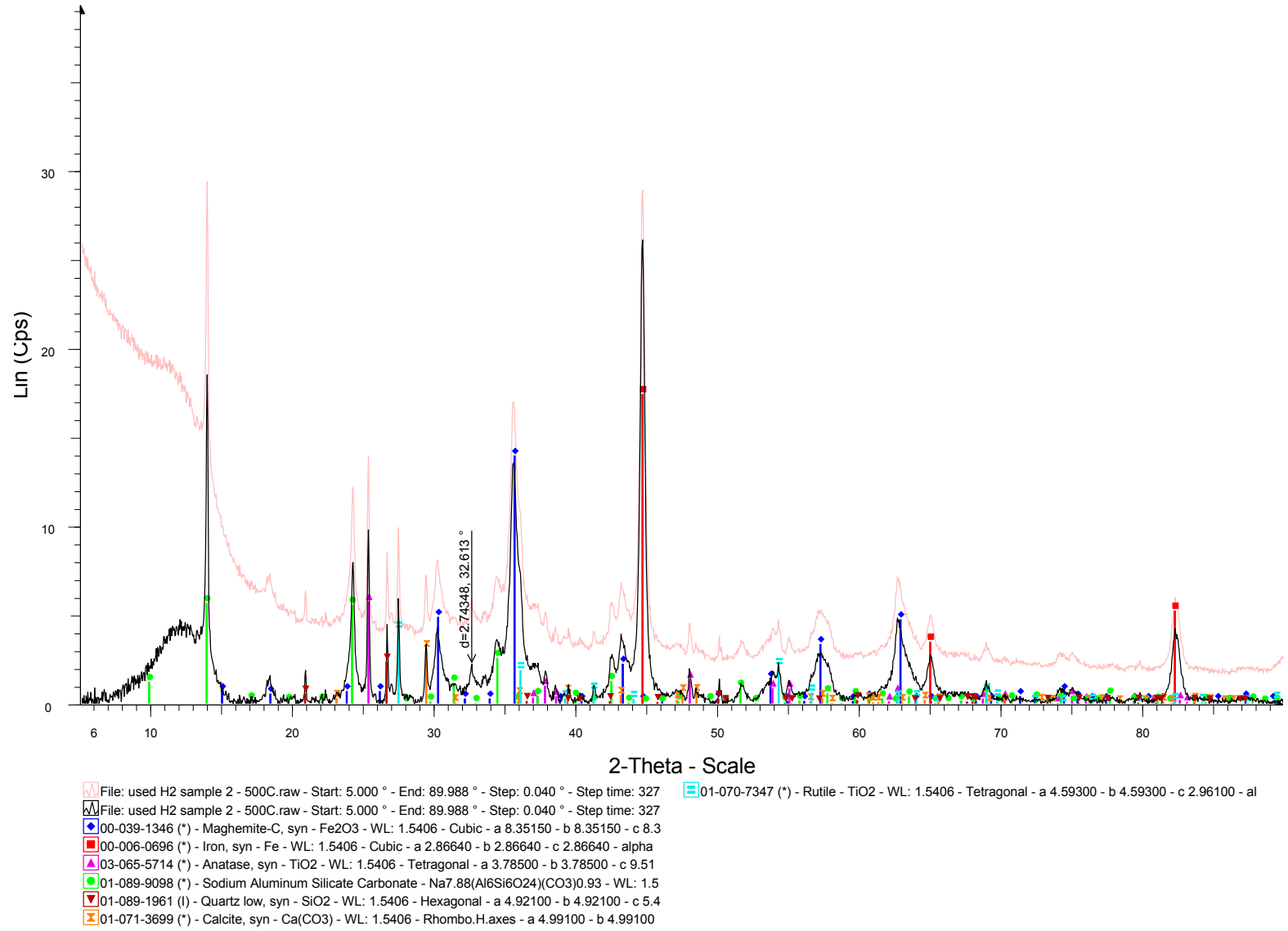


Figure E9: Powder XRD profile of fresh red mud pellet reduced at 500C

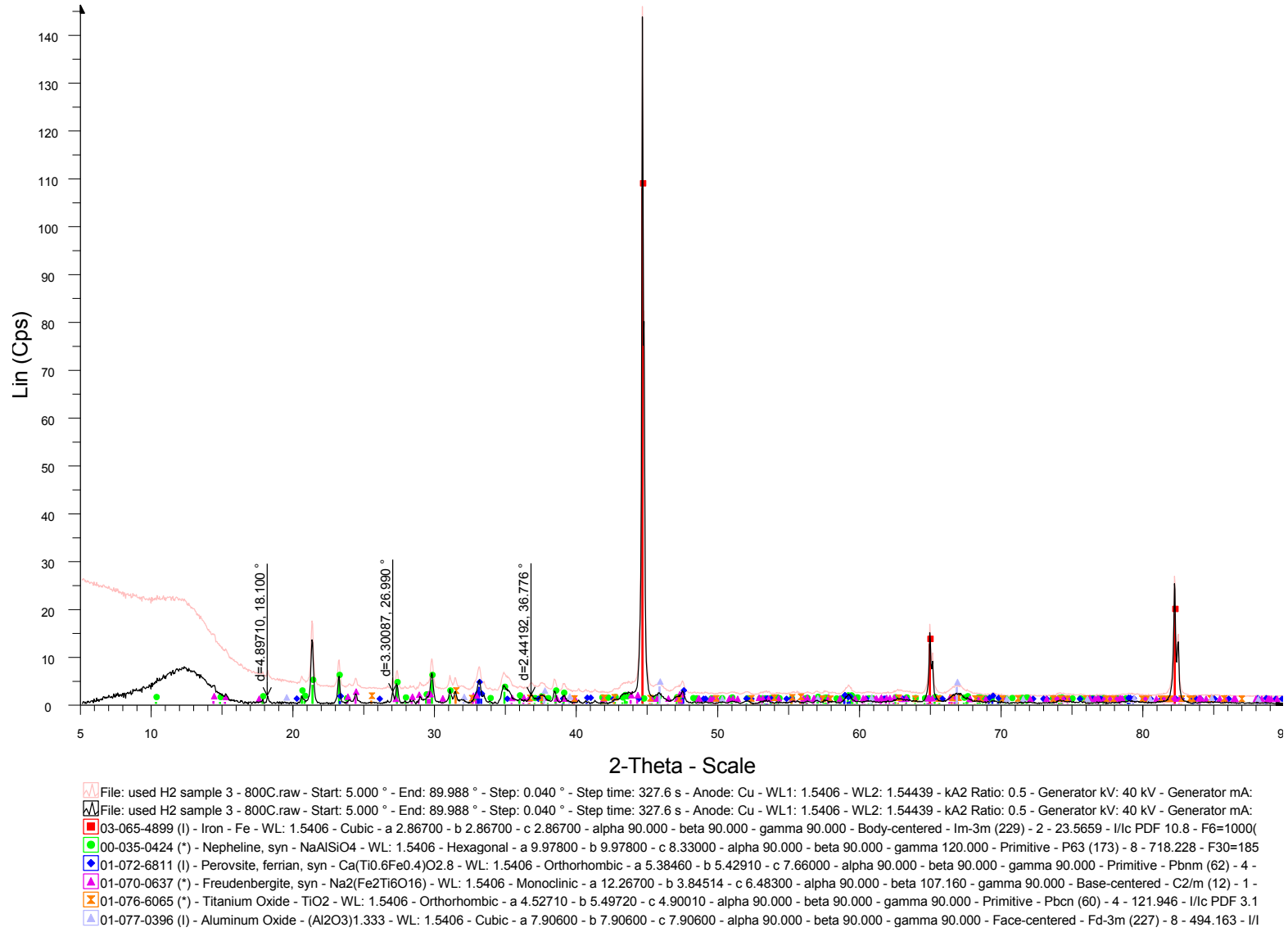


Figure E10: Powder XRD profile of spent red mud pellet under 13 vol.% H₂ in N₂ at 800C for 1 hour

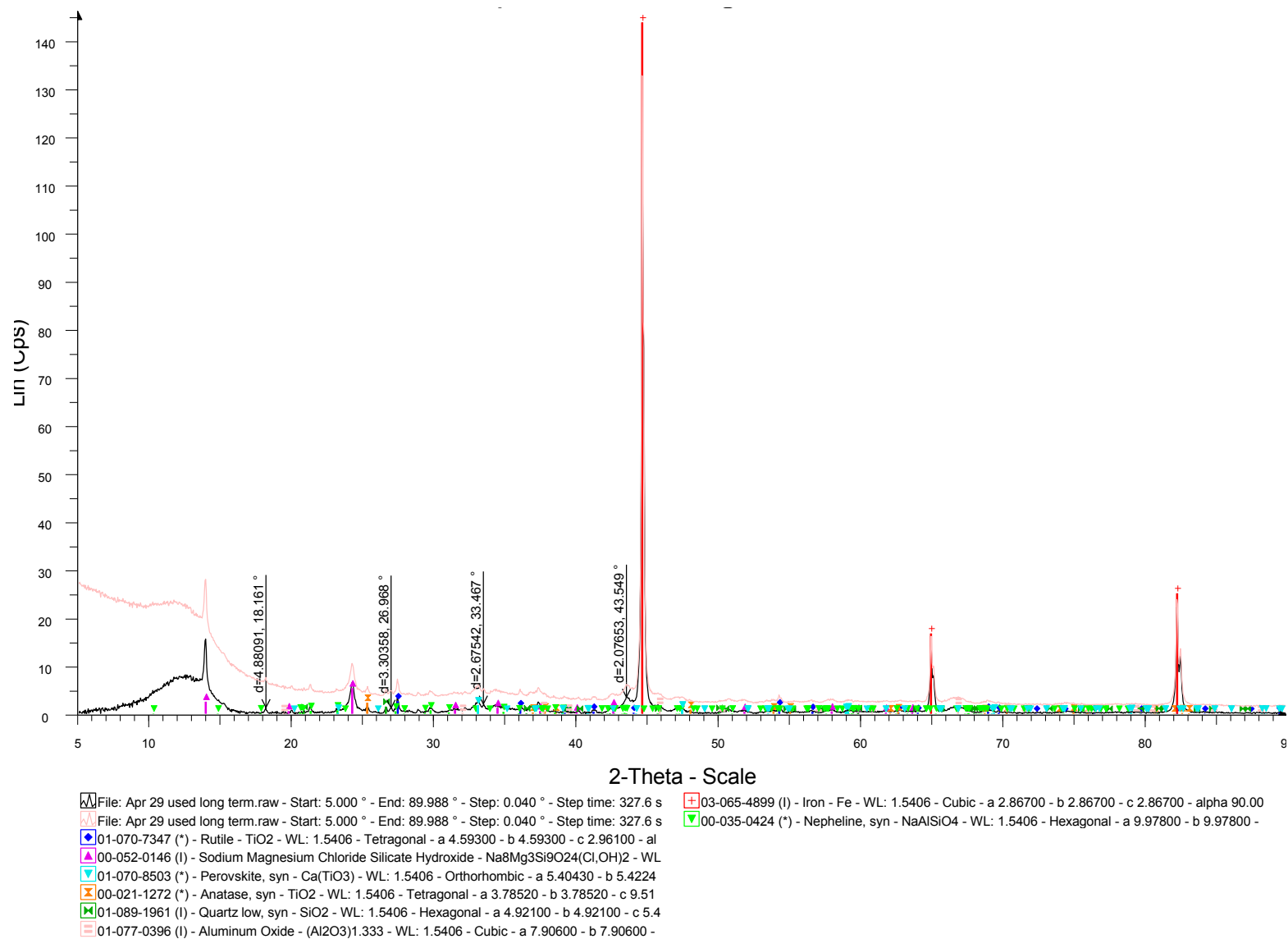


Figure E11: Powder XRD profile of spent red mud pellet under 13 vol.% H₂ in N₂ at 800C for 14 hours

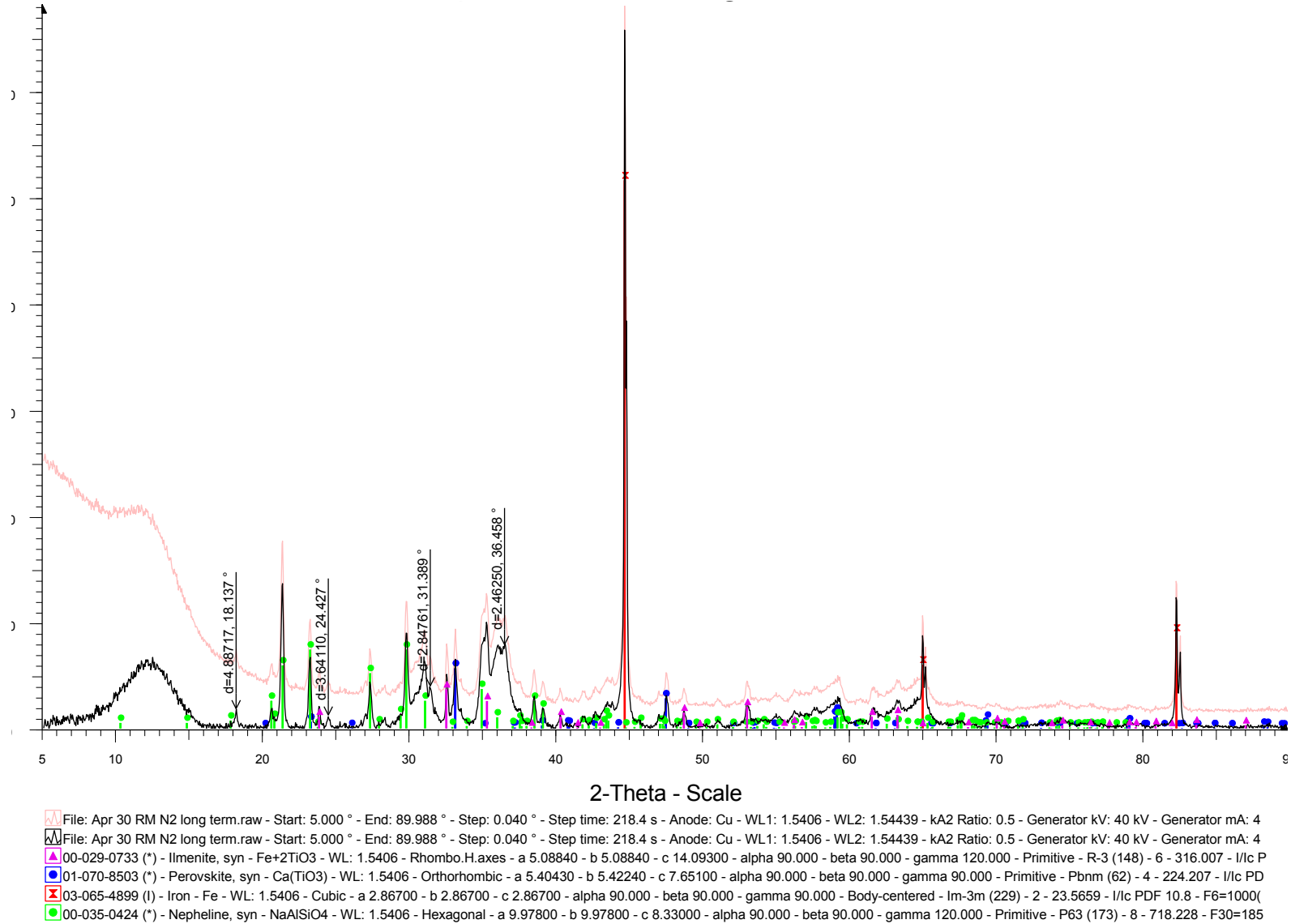


Figure E12: Powder XRD profile of spent red mud pellet under pure N₂ at 800C for 14 hours

Appendix F

X-ray Photoelectron Spectrometry (XPS)

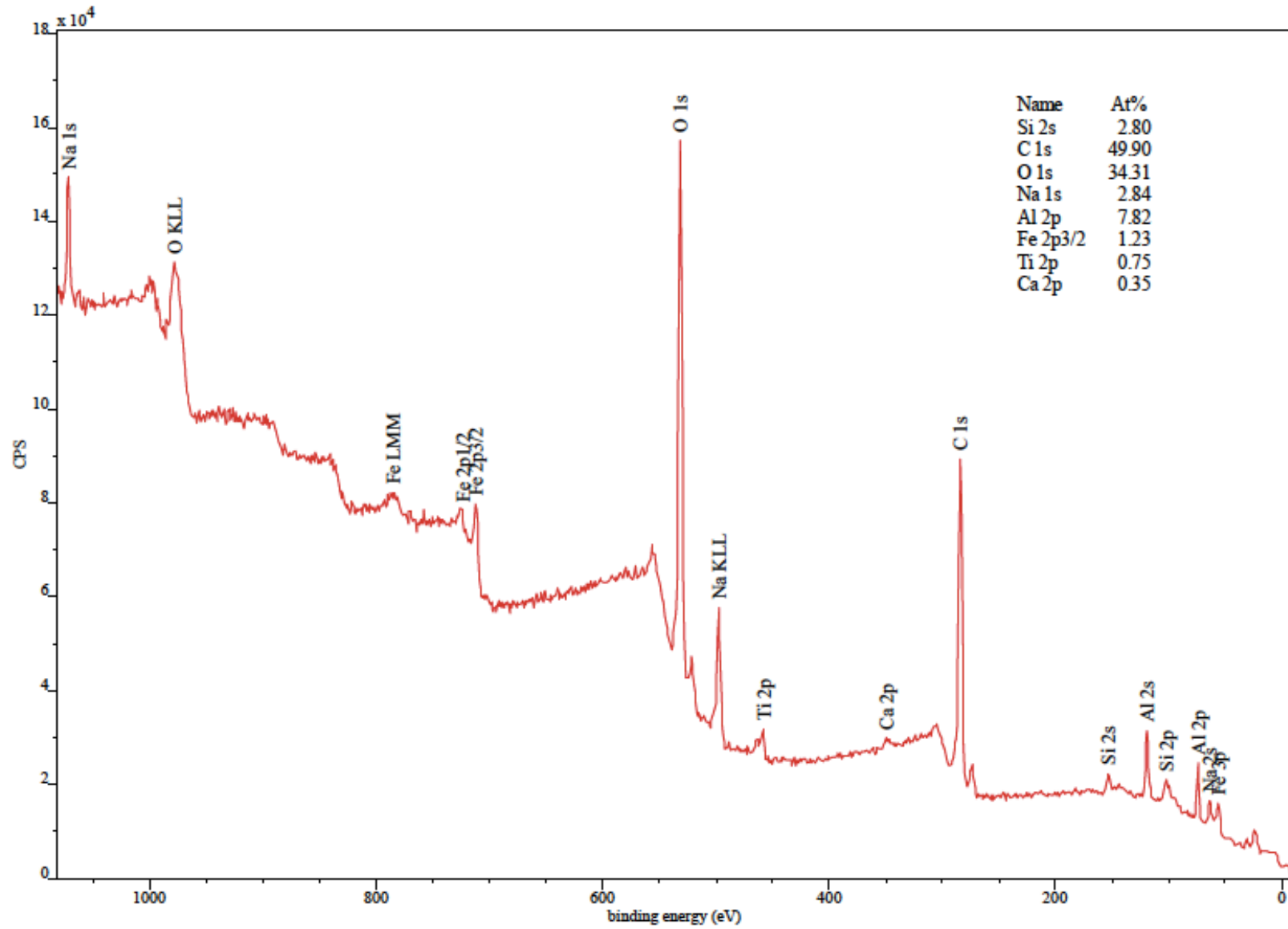


Figure F1: XPS spectra of fresh as-received red mud powder

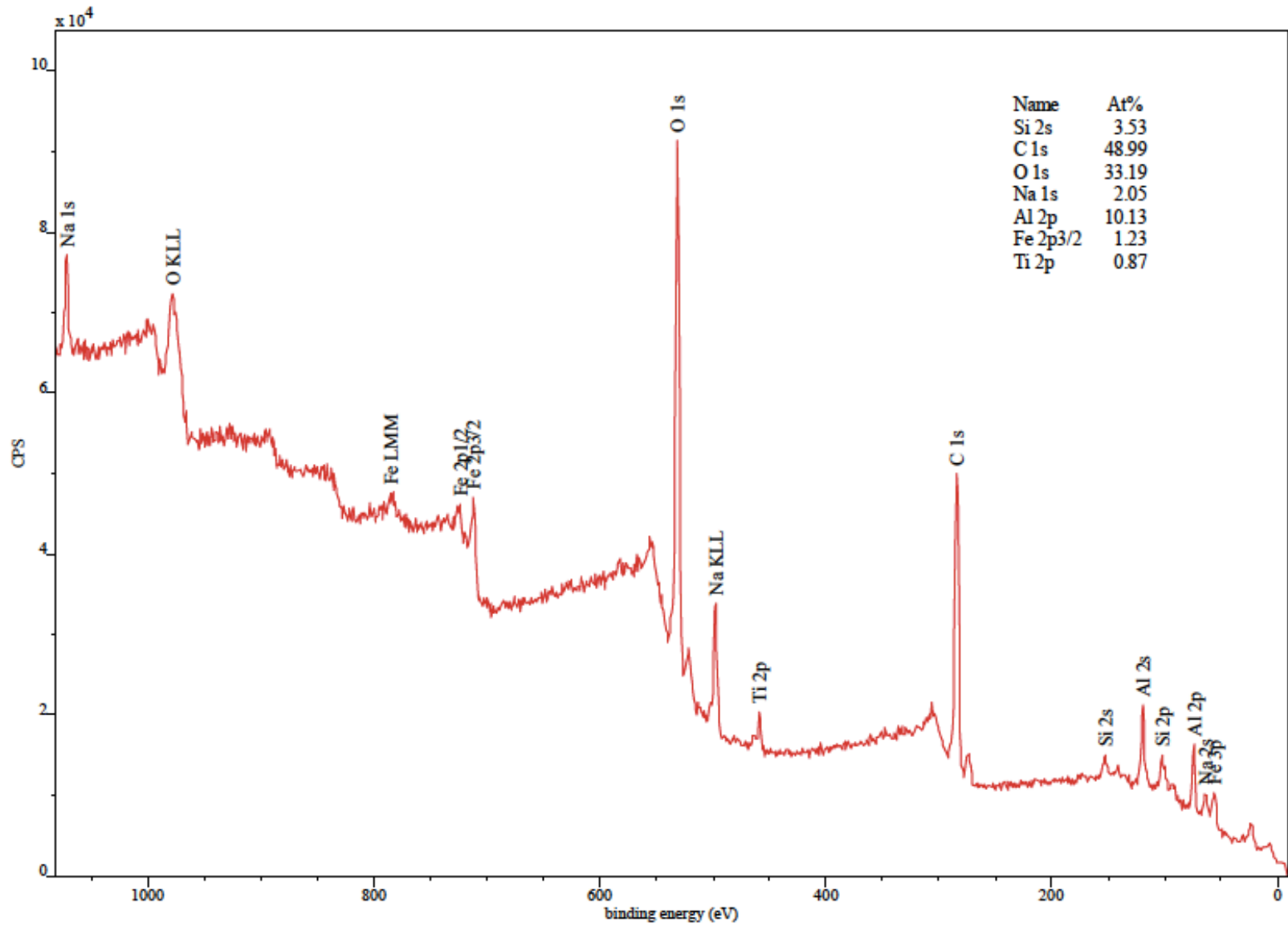


Figure F2: XPS spectra of fresh prepared red mud pellet

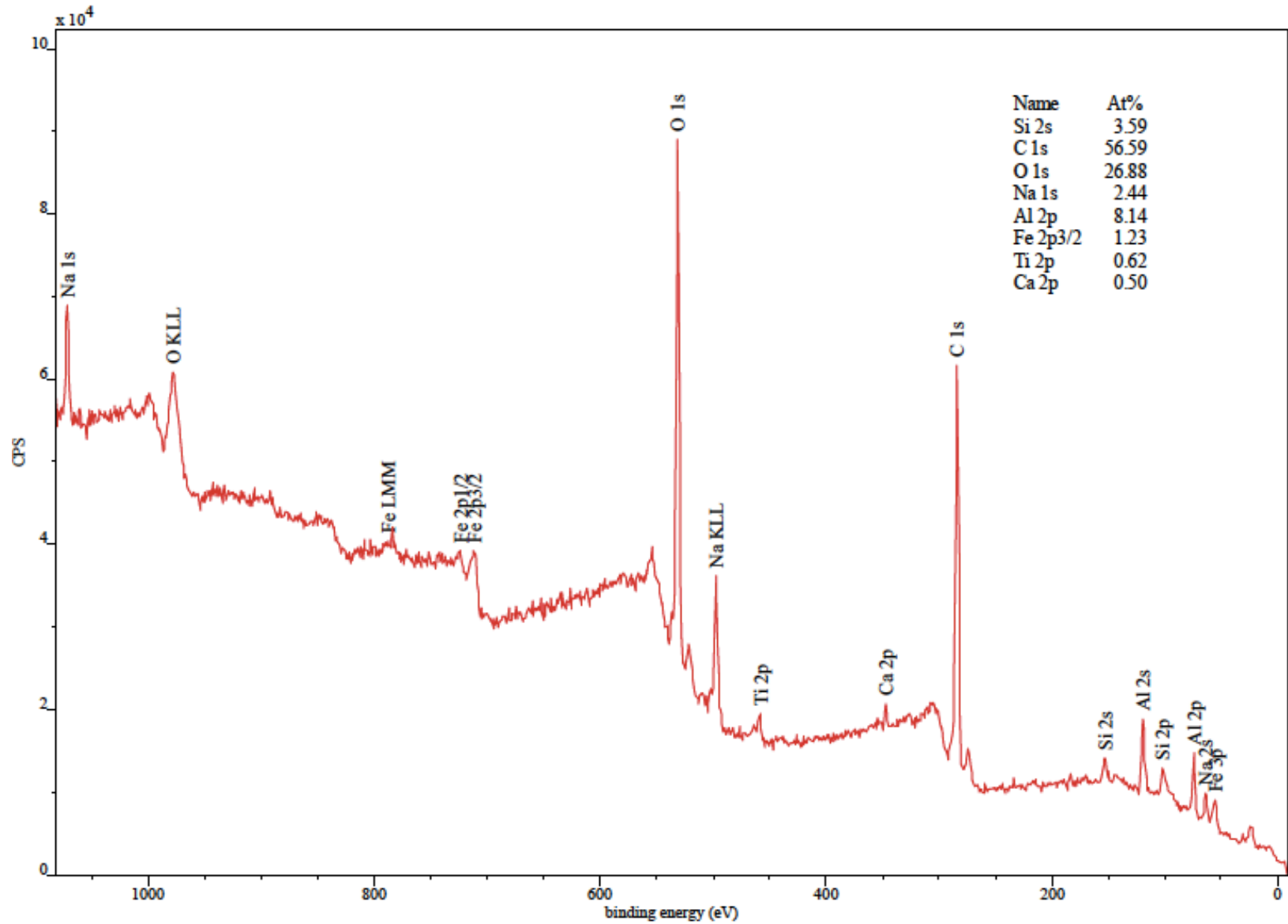


Figure F3: XPS spectra of spent red mud pellet

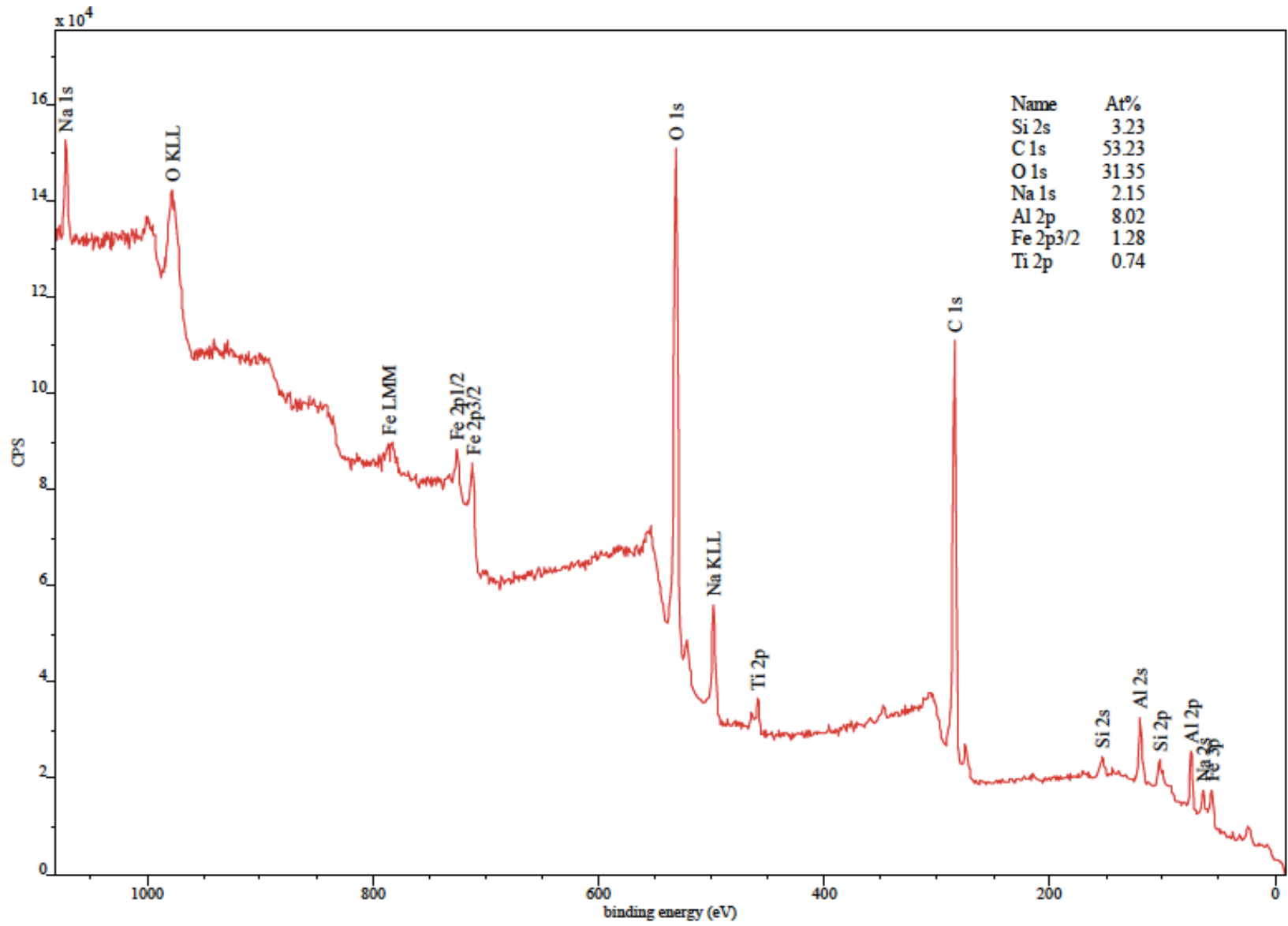


Figure F4: XPS spectra of fresh as received red mud powder, heated at 300°C for 24h right before analysis

Appendix G

Brunauer–Emmett–Teller Analysis (BET)

The BET surface area and pore volume of the catalyst were determined by means of nitrogen adsorption-desorption isotherms at 77 K in a Micromeritics AutoChem II 2920 equipment. The amount of nitrogen adsorbed at a relative pressure of $p/p_0 = 0.01$ to $p/p_0 = 0.98$ was used to evaluate the total surface area and pore volume, respectively. The surface area was determined using the Brunauer-Emmett-Teller (BET) theory.

$$\frac{1}{V\left(\frac{P_0}{P} - 1\right)} = \frac{C - 1}{V_m C} \cdot \left(\frac{P}{P_0}\right) + \frac{1}{V_m C} \quad G - 1$$

P = equilibrium pressure

P_0 = Saturation pressure of adsorbate gas at the temperature of adsorption

V = Volume adsorbed

V_m = monolayer adsorbed quantity (Volume units)

C = BET constant

$$C = \exp\left(\frac{E_1 - E_L}{RT}\right) \quad G - 2$$

E_1 = Heat of adsorption for the first layer

E_L = Heat of adsorption for the second and higher layers and is equal to the heat of liquefaction.

Plotting the left-side expression of Equation G-1, $(\frac{1}{V(\frac{P_0}{P}-1)})$ vs. the relative pressure $(\frac{P}{P_0})$ would result in a line, from which the monolayer adsorbed volume (V_m) and C could be determined. Once these are evaluated, the BET surface area of the catalyst could be calculated according to:

$$S_{BET} = \frac{V_m \sigma N_A}{V_0} \quad G - 3$$

Where σ is the adsorption cross section of a single N_2 molecule (16.2 \AA^2) and N_A is the Avogadro's number.

Table G1: Red mud BET surface area and pore volumes reported in the literature

Supplier	BET surface area m ² /g	Pore volume cm ³ /g	Reference #
Shandong Aluminium Corporation	23	0.067	[132]
Karnataka, India	26.58		[92]
Odisha, India	39.24		[92]
NALCO,	32	0.175	[108]
NALCO, India	13-20	0.086	[110]
Shandong Aluminium Corporation	27	0.089	[132]
National Aluminium Company India	31.39	NA	[108]
Sao Luis-Maranhao, Brazil	12.96	NA	[114]
KC Industry, Korea	23	0.11	[129]

Appendix H

Plug Flow Reactor Design Calculations

Fluid composition: 100% N₂ at 800C

$$\rho_{1073K} = \rho_{273K} * (T2/T1) = 1.251*1073/273 = 0.3139 \text{ kg/m}^3 \text{ [158]}$$

$$\mu_{\text{dynamic}} = 4.357\text{E-}6 \text{ Pa.s [158]}$$

$$D_{\text{bed}} = 0.015\text{m}$$

$$A_{\text{c_bed}} = \pi D^2/4 = 1.767\text{E-}4 \text{ m}^2$$

$$\rho_{\text{cat}} = 2500 \text{ kg/m}^3$$

$$Q = 385 \text{ mL/min at STP} \rightarrow 385*1073/273 = 1513 \text{ mL/min at 800C}$$

$$\epsilon_{\text{void}} = 0.5$$

$$U_s = Q/A_c = 0.1427 \text{ m/s}$$

$$m_{\text{cat}} = 3.85\text{g}$$

$$D_{\text{cat}} = 2 \text{ mm}$$

$$L_{\text{cat}} = 7.5 \text{ mm}$$

$$dp_{\text{cat}} = (6*\pi D^2/4*L/\pi)^{1/3} = 3.55\text{E-}03 \text{ m [159]}$$

$$Re = \rho*dp_{\text{cat}}*U_s/\mu = 21.614$$

$$\gamma = (2\pi rL + 2\pi r^2)/(\pi d_p^2) = 1.349$$

$$Re' = Re/((1-\epsilon)\gamma) = 32.04$$

Looking at Bischoff's chart of axial dispersion (Fig. H1):

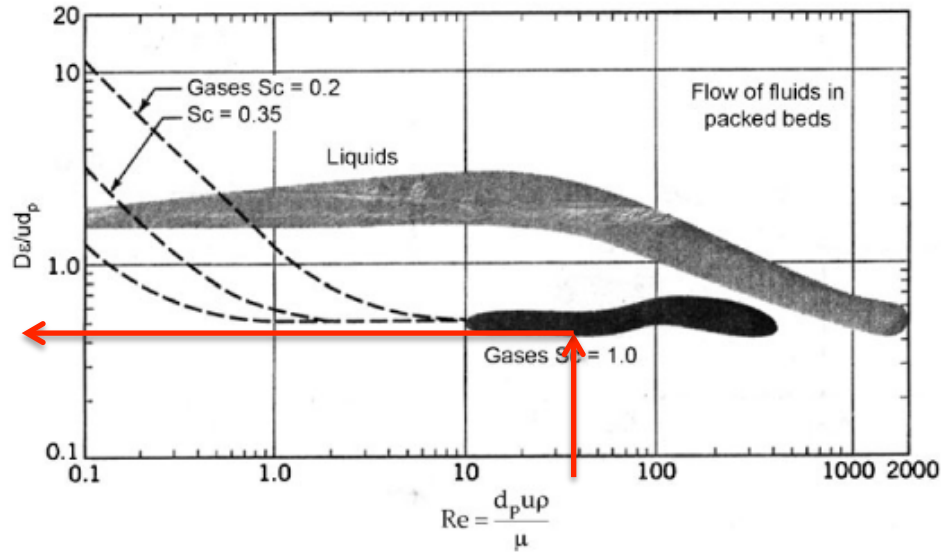


Figure H1: Bischoff findings on dispersion of fluid flowing in packed beds [160]

From Fig. H1, the value of the Bischoff constant (B) can be found to be 0.48. Hence:

$$D\varepsilon = B \cdot U_s \cdot d_p = 2.43E-04$$

$$D_{AB} = D\varepsilon / (\varepsilon_{\text{void}}) = 4.86E-04$$

$$Pe_{\text{axial}} = D_{\text{bed}} \cdot U_s / D_{AB} = 8.81$$

To check whether plug flow conditions can be assumed in the reactor or not, we need to determine if:

$$L/d_p > 20 \cdot n / Pe \cdot \log(1/(1-X))$$

For a 1st order reaction ($n=1$), considering the worst scenario, i.e. $m_{\text{cat}} = 5\text{g}$ with a bed height of 29 mm, and a complete naphthalene conversion ($X = 0.999$), we can find:

$$L/d_p = 8.451$$

$$20 \cdot n / Pe \cdot \log(1/(1-X)) = 6.81$$

Since **8.451 > 6.81**, plug flow can be assumed in the reactor.